TECHNISCHE UNIVERSITÄT WIEN

DISSERTATION

The Ice Nucleation Activity of Carbonaceous Particles

ausgeführt zum Zwecke der Erlangung des akademischen Grades eines Doktors der technischen Wissenschaften unter der Leitung von

Ao. Univ.-Prof. Dr. Hinrich Grothe
E165
Institut für Materialchemie

eingereicht an der Technischen Universität Wien
Fakultät für Technische Chemie

von

Dipl. Ing. Thomas Häusler
Matr.-Nr. 0527726
Getreidemarkt 9/BC01
A-1060 Wien

Wien, am 01.05.2018 _____

Zusammenfassung

Wolken haben aufgrund ihres Einflusses auf das Klimasystem, Wetterphänomene oder den Wasserkreislauf der Erde eine wichtige Rolle in der Erdatmosphäre. Dabei bestimmt die Mikrophysik der Wolken unter anderem die Wechselwirkung mit sichtbarer und infraroter Strahlung, den Lebenszyklus der Wolken, oder die Eigenschaften von Niederschlägen. In all diesen Prozessen spielen Aerosolpartikel eine bedeutende Rolle. Diese dienen einerseits als Wolkenkondensationskeime zur Bildung von flüssigen Tropfen, andererseits als Eiskeime zur Bildung von Eiskristallen. Eiskeime katalysieren den Gefrierprozess in Wolken und unterstützen damit den kinetisch gehemmten Phasenübergang von flüssigem Wasser zu Eis. Dieser Prozess wird als heterogene Eisnukleation bezeichnet. Kohlenstoffhaltige Verbrennungsrückstände wie Ruß, biologisches Material wie Pollen oder Bakterien, aber auch mineralische Stäube wie Albit oder Feldspat können als Eiskeime dienen. Auf Grund dieser enormen Vielfalt und Komplexität der Eiskeime, ist der Prozess der Eisbildung weitestgehend unverstanden.

Ziel dieser Arbeit war es grundlegende Kenntnisse zu den physikalischen und chemischen Prozessen der Eisnukleation zu erlangen. Dazu wurde das Gefrierverhalten von künstlich erzeugten Tropfen, versetzt mit unterschiedlichen Eiskeimen, untersucht. Die gebräuchliche Analysentechnik zur Bestimmung des Gefrierverhaltens von wässrigen Tropfen im Mikrometermaßstab wurde grundlegend überarbeitet. Dabei konnten wesentliche Verbesserungen, wie die Bildung von Tropfen mit definierten Durchmessern zwischen 20 µm und 80 µm oder eine automatisierte Evaluierung des Gefriervorganges, realisiert werden. Kohlenstoffhaltige Eiskeime wie Graphen, Ruß, oder Cellulose wurden eingehend bezüglich ihrer Eigenschaften als Eiskeime untersucht. Komplementäre Analysen zur Bestimmung von chemischen und physikalischen Eigenschaften der Keime wurden durchgeführt. Ausführliche Untersuchungen mittels Kryo- und Elektronenmikroskopie, als auch Raman- und Röntgenphotoelektronenspektroskopie, zeigten sowohl den Einfluss der chemischen Zusammensetzung als auch der Kristallstruktur auf die eisbildenden Eigenschaften dieser Keime. Diese Arbeit zeigt die absolute Notwendigkeit einer sorgfältigen Analyse der Gesamtheit sowohl der physikalischen als auch der chemischen Eigenschaften von kohlenstoffhaltigen Partikeln, um eine qualitative Aussage zur Eisnukleationsfähigkeit treffen zu können.

Summary

Clouds are essential for the Earth's climate system, weather phenomena, and the hydrological cycle. Cloud microphysics determine cloud albedo in the visible and infrared spectral ranges, cloud lifetime, and precipitation properties. In all these processes, aerosol particles play a crucial role. They can act as so-called cloud condensation nuclei for liquid droplets and as ice nuclei for the formation of ice particles. Ice nuclei catalyze the freezing process in clouds and support the kinetically hindered phase transition from water to ice, which is called heterogeneous ice nucleation. Several materials can act as ice nuclei, such as carbonaceous residues like soot, biological materials like pollen or bacteria, and mineral dusts like albite or microcline. Even though intensive research on ice nucleation has already been performed for decades, the mechanisms during the freezing process remain still fragmentary. This is, among other reasons, due to the tremendous variability as well as complexity of ice nuclei.

The goal of this study was to obtain a fundamental understanding of physical and chemical processes during ice nucleation, by conducting a comprehensive study of the ice nucleation behavior of artificial droplets including ice nuclei. The current technique to determine the ice nucleating behavior of aqueous droplets in micrometer range was optimized regarding the formation of droplets with defined diameters between 20 µm and 80 µm, process control and experimental evaluation. In addition, carbonaceous ice nuclei as graphene, soot or cellulose have been investigated concerning their properties as ice nuclei. Complementary analysis techniques to determine the particles' chemical and physical properties have been performed. Detailed investigations by cryo- and electron microscopy, as well as Raman- and X-ray photoelectron spectroscopy, revealed the influence of the chemical composition and crystal structure on ice nucleating properties. This study demonstrates the absolute need for a thorough analysis of the entirety of physical and chemical properties of carbonaceous particles in order to draw conclusions concerning their ice nucleation activity.

Acknowledgement

I would like to thank my supervisor, Prof. Hinrich Grothe, for the opportunity to achieve my doctor's degree in his working group and for his consistent support and assistance.

I want to thank Prof. Regina Hitzenberger and Lorenz Witek from the University of Vienna for the successful collaboration.

I am thankful for the collaboration with Prof. Dominik Eder, Prof. Silvia Marchesan, Paul Gebhardt, Greta Haselmann and Daniel Iglesias from TU Wien and Università degli studi di Trieste.

I would like to express my gratitude to Markus Schinnerl and Prof. Alois Lugstein from the Faculty of Electrical Engineering and Information of TU Wien for patiently helping me design the freezing chip.

I want to thank Markus Sauer from the Analytical Instrumentation Center for XPS measurements short-term appointments.

I want to thank Pharmallerga and JRS Pharma for providing pollen and cellulose samples free of charge.

I would like to thank the Austrian Science Fund (FWF: P26040) and TU Wien (travel scholarship) for financial support.

I am thankful for the support of my family and friends.

Esta tesis no habría sido posible sin mi querida familia - Noelia, Valentina y Emma. Os quiero. ¡Muchísimas gracias!

Table of Content

1. Introduction

1.1 The Earth's Atmosphere

The Earth's atmosphere has a series of different layers, each with its own particular properties. Moving from ground level upwards, the layers are called troposphere, stratosphere, mesosphere, thermosphere and exosphere (see Figure 1-1). They are well described and summarized e.g. by Seinfeld and Pandis (1998).

The troposphere is the lowest layer of Earth's atmosphere. It stretches from the ground level to about 10 km above sea level. Air pressure and temperature decreases as one climbs higher in the troposphere. Nearly all weather occurs in this lowest layer since 99% of all water vapor in the atmosphere is found here and most clouds appear in the troposphere. The concentration of water vapor in the troposphere varies from 0 to 5%, depending on the location. Higher values are achieved in oceanic regions and lower values in deserts. The atmospheric water can condense to liquid water as well as to solid ice in the atmosphere, which is a unique property which no other gaseous component can achieve.

The next layer above is called the stratosphere. It extends from the top of the troposphere to about 50 km above ground. The well-known ozone layer, which absorbs high-energy ultraviolet light (UV, 220-300 nm) from the Sun and converts the UV energy into molecular movement (recognized as heat), is found within the stratosphere. Unlike the mesosphere, the stratosphere gets warmer with increasing altitude. Commercial passenger airplanes fly in the lower stratosphere, partly because it is a less turbulent layer than the troposphere underneath. Above the stratosphere is the mesosphere. It extends upward to a height of about 85 km above the Earth. In contrast to the thermosphere, the temperatures grow colder as one rises through the mesosphere. The coldest temperature in the Earth's atmosphere, of about -80 °C, can be found near the upper boundary. The layer above the exosphere is called the thermosphere. High-energy X-rays and UV radiation from the Sun are absorbed here by oxygen and nitrogen molecules and by their reaction product NO, increasing the temperature

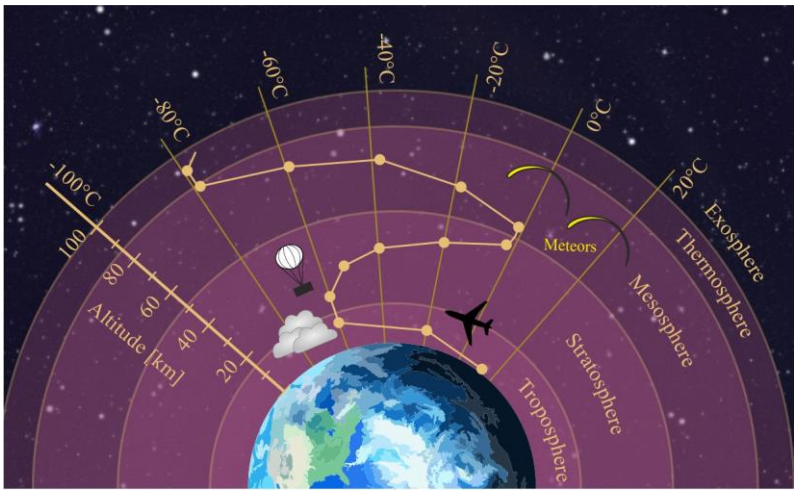

Figure 1-1 Earth's atmosphere divided into layers.

with increasing altitude. Due to the few molecules present at this altitude and the resulting low pressure (<0.01 mbar), the temperature is measured as the mean kinetic energy, or average speed of motion, of a molecule. Therefore, it has not been illustrated in Figure 1-1. The top of the thermosphere can be found between 500 and 1000 km above the ground. The aurora also referred to as northern or southern lights occur here. At this phenomenon, the ionization and excitation of nitrogen and oxygen molecules by solar winds, result in emissions of light with varying color and complexity.

The uppermost layer, the exosphere, gradually fades away into space and no clear-cut upper boundary can be defined. Therefore, the exosphere's upper boundary is suggested to be somewhere between 10,000 and 190,000 km above the surface of the Earth.

1.2 Clouds, Aerosols and Their Impact on the Climate System

Clouds appearing in the troposphere can be categorized into three groups: (i) warm clouds, (ii) mixed phase clouds and (iii) ice clouds. While warm clouds consist only of liquid water droplets, mixed phase clouds and ice clouds (also named cirrus clouds) have ice crystal content or consist completely of ice crystals. The water droplets in liquid and mixed phase clouds are formed by condensation of water vapor that has been evaporated from the planetary surface. They can reach sizes of up to 1 mm until they appear to be too heavy and form precipitation. All cloud types are important in terms of climate (Liou, 1986), transport of water vapor (Holton and Gettelman, 2001) and atmospheric chemistry (Abbatt, 2003). Thereby the presence of liquid water droplets or solid ice crystals in the cloud determines its properties and behavior (Wang, 2013). Due to strong changes of the dipole moment in the molecular vibrations of water and the respective high absorption coefficients and refractive indices in the infrared, clouds are able to absorb and reflect infrared radiation emitted from the Sun or the planetary surface. Pope and Fry (1997) determine only very weak light absorption in the visible range of liquid water. However, clouds can also influence visible light via Mie scattering and reflection (Mie, 1908).

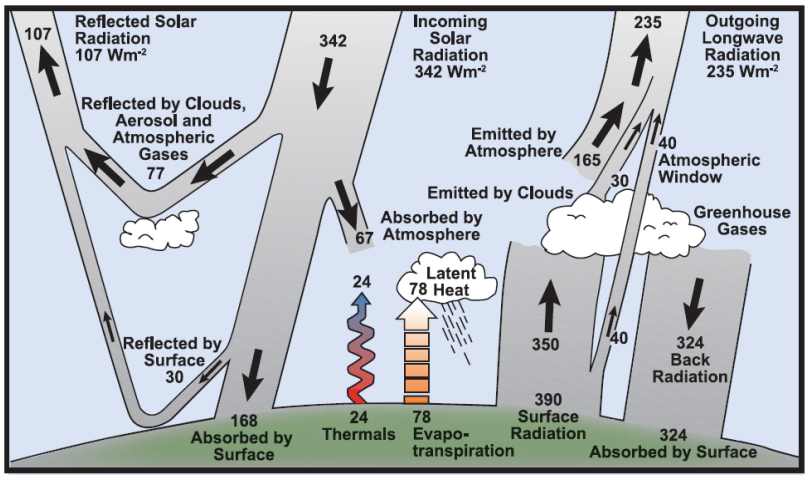

Figure 1-2 The Earth's annual global mean energy budget in Wm^{-2} based on Kiehl and Trenberth (1997).

Clouds play a major role with respect to the Earth's global energy budget (see Figure 1-2). The energy budget describes the heat and radiation flows to and from the Earth's surface. The state of aggregate is especially known to have a high impact on the absorption and emission properties of clouds and, in consequence, on the energy budget. Ice clouds reflect a higher ratio of incoming radiation back into space compared to liquid clouds, resulting in an increase of planetary albedo (Mishchenko et al., 1996). Furthermore, Shupe and Intrieri (2004) showed that long- and shortwave cloud forcing is a function of cloud temperature, height, emissivity (i.e., microphysics), cloud transmittance, surface albedo, and the solar zenith angle.

In the lower atmosphere the ambient conditions do not allow cloud droplets to freeze homogeneously (Pruppacher and Klett, 1997). Therefore, cloud-sized water droplets can occur in a supercooled state below -37 °C in the absence of a catalyzer, a so-called ice nucleating particle (INP). Aerosols acting as INPs are required to form ice particles because the nucleation is energetically hindered and not favorable in the troposphere under these conditions. Thus, droplets can freeze in principle at any temperature below 0 °C depending on the presence of the respective type of INP.

Aerosols can consist of solid and liquid particles of varying chemical composition, size and phase. Due to the wide range of variety, it is a big challenge to understand how they impact the climate and chemistry of the atmosphere. According to Lohmann and Feichter (2005), aerosol particles can affect the climate system via three physical mechanisms: (i) scattering and absorbing of solar radiation, (ii) scattering, absorbing and emitting of thermal radiation and (iii) acting as cloud condensation nuclei (CCN) and ice nuclei (IN). Aerosols can be divided into two main subgroups: (i) primary aerosols; containing particles introduced directly from their source into the gas (e.g. soot or pollen) and (ii) secondary aerosols, containing particles which are formed by gas-to-particle conversion (e.g. oxidation of SO_2 to H_2SO_4, leading to the attraction of air humidity and the formation of liquid droplets). However, aerosols are usually a composition of both subgroups with a variety of substances and sources, such as H_2SO_4 covered soot or organic layer coated mineral dust.

Aerosol particles serving as INP are rare compared to aerosol particles serving as cloud condensation nuclei (CCN) in the Earth's atmosphere (Pruppacher and Klett, 1997; Rogers et al., 1998; DeMott et al., 2010). Therefore, it is not surprising that many clouds persist in a supercooled liquid state. In general, the fraction of clouds which contain supercooled water droplets decreases with decreasing temperature, which reflects the results of theoretical calculations and laboratory studies summarized by Murray et al. (2012). These studies revealed that the number of aerosol particles capable of serving as INP increases with

decreasing temperature. Only a small proportion of aerosol particles can serve as INP at all temperatures. The substantial impact of INPs on the properties of clouds is in part because liquid clouds in supercooled state (below 0 °C) are thermodynamically unstable. A transition to a more stable state can occur promptly despite the system having persisted in a metastable state over a long period (Murray et al., 2008). The formation of a small fraction of ice crystals in a cloud can trigger a transformation of the whole cloud and substantially modify its properties. Since the solid state of water is more stable than supercooled water, ice crystals have a lower equilibrium vapor pressure (Murphy and Koop, 2005). This causes a water vapor concentration gradient between the air around the ice crystal and the supercooled water droplets. This leads to the growth of the ice crystals at the expense of supercooled water, which is known as the Bergeron-Findeisen effect (Pruppacher and Klett, 1997; Korolev, 2007). As a result, large ice crystals of a considerably lower concentration than the original liquid droplet concentration, appear. Furthermore, when ice crystals reach a critical size they can collide with supercooled droplets, which freeze in contact and lead to the formation of rain and hail.

Modes of Ice Nucleation

There are several ways in which INPs are thought to nucleate ice in the atmosphere: (i) Condensation freezing takes place when the particle acts as a CCN at temperatures below the melting point of ice and afterwards freezes at the same temperature. (ii) In contact freezing mode, the particle initiates the freezing when it collides with a supercooled droplet. (iii) The deposition mode involves the growth of ice directly from the vapor phase on the INP. (iv) In immersion mode, the INP is already suspended in the droplets before the droplet freezes. Nevertheless, studies summarized by Murray et al. (2012) showed that water saturation is a prerequisite for ice formation in mixed phase clouds and therefore either contact or immersion freezing is dominant. Since thermophoretic effects favor contact nucleation only in evaporating droplets, but these droplets tend to disappear before they can freeze, immersion freezing is suggested to be the most relevant mode in mixed phase clouds (Phillips et al., 2007). The nucleation modes are illustrated in Figure 1-3 and 1-4. These schemes however are model mechanisms and real life freezing modes are often not that well defined.

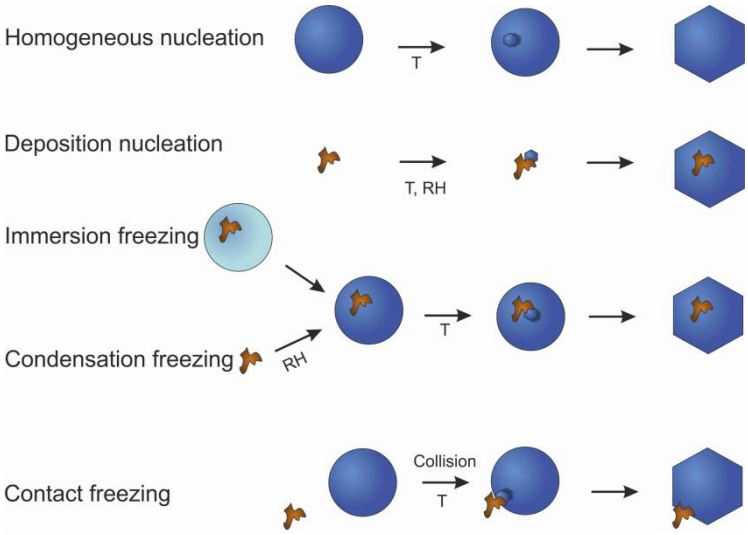

Figure 1-3 Schematic presentation of different nucleation modes.

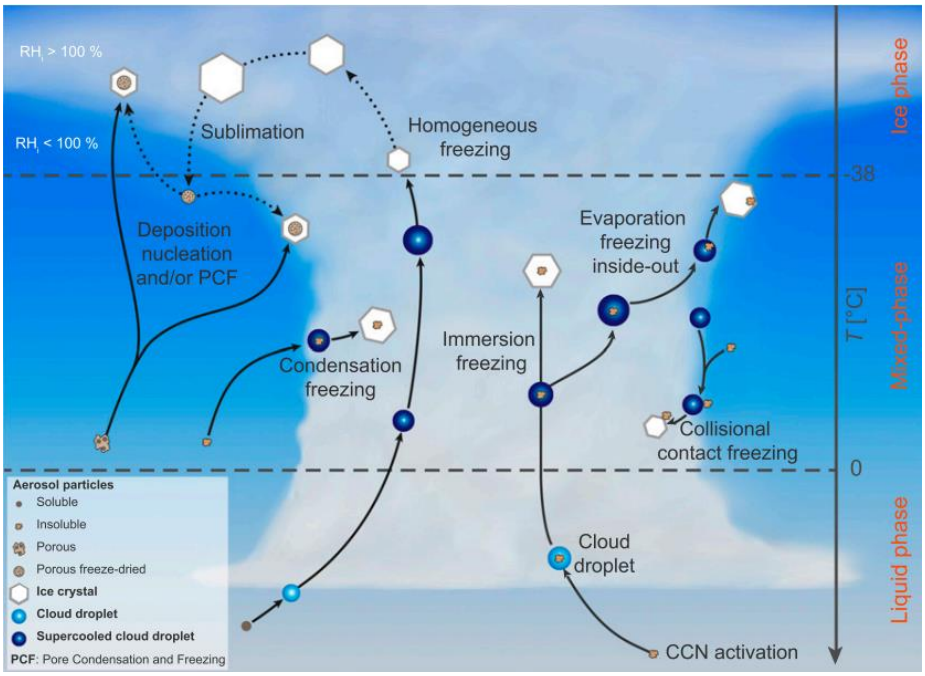

Figure 1-4 Schematic presentation of known ice nucleation pathways possible in the atmosphere (Kanji et al., 2017).

1.3 Classical Nucleation Theory (CNT)

An insight on the CNT given here is based on Murray et al. (2012). Although the CNT makes simplifying assumptions based on thermodynamics, observed trends can be reproduced exceptionally good (e.g. Huang and Bartell (1995)). It makes use of macroscopic values to estimate the rate at which the new phase nucleates. The CNT can be applied to the nucleation of ice from supercooled water or supersaturated water vapor as well as to the nucleation of amorphous materials from vapor. In general, the CNT can be applied to any situation in which a new phase nucleates from a metastable phase. Nevertheless, the CNT has several flaws. The CNT strongly depends on the interfacial energy, saturation and density but assumes that they appear to be the same for nano- as macroscopic-scaled materials. However, several studies revealed an actual size dependency of these factors which implies to evaluate results obtained using the CNT with caution (e.g. Bogdan (1997)).

1.3.1 Homogeneous Ice Nucleation

In pure water so-called clusters form and decay through the addition and removal of water molecules. The stability of these clusters is related to their size as well as the temperature. However, the formation of clusters above 0 °C is always a thermodynamically unfavorable process. If a cluster reaches a certain size in supercooled water, ice crystals are being formed. By calculating the Gibbs free energy of forming a cluster (ΔG_{Cl}), it can be shown that below a critical cluster size the addition of a new water molecule is endothermic, but above this threshold becomes exothermic and crystal growth can occur. ΔG_{Cl} consists of the amount of energy necessary to create an interface (ΔG_s) (which is always an endothermic process and therefore unfavorable) and the energy necessary for forming bonds between water molecules within the bulk of the cluster (ΔG_V) (which is exothermic if the saturation S with respect to a specific condensed phase is larger than 1) (Mullin, 2001).

$$\Delta G_{Cl} = \Delta G_S + \Delta G_V$$

Equation 1

For a spherical cluster, ΔG_{Cl} can be also expressed as:

$$\Delta G_{Cl} = -\frac{4\pi r_i^2}{3v} kTlnS + 4\pi r_i^2 \gamma$$

Equation 2

Where r is the radius of a cluster containing i water molecules, k the Boltzmann constant, γ the surface tension or surface forming energy and v the molecular volume of the condensed phase (Mullin, 2001). For ice nucleation from supercooled water, S can be calculated from the ratio of vapor pressure of liquid water and ice (P_l/P_{ice}). The critical cluster size r^* and Gibbs energy necessary to overcome the resulting energy barrier ΔG^* can be expressed as:

$$r^* = \frac{2\gamma v}{kTlnS}$$

Equation 3

and

$$\Delta G^* = \frac{16\pi\gamma^3 v^3}{3(kTlnS)^2}$$

Equation 4

The rate coefficient (J_{homo}, nucleation events per unit volume per unit time) at which ice crystals form in supercooled water can be expressed in Arrhenius form as:

$$J_{homo} = Ae^{\left(-\frac{\Delta G^*}{kT}\right)}$$

Equation 5

Since J_{homo} is the number of nucleation events per unit volume and unit time, it is widely used to evaluate experimental data using its form (Huang and Bartell, 1995):

$$J_{homo} = -\ln\left(\frac{1 - f_{ice}}{V\,t}\right)$$

Equation 6

with V being the droplet volume, t the observation time, and f_{ice} being the frozen fraction:

$$f_{ice} = \frac{n_{frozen}}{n_{total}}$$

Equation 7

Here n_{total} is the total number of droplets and n_{frozen} is the number of homogeneously frozen droplets.

1.3.2 Heterogeneous Nucleation

In contrast to the homogeneous nucleation, a suitable surface in contact with supercooled water can act as a catalyst and reduces the energy barrier necessary to form ice. By adapting Equation (5) the Arrhenius equation for heterogeneous nucleation coefficient (J_{het}) can be expressed as:

$$J_{het}(T) = A_{het}e^{\left(-\frac{\Delta G^* \varphi}{kT}\right)}$$

Equation 8

A_{het} is a pre-exponential factor in $cm^{-1}s^{-1}$ and φ is the factor by which the energy barrier is reduced relative to homogeneous nucleation.

The so-called ice nucleation active surface site density n_s (Demott, 1995; Connolly et al., 2009; Niedermeier et al., 2010; Broadley et al., 2012) can be used to describe heterogenous ice nucleation because the total surface area of INPs per droplet is important to their activity, as predicted by classical nucleation theory and confirmed by Edwards et al. (1962). n_{total} is the total number of droplets in the experiment, $n_{frozen}(T)$ is the number of frozen droplets at temperature T, and s is the particle surface per droplet. The fraction of frozen droplets $f(T)$ is given by:

$$f_{ice}(T) = \frac{n_{frozen}(T)}{n_{total}} = 1 - \exp\ [\ - n_s(T) \times s\ ]$$

Equation 9

The fraction of frozen droplets f_{ice} is multiplied by 100 to illustrate the values in percentage (e.g. see Chapter 3.1). The ice nucleating activity can be also expressed by referring to the number of active sites per mass of ice nucleating material (n_m) instead of the surface area per droplet. This expression is often used when the surface of the investigated INP cannot be accurately quantified.

Stochastic vs. Singular Nucleation

Heterogeneous ice nucleation can be described using a singular (time independent) or stochastic (time dependent) approach. The stochastic model is analogous to first-order chemical kinetics (Murray et al., 2012). It uses the homogeneous nucleation rate coefficient to predict freezing events of heterogeneous nucleation (see Equation (8)). However, contrary to the homogeneous coefficient, the heterogeneous coefficient is independent of volume but depends on the surface area of the INP in the water droplet (Iannone et al., 2011). This means that droplets with a different size/volume containing one single nucleus would each freeze at the same temperature (Hartmann et al., 2016). But if the nuclei are evenly distributed in the liquid, a droplet with more volume will contain more INPs than a droplet with less, and therefore freezes statistically at higher temperatures. However, for an even distribution of INPs throughout the sub-samples, the surface areas can be replaced by the droplet volume. The other approach to describe freezing experiments is the singular model, which neglects the time dependence and focusses on the specifics of nucleation sites (Vali, 1971). It assigns a characteristic temperature to each nucleating site and expresses the abundance of sites of various characteristic temperatures in terms of differential and cumulative nucleation spectra (Vali, 1971). In a mixture of nucleation sites, the freezing temperature depends on the site with the highest ice nucleation activity (INA) (Levine, 1950). Hereby the surface tension γ and, as a result, the contact angle θ at the three-phase point of droplets, surface and air is commonly used. The surface tension leads to a certain INA and can be used to interpret ice nucleation experiments (e.g. Chen et al. (2008)).

The stochastic and singular theorem differ in their basic approaches (Vali, 2014). Singular freezing experiments, which are commonly used to interpret ice nucleation experiments (e.g. Connolly et al. (2009); Crawford et al. (2011) or Wheeler and Bertram (2012)), only explain the onset freezing temperature. However, several experiments and models contradict the singular view (e.g. Welti et al. (2012) or Wright and Petters (2013)). One rather new approach is the so-called soccer ball model (Niedermeier et al., 2011). In this approach particles are assumed to be covered with different nucleation sites exhibiting different energy barriers, each following the stochastic rules of ice embryo formation.

However, it is important to note that there are at least three random contributions to heterogeneous freezing experiments with distributed samples: (i) molecular fluctuation of the ice cluster (ii) allocations of INPs in the sub-samples and (iii) location of the nucleating site on the surface of the INP.

1.4 Ice Nucleating Particles- INPs

Roughly four groups of different INP-types can be distinguished: (i) mineral dust, (ii) biological material, (iii) salts and (iv) carbonaceous particles (Pratt et al., 2009). Mineral dusts are spread into the atmosphere from a range of sources e.g. arid regions in Africa or the Middle East (Prospero et al., 2002). They were shown to serve as effective ice nuclei in several studies summarized by Murray et al. (2012). Although it is known that biological materials can act as INP, their roles in ice formation in clouds remain poorly understood. A wide variety of sources, including fragments of plants and animals, pollen, fungal spores, bacteria and virus particles, can be found (Deguillaume et al., 2008). Discussions of the impact of biological INPs on the ice formation process were featured in several recent reviews (Szyrmer and Zawadzki, 1997; Phillips et al., 2008; Hoose and Möhler, 2012). Salts were thought to be unable to act as INP due to their solubility in water (Pruppacher and Klett, 1997). Nevertheless, studies proved that salts such as ammonium sulfate (Zuberi et al., 2001) and oxalic acid (Wagner et al., 2011) nucleate ice in the immersion mode. Sea salt plays a major role as INP, especially above the sea and regions close to the coast.

There is an immense variety of nucleating relevant properties associated with INPs. Pruppacher and Klett (1997) listed a number of required features of effective INPs as: (i) insolubility of the INP to prevent disintegration, (ii) size (a correlation of "larger" aerosol particles and INA has been reported by DeMott et al. (2010) and Pruppacher and Klett (1997)), (iii) chemical bonding of the INP's surface with water and (iv) crystallographic aspects, that is, an effective INP should template ice. These commonly cited required features need to be taken with caution since they have been disproven several times over the past decade, revealing that these criteria are too narrow (Murray et al., 2012). Nevertheless, the surface composition and specific molecular features (ice nucleation active sites) are likely to be important. As an example, they might support the formation of so-called "charge-assisted hydrogen bonding" allowing interactions with water molecules, thus increasing the INA (Steiner, 2002).

The surface composition of aerosol particles can differ depending on physical state, surface structure, distribution of functional groups and environmental chemistry of active sites (Coluzza et al., 2017). Additional information on surface features supporting ice nucleation are needed in terms of spatial expansion, surface crystallographic structure, and chemical composition. Functional groups (see Figure 1-5) or structures may influence the hydrophilicity or hydrophobic interactions and therefore the ability to nucleate ice.

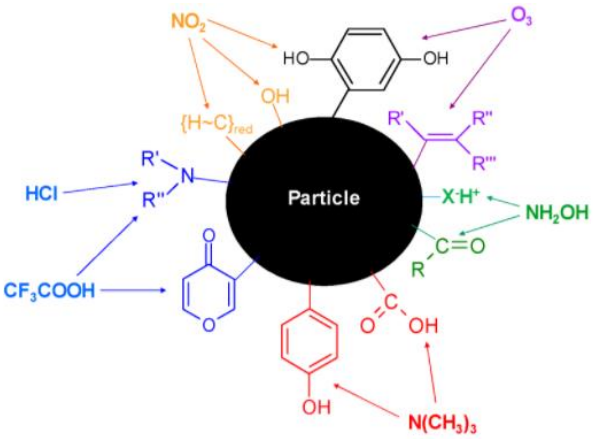

Figure 1-5 Scheme of surface functional groups potentially acting as ice nucleation active sites and affecting the ability to nucleate ice (Coluzza et al., 2017). Reactive molecules as O_3, NO_2, HCl, CF_3COOH, $N(CH_3)_3$ and NH_2OH can influence the chemical properties of the interface.

Moreover, the crystallographic aspects and microstructure of INPs are likely to be important ice nucleating features. Recent studies have shown, that a crystallographic similarity to ice¸ as suggested by Pruppacher and Klett (1997), is not necessary to trigger ice formation (Lupi et al., 2014; Lupi and Molinero, 2014). Their results indicate that even amorphous lattice structures can nucleate ice.

Beside the lack of knowledge of required features, also nucleation mechanisms are still not fully understood. Using computer simulations, a molecular understanding of ice nucleation can be obtained (Matsumoto et al., 2002; Sanz et al., 2013; Lupi et al., 2014; Lupi and Molinero, 2014). In general, three different kinds of models are used in recently published computational studies: (i) The fast and simple monoatomic coarse grained mW water model (Molinero and Moore, 2009; Bianco et al., 2017), (ii) the more accurate but computationally demanding all atom water models (Abascal et al., 2005; Abascal and Vega, 2005), and (iii) the very general but accurate model using calculations of forces and energies from first principles electronic structure based on density functional theory or other methods.

These simulations showed, that the mechanisms of heterogeneous ice nucleation are influenced by several independent molecular properties as the surface hydrophobicity (Lupi and Molinero, 2014), surface morphology (Cox et al., 2012), and local electric fields (Yan and Patey, 2011). Consequently, the investigation of INA needs to be done including the influence of different molecular properties, such as water-substrate interactions and surface morphologies.

In general, it can be said that due to contradicting results and opened questions of ice nucleating features and ice nucleating mechanisms, predictions must be taken with care.

1.5 Ice Nucleation - State of the Art

INPs are shown to play a major role in the ice forming process in clouds and therefore the Earth's climate system. The composition and origin of INPs have been studied intensively over the last few decades, as summarized e.g. by Murray et al. (2012). However, the processes and mechanisms of heterogeneous ice nucleation remain poorly understood (Kärcher and Lohmann, 2003). To answer the major question of ice nucleation: What makes an effective ice nucleating site? — further investigations of omnipresent INPs are needed. For this aim simple proxy INPs as a surrogate for more complex INPs, are very suited and often give decisive laboratory results which then can be used for field experiments or model calculations. Moreover, the commonly used vial-shaking lab bench technique reveals several obstacles. Further developments were needed to improve the investigation of droplets with diameters down to 20 µm in a wide temperature window down to -37 °C.

Portions of this chapter, which were previously published as *The Ice Nucleation Activity of Graphene and Graphene Oxides* in *The Journal of Physical Chemistry C* (Häusler et al., 2018a), *Freezing on a Chip–A New Approach to Determine Heterogeneous Ice Nucleation of Micrometer-Sized Water Droplets* in the Journal *Atmosphere (Häusler et al., 2018b)* and *The Ice Nucleation Activity of Black and Brown Soot Aged by Exposure to NO_2 and SO_2* in the *Journal of Geophysical Research- Atmosphere* (Häusler et al., submitted 2018), have been partially reproduced.

1.5.1 Lab Bench Droplet Freezing Techniques

In order to study freezing processes in the laboratory, several experimental approaches have been employed in the past, such as cloud chambers, continuous-flow diffusion chambers, levitation in an electrodynamic balance, acoustic levitation, and different kinds of lab bench droplet-freezing setups (Cziczo et al., 2017). Lab bench droplet-freezing devices can be distinguished based on their droplet generation technique into four groups (see Table 1-1): (i) Piezo-driven generator (Peckhaus et al., 2016), (ii) generation via micro-pipetting (Stopelli et al., 2014; Budke and Koop, 2015; Whale et al., 2015a; Polen et al., 2016; Tobo, 2016; Zaragotas et al., 2016), (iii) flow-focusing generator (Stan et al., 2009; Riechers et al., 2013), and (iv) the generation via shaking of a water-oil emulsion in a vial (herein called the vial-shaking technique) (Pummer et al., 2012; Wright and Petters, 2013; Pummer et al., 2015;

Zolles et al., 2015). Generated volumes range from 4 pL (from the vial-shaking technique), to 0.5 nL (from the flow-focusing generator), and up to 400 µL (from the pipetting technique).

While an increased volume allows the quantification of much smaller values of ice nucleation active surface site density n_s (Whale et al., 2015a), the temperature range in which ice nucleation experiments can be done becomes restricted. The volume dependence of the homogeneous freezing temperature shifts the freezing temperature of ultrapure water to higher temperatures (Vali, 1971). Moreover, contamination of ultrapure water droplets with diameters of >1 mm can cause heterogeneous ice nucleation at higher temperatures of about −20 °C (Whale et al., 2015a).

Nevertheless, the vial-shaking technique has been used in our laboratory for several years and enables the investigation of INA of droplets with diameters down to 20 µm (4 pL volume) in a wide temperature range down to −38 °C (see Table 1-1) without any restrictions (Pummer et al., 2012; Pummer et al., 2015; Zolles et al., 2015).

However, several issues can occur in the application of this technique. (i) Droplets show a rather broad size distribution, so a more elaborate analysis as the individual calculation of surface area present in each single droplet, is required (Pummer et al., 2012; Pummer et al., 2015; Zolles et al., 2015). (ii) Contact between droplets can lead to possible droplet–droplet interactions during the freezing process. Frozen droplets can act as INP themselves for yet unfrozen ones (herein called infectious freezing). (iii) The interface between droplets and the oil matrix can interfere with the nucleation process. If a hydrophobic INP (e.g., graphene) is immersed in an oil-water mixture, it is possible that the hydrophobic sample gets drawn into the oil phase (Pummer et al., 2012). This possibility is especially true during the shaking process when a high kinetic energy is applied, increasing the probability of hydrophobic INPs getting drawn into the oil matrix. This migration can significantly lower the concentration of the INPs in the water droplets. However, a precise quantification of this effect is rather difficult. (iv) Partial crystallization and changes in viscosity of the oil matrix due to decreasing temperatures can cause impaired vision. All these issues can cause more labor intensive evaluation and false positive or false negative freezing events (Hauptmann et al., 2016). New approaches for droplet-freezing experiments aiming to reduce these issues as e.g., a nonuniform droplet size distribution, while still providing the ability to create small droplets and to investigate them in a wide temperature range, are needed.

Table 1-1 Comparison of the main features of different lab bench freezing devices.

Freezing Device	Generation of Sample Volumes	Reference	No. of Observed Sample Volumes Per Experiment	Sample Volumes	Freezing Temperature of Water without Added INPs (°C)
Nanoliter droplet freezing assay	Piezo-driven droplet-on-demand generator	Peckhaus et al. (2016)	1500	215 ± 70 pL	−36
Bielefeld Ice Nucleation Array (BINARY)	Pipetting into compartments	Budke and Koop (2015)	36	~1 µL	−34
LED-based Ice Nucleation Detection Apparatus (LINDA)	Separated compartments (Eppendorf Safe-Lock)	Stopelli et al. (2014)	52	40 to 400 µL	−15
Microplate partially submersed in cooling liquid	Separated compartments (plastic microplate)	Zaragotas et al. (2016)	96	≤400 µL	−17.26
Carnegie Mellon University Cold Stage (CMU-CS)	Syringe or micropipette	Polen et al. (2016)	30–40	~0.1 µL	−20
Microliter Nucleation by Immersed Particle Instrument (µl-NIPI)	Micropipette	Whale et al. (2015a)	40	~1 µL	−20
Cryogenic Refrigerator Applied to Freezing Test (CRAFT)	Micropipette	Tobo (2016)	49	5 µL	−30
WeIzmann Supercooled Droplets Observation (WISDOM)	Flow-focusing droplet generator	Reicher et al. (2018)	120–550	~0.03 and 0.5 nL	−38
Microfluidic apparatus	Flow-focusing droplet generator	Stan et al. (2009)	>10.000	~0.3 nL	−36
Droplet freezing assay	Shaking of a water-oil emulsion in a vial	Wright and Petters (2013)	300–1500	0.06 to 8 nL	−34
Droplet freezing assay	Shaking of a water-oil emulsion in a vial	Pummer et al. (2012)	20–40	4 to 30 pL	−37
Freezing on a chip	Filled cavities on a silicon/gold chip	Häusler et al. (2018b)	25	4 to 300 pL	−37.5

1.5.2 Soot as Ice Nucleating Particle

Even though the tremendous soot concentrations in the atmosphere monitored in the early 1950s was reduced by the Clean Air Act of 1956 due to the use of soft coal and domestic heating (Auliciems and Burton, 1973), a series of studies demonstrated that black carbon as well as organic soot components continue to be a large fraction in urban aerosols (Novakov et al., 1974; Chang and Novakov, 1975; Rosen et al., 1980). The impact of soot as an aerosol particle on the radiation budget within the atmosphere was reviewed by Ramanathan et al. (2001). It showed that soot is even present in remote oceanic regions, raising the possibility of hemisphere-wide dispersal. Depending on the organic content of soot, the presence of trace amounts of soot can result in a large atmospheric solar absorption, which reduces substantially the solar radiation reaching the surface. Soot can absorb the solar radiation on the top-of-the atmosphere TOA (reflected by the surface and clouds). As a result, this reduces the solar radiation reflected to space, resulting in a positive TOA aerosol forcing (that is, the change in the outgoing long-wave radiation), in contrast to the negative forcing at the surface. Whether the Earth's surface will cool or warm in response to soot induced aerosol forcing depends on the small details of how the surface and the atmosphere interact with each other. As a result, different regions of the planet may respond differently, both in magnitude and in sign.

a. Structure of Soot

Soot is ubiquitous in the Earth's troposphere (Heintzenberg, 1989) and is defined as a particulate primary, carbonaceous product from an incomplete combustion process of natural or anthropogenic origin (Gorbunov et al., 2001). Many details of soot formation remain poorly understood, but there is an agreement on the general steps involved, which are summarized by Richter and Howard (2000). A schematic representation of the formation process is given in Figure 1-6.

The formation process can be divided into six steps: (i) The formation of molecular precursors of soot: Molecular precursors are thought to be heavy polycyclic aromatic hydrocarbons (PAH) with a molecular weight of 500 to 1000 amu (atomic mass unit). The formation of PAHs appears to involve the growth of small molecules as benzene by adding small carbon units as C_2 and C_3. The exact pathway of the growth reaction strongly depends on the fuel. (ii) The nucleation or inception of particles from heavy PAH molecules: In this step, molecular mass is converted into particulate mass. Heavy PAH molecules become soot particles with a mass of about 2000 amu and an effective diameter of 1.5 nm. (iii) The mass growth of

particles: The mass of soot particles increases via the addition of gas phase species as acetylene and PAH. During this process, the number of soot particles remains the same. (iv) The coagulation via reactive particle-particle collision: Sticking collision of particles during the mass growth process increases the particle size and decreases the particle number. (v) Carbonization of particulate material: At longer period under pyrolytic conditions in the post flame zone, the polyaromatic soot particles undergoes addition reactions as functional group elimination, cyclization, ring condensation and ring fusion. During this reactions, dehydrogenation, growth and alignment of polyaromatic layers takes place, leading to the conversation of initially amorphous soot material to a more graphitic carbon material. (vi) the oxidation: Oxidation of soot particles decreases the mass through the formation of CO and CO_2. It can occur during the formation of soot or subsequently to formation, depending on the flame type. The main oxidation reactants are OH, O and O_2.

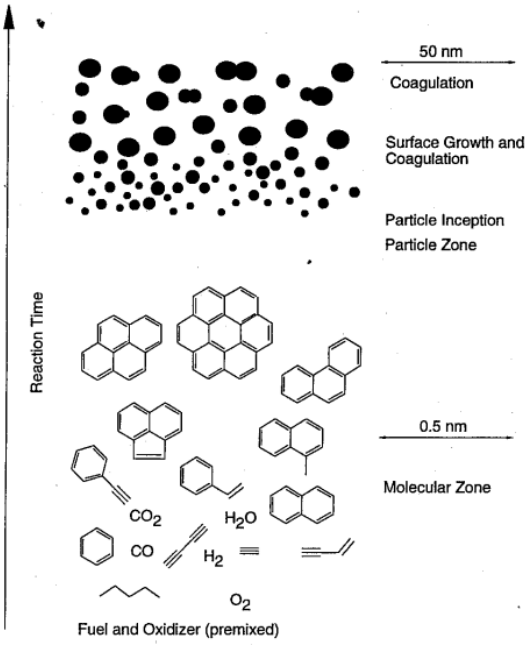

Figure 1-6 Rough schematic representation of soot formation in premixed flames (Bockhorn, 1994).

According to Kim et al. (2015) and Mamakos et al. (2013), the structure and composition of the soot particles generated by combustion, strongly depends on the burning conditions. An oxygen rich flame results in agglomerates of small spherical primary soot particles (see Figures 1-7 to 1-9), which are typical structures for diesel exhaust particles (Kim et al., 2015). These particles are called black carbon and reveal a high portion of elemental (highly ordered graphitic-like structure) and low portion of organic carbon. Oxygen poor burning conditions, on the other hand, reveal less graphitic-like structures and a higher amount of organic carbon

including organic and inorganic components (aliphatics, sulfate, metal oxides, etc.) (Laskin et al., 2015).

Soot carbon consists of agglomerates (see Figure 1-7) typically formed, ranging in diameter from about 1 to 100 µm (McCunney et al., 2012). These clusters consist of ten to thousands of strongly attached aggregates (85-500 nm in diameter), which are held together by van der Waals forces. Work by Gray and Muranko (2006) concluded that although agglomerates can be seen as temporary structures due to the absence of chemical bonds or weld, they persist as large clusters under typical manufacturing and use conditions. The chain-like aggregates consist of nano-spherical particles (primary particles) with diameters of 15 to 300 nm (see Figures 1-7 to 1-9). Primary particles form the basic unit of soot aggregates (Levy et al., 2012). They consist of turbostratically stacked and concentric sheets of condensed aromatic ring systems, revealing a graphitic-like structure as i.e., graphite platelets (see Figure 1-8). These sheets are formed by 3 to 4 stacked polyaromatic carbon layers with an average lateral extension of up 3 nm and interlayer distances of about 3.5 Å.

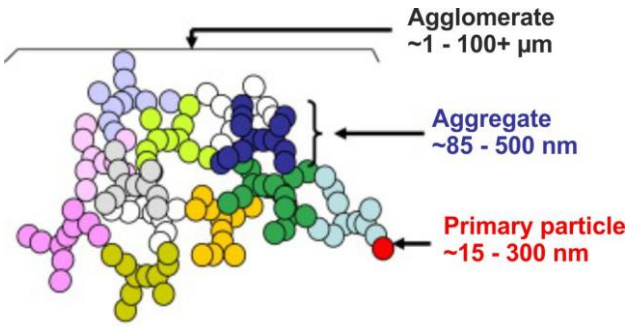

Figure 1-7 Structure of black carbon particles (Long et al. (2013), Copyright 2006 Lippincott Williams & Wilkins, Inc.).

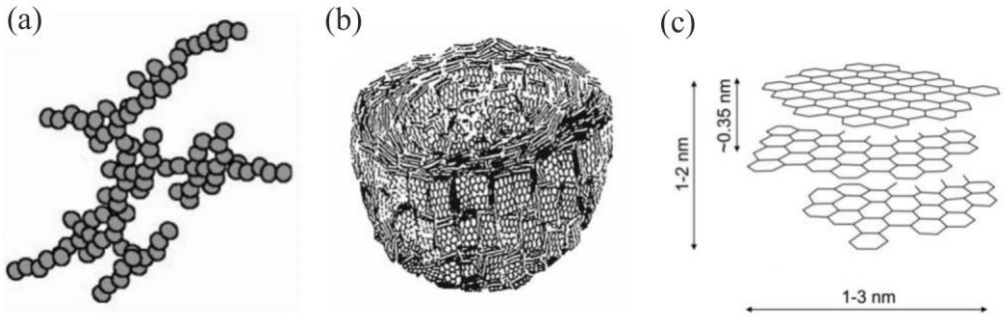

Figure 1-8 Schematic representation of black carbon aggregates and primary particles (Pawlyta and Hercman, 2016): (a) a soot aggregate composed of nano-spherical primary particles; (b) nano-spherical primary particle internal structure showing stacked carbon layers (Heidenreich et al., 1968); (c) basic unit of primary soot particle– ordered domain consists of 3-4 stacked carbon layers.

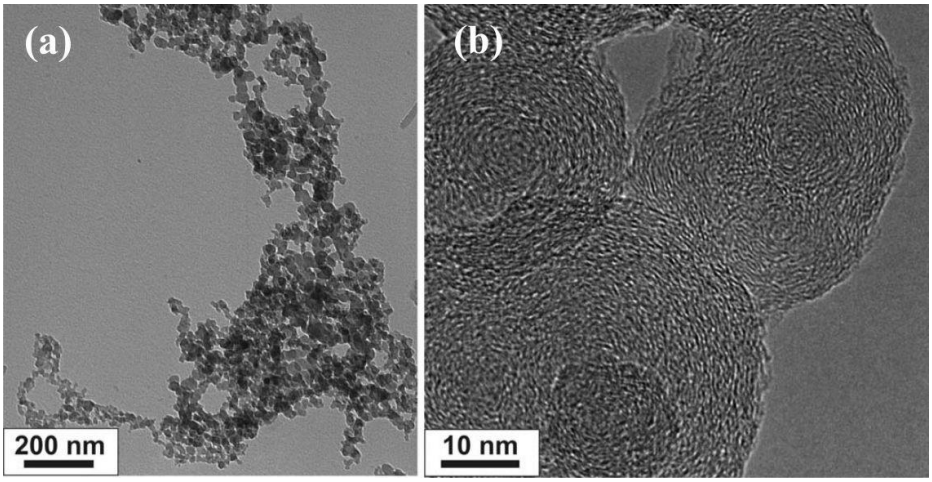

Figure 1-9 TEM images of typical diesel soot (Pawlyta and Hercman, 2016): (a) soot aggregate showing chain-like structure and (b) nano-spherical primary particles showing concentrically stacked carbon layers.

b. Ice Nucleation Activity of Soot

There is evidence that graphite-like carbon particles as soot can trigger the formation of ice crystals even though the fact that they are naturally hydrophobic has been known for a long time (Garten and Head, 1964). Soot may become partially hydrated by oxidation or by deposition of water-soluble species present in the air, such as sulfuric acid and nitric acid (Wyslouzil et al., 1994; Chughtai et al., 1996), and therefore may have increased INA.

If fresh or aged soot particles, which are omnipresent in the atmosphere, are indeed effective INPs, they have the potential to fundamentally impact the Earth's climate by changing the properties of ice crystal containing clouds (DeMott et al., 1997; DeMott, 2002; Lohmann, 2002; Gierens, 2003; Lohmann and Feichter, 2005). For example, an increase in soot concentrations may lead to more frequent ice nucleation in the lower troposphere, thus increasing the ice phase induced precipitation (Dymarska et al., 2006). Increased soot concentrations may also cause a reduction of clouds in the lower troposphere and result in increased absorption of solar radiation (Lohmann, 2002; Lohmann and Feichter, 2005). Investigations of the INA of (aged) soot particles are therefore crucial to understand the effect of soot on global climate.

Several studies showed that an increase in the hydrophilicity upon oxidation can enhance the INA of aged soot (Gorbunov et al., 2001; Zuberi et al., 2005; Kärcher et al., 2007; Knopf et al., 2010; Pratt et al., 2010; Friedman et al., 2011). Oxidation, however, also impacts the nanostructure of soot, making it difficult to assess the separate effects of soot lattice/nanostructure and hydrophilicity in experiments. Recent molecular dynamics simulations indicated that the hydrophilicity of the surface is not necessarily a good predictor

of INA. Knowledge of the actual nanostructure and spatial distribution of chemical groups in soot and other atmospheric carbon particles is also required to make an accurate prediction of the ice nucleating ability of these particles (Lupi and Molinero, 2014).

Dymarska et al. (2006) investigated the deposition freezing properties of a range of different types of soot, including soot that had been treated with atmospherically relevant amounts of ozone. The authors noticed that the INA of ozone-treated and untreated soot did not differ significantly. They confirmed that ice nucleation on many types of soot particles was not efficient below water saturation at temperatures above -25 °C (DeMott, 1990; DeMott et al., 1999; Möhler et al., 2005a; Möhler et al., 2005b). However, several reports suggested that it may be effective in condensation or immersion mode (DeMott, 1990; Diehl and Mitra, 1998; DeMott et al., 1999; Gorbunov et al., 2001; Möhler et al., 2005a; Möhler et al., 2005b; Dymarska et al., 2006).

On the other hand, Gorbunov et al. (2001) found that soot particles of various sizes are ice nucleation active in a temperature range from -5 to -20 °C. They found that the fraction of aerosol particles forming ice crystals was influenced by the degree of oxidation of the soot particle surface. They suggested that oxidation affected the concentration of surface chemical groups that could form hydrogen bonds with water molecules, leading to an increased INA (Gorbunov and Safatov, 1994). Brooks et al. (2014) confirmed these results and showed that the mean freezing temperatures of freshly produced soot particles of −19 to −24 °C shifted by 2-3 °C to higher temperatures after exposure to ozone. Moreover, they reported that a fraction of the oxidized soot particles froze at temperatures above −10 °C, increasing the temperature range in which soot is ice nucleation active.

The INA of combustion particles present in the exhaust of jet engines was investigated by Diehl and Mitra (1998). They reported that soot particles can already act as INPs at higher temperatures than those at cruise altitude, implying that soot in aircraft exhaust can form ice crystals heterogeneously. Schumann et al. (1996) observed the impact of different sulfur mass fractions in jet aircraft fuels on the aircrafts' contrails. Their results indicate that part of the fuel sulfur converted to sulfuric acid, which nucleates with water vapor heterogeneously on soot or nucleates acid droplets homogeneously, causes different contrail properties e.g. particle size distribution and optical thickness.

Raman spectroscopy allows the characterization of a wide range of chemical substances (McCreery, 2000; Ivleva et al., 2005; Sadezky et al., 2005). A correlation between the structure of soot and Raman spectroscopic parameters has already been reported (e.g. Dippel et al. (1999), Ivleva et al. (2007) and Sadezky et al. (2005)). Knauer et al. (2009) applied

Raman spectroscopy to obtain detailed information about the reactivity of soot by determining its lattice structure. They showed that soot can exhibit complex heterogeneous structures which include graphitic and nonplanar molecular parts (basic structural units). As a result, four different kinds of disorder (surfaces, edges, amorphousness and impurities/polyenes) in the graphite lattice must be considered with respect to the reactivity of soot. Furthermore, soot can contain graphene nanoribbons, whose curvature has also been identified as a crucial parameter defining the reactivity of soot (Müller et al., 2007).

Various competing atmospheric aging processes may be responsible for the contradictory results in the literature reporting either an increase, decrease or permanence of INA (Dymarska et al., 2006; Friedman et al., 2011; Wang and Knopf, 2011; Chou et al., 2013; Kanji et al., 2013; Li et al., 2014).

1.5.3 Graphene and Graphene Oxides as Ice Nucleating Particles

As shown above, the INA of soot was investigated intensive over the last decades. Nevertheless, the complexity of atmospheric soot makes the forecast of their ice nucleating behavior rather difficult. To gain a fundamental understanding of the INA of soot, a chemically and structurally related proxy INP like graphene needs to be investigated.

A series of studies demonstrated that black carbon as well as organic soot components form a large fraction of urban aerosols (Novakov et al., 1974; Chang and Novakov, 1975; Rosen et al., 1980). The ice nucleation activity of soot has been well investigated, for example, by DeMott (1990) and Dymarska et al. (2006). Nevertheless, the complexity of atmospheric soot makes forecasts of their ice nucleating behavior rather difficult. Several laboratory and field studies showed that an increase in the INA of aged soot results from an increase in the hydrophilicity of the surface upon oxidation (Zuberi et al., 2005; Kärcher et al., 2007; Knopf et al., 2010; Pratt et al., 2010; Friedman et al., 2011). However, oxidation also impacts the nanostructure of soot, making it difficult to assess the separate effects of soot nanostructure and hydrophilicity via experiments. Therefore, the investigation of graphene, a simple proxy substance with chemical and structural similarities to soot (Richter and Howard, 2000; Cooper et al., 2012), may confirm or correct the established rules regarding the necessary ice nucleation characteristics. Graphene is a single two-dimensional layer of carbon atoms bound in a hexagonal lattice structure (Cooper et al., 2012). It was first isolated and identified in 1962 by Hanns-Peter Böhm (Böhm et al., 1962). Since then, graphene has been the focus of extensive studies, primarily due to its exceptional electrical, thermal and mechanical properties (Böhm, 2010).

Lupi and Molinero (2014) used molecular dynamics simulations to investigate the effect of changes in the hydrophilicity of model graphitic surfaces on the freezing temperature of ice. Their results indicate that the ordering of liquid water in contact with the surface plays an important role in the heterogeneous ice nucleation mechanism and that the hydrophilicity of the surface is not generally a good predictor of the INA. These ordered water molecule domains of bilayer hexagons are necessary for the INA of graphene but have not been observed on hydrophobic or hydrophilic atomically rough surfaces. They suggested that knowledge of the actual nanostructure and spatial distribution of chemical groups in soot and other atmospheric carbon particles is needed for an accurate prediction of the INA of these aerosols.

A molecular dynamics study by Bi et al. (2016) revealed that a crystalline graphitic lattice with an appropriate hydrophilicity may indeed template ice and thus significantly enhance its INA. Their calculations demonstrated that the templating effect is found to transit from within the first contact layer of water to the second as the hydrophilicity increases, yielding an oscillating distinction in the INA of crystalline and amorphous graphitic surfaces. Furthermore, it was evident that crystalline graphene becomes up to 10^5 times more efficient within certain hydrophilicity ranges, suggesting that the crystallinity is also a key factor for ice nucleation under such hydrophilicity. The experimental investigation of Zheng et al. (2013) showed that a sprinkle of graphene oxide nano-flakes is effective for condensing water nano-droplets and seeding ice epitaxy on graphite under ambient conditions. They discovered that ice nucleation and growth can be influenced by modifying the functional groups of graphene oxide nano-flakes and by intermolecular hydrogen bonding between nano-flakes. Carboxylate groups introduced by base treatment play a key role in the INA of graphene oxide nano-flakes. So-called “charge-assisted hydrogen bonding” (Steiner, 2002) allows interaction with water molecules, thus increasing the INA. Reduction via acid or ammonium treatment decreases the INA significantly. Furthermore, by arranging graphene oxide nano-flakes in one dimension, an ice-like structure can be induced, leading to an increase in the INA. A phenyl ring structure, however, reduces the number of possible hydrogen-bonding carbonyl sites for ice nucleation and decreases the INA.

Whale et al. (2015b) investigated different kinds of carbon nanomaterials in laboratory experiments using an immersion freezing technique. Their results agreed with the calculations done by Lupi and Molinero (2014) and Lupi et al. (2014) and showed that materials with a lower oxidation state nucleate ice more efficiently than materials with a higher oxidation state. Any oxidation, roughness or curvature was found to decrease the observed nucleation

temperature. The result that oxidized surfaces nucleate ice less well than atomically flat surfaces is somewhat in contradiction with the commonly stated “chemical bonding” requirement for ice nucleation (Pruppacher and Klett, 1997). Oxides or other polar groups on the surface of INPs are meant to offer so-called functional sites that are able to interact with water molecules and nucleate ice.

Biggs et al. (2017) modified graphene oxides by means of thiol–epoxy chemistry, resulting in materials with increased INA. They revealed that hydrophobic chains increased the heterogeneous nucleation temperature from -22.5 °C to -12.5 °C. Hydrophilic surface modifications did not promote the activity but also did not reduce the underlying INA of the graphene oxide. They suggested that due to the functionalization and increase in hydrophobicity, an increased degree of aggregation occurred, with larger aggregates potentially leading to more nucleation. Ammonia is highly relevant in the atmosphere, as it has been shown to play a primary role in the formation of secondary particulate matter, forming ammonium-containing aerosols (Behera and Sharma, 2010). Ammonium-containing aerosols constitute the major fraction of $PM_{2.5}$ aerosols in the atmosphere.(Behera and Sharma, 2010) Anthropogenic ammonia originates, for example, from soil due to agriculture activities and from industrial and traffic emissions (Pandolfi et al., 2012; Phan et al., 2013).

Due to the differences in approaches concerning the required features of an INP, investigations of simple and closely related INPs are important to gain more information on the characteristics of a functional site. Therefore, graphene was chosen to be a good proxy substance to fundamentally understand heterogeneous ice nucleation of carbonaceous particles.

1.5.4 Cellulose as Ice Nucleating Particle

Cellulose [β(1,4)-linked D-glucose polymer] is a main component of biological cell walls. It occurs in green plants as macromolecule with a polymerization degree in the range of 300–3000 and in certain cases, e.g. in fibers of cotton seeds up to 15,000 (Bunbury, 1925). Linear macromolecules form micelles via hydrogen bonding called micro fibrils (Denffer, 1978). Plant seeds with visible white fibers are pure cellulose and are referred to as free cellulose, since it is directly accessible for saccharification. Leaves of terrestrial plants consist of around 50% cellulose, around 20% lignin and 20–30% hemicelluloses (Butler and Bailey, 1973). It is assumed that the major fraction of cellulose in continental aerosol originates from decomposition processes of leaves. Kunit and Puxbaum (1996) showed that that plant debris is a major contributor to organic carbon in atmospheric aerosols. Further sources of cellulose are pollen (Stanley and Linsken, 1985), and cellulose producing bacteria, e.g. Acetobacter xylinum.

Airborne cellulose accounts for more than 5% (up to 22%) by mass of the total airborne organic matter throughout the year (Sanchez-Ochoa et al., 2007) and is ubiquitous in the atmosphere (Nishiyama et al., 2002; Quiroz-Castañeda and Folch-Mallol, 2013). Moreover, high concentrations of atmospheric cellulose, of about 0.4 µg m^{-3} (see Figure 1-10), were estimated in an urban environment and attributed to the plant debris emitted at or near ground level (Kunit and Puxbaum, 1996; Puxbaum and Tenze-Kunit, 2003). Due to the seasonal cycles of deciduous trees and the decay processes of the leaf litter, large fluxes of the decay products in the atmosphere occur (Brimblecombe, 1986; Kunit and Puxbaum, 1996).

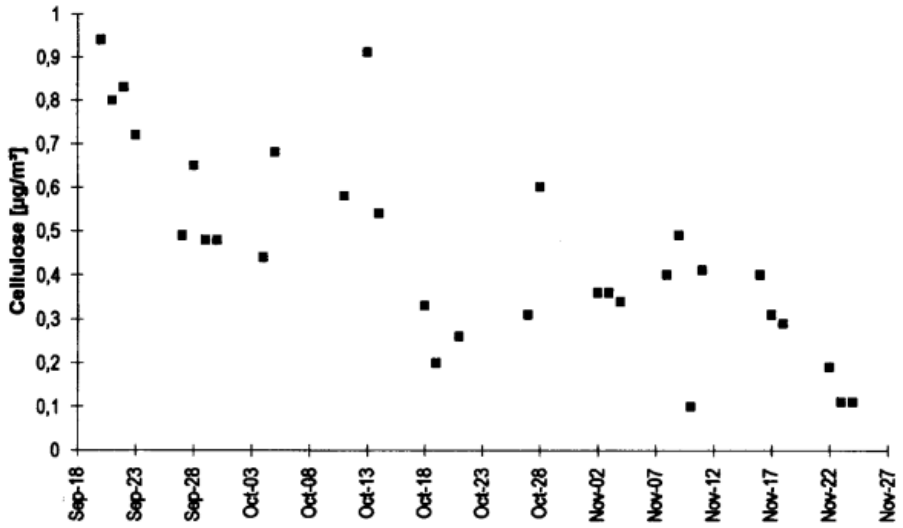

Figure 1-10 Atmospheric cellulose concentration in Vienna (Kunit and Puxbaum, 1996).

Very little is known about the INA of cellulose. Carbonaceous aerosol particles of biological origin are known to be efficient INPs at modest levels of supercooling (summarized e.g. by Murray et al. (2012)). Yet it remains unclear which compound of this type of INP nucleates ice. Likely candidates are carbohydrates or oxidized polymers. Furthermore, the connection between their atmospheric abundance and their influence on cloud development is still uncertain (Atkinson et al., 2013). Hiranuma et al. (2015) reported that microcrystalline cellulose particles can act as INP in simulated supercooled clouds at temperatures below about -21 °C, temperatures relevant for mixed-phase clouds.

2. Objectives

The main aim of the work presented is to give an answer to the major question: What makes an effective ice nucleating particle? Studies in the last few decades trying to solve this puzzle contradict each other partly or just provide insufficient answers. With the results obtained from this work, an additional jigsaw piece shall be added to the heterogeneous ice nucleation-puzzle.

The specific objectives of the work presented are as follows:

I. Enhancement of measurement instrumentation to determine INA (see Chapter 4):
   The vial-shaking lab bench technique, used for recent studies in our laboratory, reveals several obstacles. Further developments were needed to improve the investigation of droplets with diameters down to 20 µm in a wide temperature window.

II. Investigation of proxy model INPs (see Chapter 5):
   To gain a fundamental understanding of heterogeneous ice nucleation, a possible link between INA and lattice structure, microstructure and chemical composition was investigated.

III. Production and aging of aerosol particles (see Chapter 6)

IV. Investigation of produced aerosol particles (see Chapter 6):
   Previously stated links were applied to self-produced aerosol particles, to demonstrate that proxy INPs can be used to predict the INA of other aerosols.

V. Modification and correction of stated correlations

VI. Fundamental insight into heterogeneous ice nucleation of carbonaceous particles to state ice nucleating features of INPs.

3. Methods

3.1 Cryo-Microscopy

The INA was determined by an immersion freezing technique, which was used in recent publications, for example, by Hauptmann et al. (2016), Pummer et al. (2012) and Zolles et al. (2015). It is a lab bench droplet freezing technique capable of generating and observing the freezing process of droplets in the micrometer size range present in an emulsion. In the course of this work major improvements have been implemented to this technique (see Chapter 4).

To generate droplets in micrometer size, an aqueous suspension containing the INP of interest gets mixed with an oil phase consisting of 80wt% paraffin oil and 20wt% lanolin and shaken with a laboratory shaking device. The mixing process was continued until the emulsion turned opaque, indicating that Mie scattering sets in and therefore droplet sizes in micrometer range were generated. The oil phase was always added in small excess. This process generates aqueous droplets embedded in an oil phase that can be used for freezing measurements in the same way as the freezing chip (Pummer et al., 2012; Zolles et al., 2015; Hauptmann et al., 2016). The emulsion becomes transferred on a sample carrier which is placed directly on a thermoelectric cooler (TEC) located in a cryo-cell. The TEC is capable to cool down the emulsion to -40 °C where homogeneous freezing of droplets with this volume takes place. A camera connected to the light microscope records the freezing process. The freezing point is indicated by contrast changes of the droplets due to different light scattering properties of liquid and frozen water. By evaluating the recorded freezing process, so-called freezing spectra showing the amount of frozen droplets f_{ice} at a given temperature T are obtained (see Figure 3-1). Due to the freezing temperature of ultrapure water at -36 °C, freezing events below -36 °C are considered as homogeneous freezing.

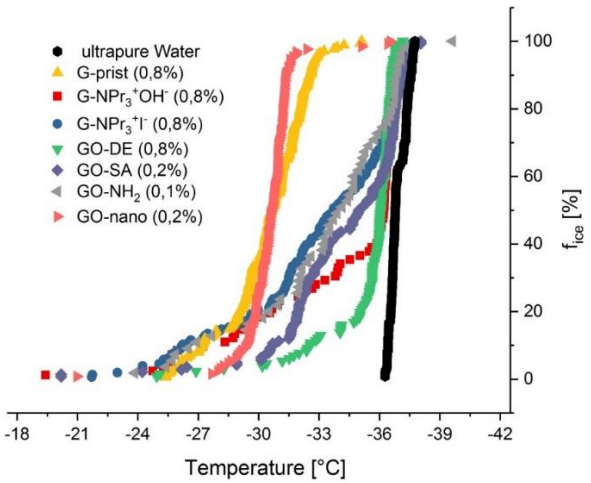

Figure 3-1 Representative freezing spectra of different kinds of graphene, graphene oxides and ultrapure water.

3.2 Infrared (IR) Spectroscopy

A molecule can be understood as a system of masses joined by bonds with spring-like properties (Colthup et al., 1990). The laws of quantum mechanics establish defined states or levels of vibration, rotation and translation of this spring, also called oscillator. The spring can jump between different levels by uptake or release of energy. This can be realized by interaction (absorption, emission or scattering) of the spring's molecule with photons. Depending on the characteristics of a molecule, a certain energy level scheme can be calculated. The energy differences in vibrational states of molecular bonds, match the energy of infrared photons. Hence, these systems can adsorb or emit energy from infrared radiation. The interactions of infrared radiation with matter may be understood in terms of changes in molecular dipoles associated with vibrations and rotations. In IR spectroscopy, the sample is exposed to a spectrum of IR light. The photon will be absorbed by a molecule, if the bonds between the atoms allow these atoms to vibrate in this frequency. The determination of what fraction of the incident radiation is absorbed, corresponds to the frequency of the vibration of the sample's molecule and gives information about the chemical structure. To absorb IR radiation, the electric dipole moment of the molecule must change during the vibration.

For Attenuated Total Reflection (ATR) IR spectroscopy, an internal reflection element (IRE), which is a transparent optical element with a high refractive index is in contact with an optically thinner medium, the sample. Due to the optical properties of the IRE, an evanescent wave results at the interface. An evanescent wave is a wave that does not propagate in a certain material, but whose energy is spatially concentrated underneath the penetration surface. The IR light is directed through the ATR crystal in such a way, that it reflects at least once off the internal surface in contact with the sample. In contrast to transmission IR techniques or other reflection techniques as Diffuse Reflection (DRIFTs) IR spectroscopy, samples investigated by ATR-IR can be solid and liquid and don't need to be diluted in an IR transparent matrix.

Functional groups on the surface of INPs are suggested to have a major impact on the INA (see Chapter 1.4). Hence, IR spectroscopy was used to determine the chemical functionality of INPs.

Each sample was placed directly on the ATR-crystal until it was fully covered. To increase the interface between crystal and sample, slight pressure was applied on the sample via a pressure stamp. The Vector 22 spectrometer from Bruker, equipped with a DTGS (deuteriated triglycine sulphate) detector and Harrick (Split Pea^{TM} ATR microsampler) ATR chamber, was

used. The ATR unit contained a germanium crystal as total reflection window. For each measurement, 512 scans with a resolution of 4 cm^{-1} were performed.

3.3 Raman Spectroscopy

Raman spectroscopy is based on the sample's interaction with monochromatic light, usually from a laser in visible range (Colthup et al., 1990). Thereby, laser photons are scattered on the sample's molecules in two different ways: (i) elastic, where neither the photons, nor the molecule's oscillators (see Chapter 3.2) change their energy and (ii) inelastic, where the molecule's oscillators are excited to a higher (or relaxed to a lower) virtual energy level for a short time, before the photon is emitted. During inelastic scattering the energy of the emitted photon becomes of lower or higher energy than the incident photon and the sample changes it's rotational or vibrational state. The shift in energy gives information about the vibrational modes in the system. The energy difference of elastically and inelastically scattered light can be expressed as absorption energy. For a molecule to be Raman active and exhibit inelastic scattering, there must be a change in its polarizability. The intensity of the Raman scattering is proportional to this polarizability change. Samples as e.g. soot or graphene can heat up if they have an absorption band at the excitation wavelength range of the laser. This can be prevented by applying short excitation periods. Furthermore, fluorescence emissions during the measurement of organic samples can occur but can be prevented by the usage of near-infrared laser.

For highly disordered materials such as e.g. soot, Raman spectroscopy is commonly applied to investigate structural characterizations, because it is sensitive to crystal structures (long-range order) and to molecular structures (short-range order) (Sadezky et al., 2005; Ferrari and Basko, 2013; Liu et al., 2013; Hu et al., 2015; Smith et al., 2016). The Raman signals of graphite crystals result from lattice vibrations and are sensitive to the degree of structural disorder. The Raman spectra of a near-ideal graphitic lattice of highly oriented polycrystalline graphite (HOPG), differs significantly from the Raman spectra of disturbed graphitic lattices of polycrystalline graphite. Hence, several studies investigated the characteristic lattice differences of divergent types of soot using Raman spectroscopy (Mernagh et al., 1984; Gruber et al., 1994; Dippel and Heintzenberg, 1999).

The spectrum of a sample with undisturbed graphitic lattice exhibits only one first-order band, the G (''Graphite'') band at around 1580 cm^{-1}, which corresponds to an ideal graphitic lattice vibration mode with E_{2g} symmetry. The spectrum of a graphitic bar with a disturbed graphitic lattice additionally exhibits characteristic first-order bands (D or ''Defect'' bands). They grow

in intensity relative to the G band with increasing degree of disorder in the graphitic structure. Four different kinds of disorder bands (surfaces, edges, amorphousness and impurities/polyenes) can be distinguished as D1 to D4. The origin and characteristic of each D-band is listed in Table 3-1. By applying and fitting potential vibration bands to the measured Raman spectra (see Figure 3-2), a qualitative and quantitative statement of the graphene lattice and their disorders can be made. The appearance of individual vibration bands provides a qualitative statement, while the bands proportional intensity provides information on the contribution of each vibration. The bands intensities are expressed as a percentage fraction of the total intensity.

Curve fitting for the determination of spectral parameters was performed with the software OriginPro 9.1G, using the least-squares method. The goodness-of-fit was indicated by the reduced χ^2 value, which indicates the agreement between the calculated fit curve and the observed spectrum. Detailed information about the fitting is given in Sadezky et al. (2005).

Table 3-1 First-order Raman bands and vibrational modes of soot and graphite according to Sadezky et al. (2005) for interpretation of the obtained Raman spectra (vs=very strong, s=strong, m=medium, w=weak). Minor changes in the Raman shifts may occur due to the different measurement parameters.

Band	Raman shift [cm^{-1}]		Vibration mode[a]
	Soot	Disordered graphite[b]	
G	~1580, s	~1580, s	Ideal graphitic lattice (E_{2g}-symmetry)
D1	~1350, vs	~1350, m	Disordered graphitic lattice (graphene layer edges, A_{1g} symmetry)
D2	~1620, s	~1620, w	Disordered graphitic lattice (surface graphene layers, E_{2g} symmetry)
D3	~1500, m		Amorphous carbon (Gaussian line shaped)
D4	~1200, w		Disordered graphitic lattice (A_{1g} symmetry), polyenes, ionic impurities

[a] Lorentzian line shaped unless otherwise mentioned

[b] Polycrystalline graphite (<100 nm) and boron-doped highly oriented polycrystalline graphite (HOPG)

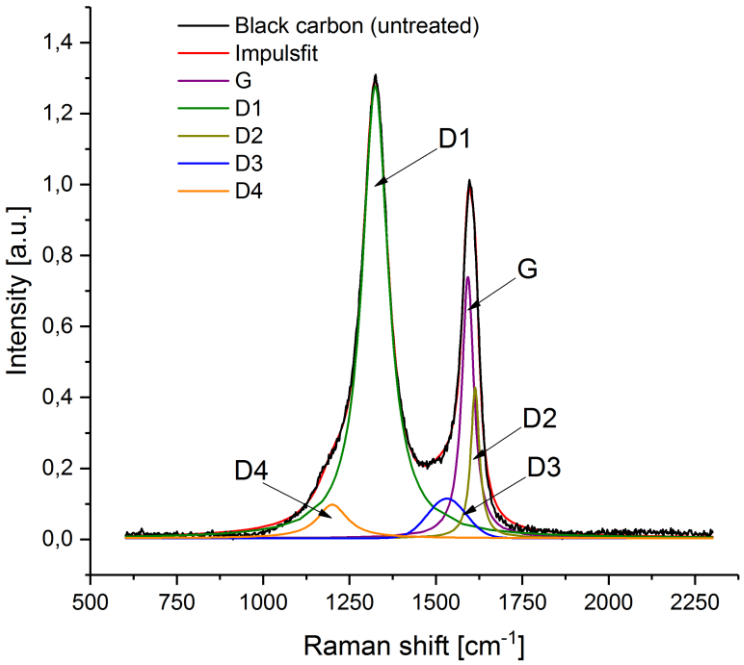

Figure 3-2 Representative Raman spectra of untreated black carbon, first-order curve fitted with band combination according to Sadezky et al. (2005) (see Table 3-1).

The microstructure and lattice structure of INPs are thought to have an impact on the INA (see Chapter 1.4). Knauer et al. (2009) applied Raman spectroscopy to show the link between the reactivity of soot during oxidation and its microstructure. Furthermore, the work of Lupi and Molinero (2014) indicated that the microstructure of carbon particles play an important role in the heterogeneous ice nucleation mechanism. Therefore, Raman spectroscopy was used to determine the lattice characteristics of INPs.

Each sample was applied and distributed on a sample carrier until a covered area of about 0.5 cm^2 was achieved. The Raman microscope system (Jobin Yvon, LabRAM HR) consisted of a light microscope (Olympus BX) coupled to a Raman spectrometer. A twentyfold objective and a grating with 300 gr/mm were used. Furthermore 60 scans with an exposure of each 5 seconds were collected to get a sufficient signal-to-noise ratio using a laser with a wavelength of 633 nm and a source power of 25 mW. The interpretation and evaluation of the Raman spectra was done according to Sadezky et al. (2005).

3.4 Nitrogen Adsorption

Nitrogen adsorption techniques are used to determine the surface area of porous solids. Liquid nitrogen cools down the sample to about -200 °C and determines the adsorbed amount of gaseous nitrogen under increased pressure. The following reduction of pressure releases (desorption) the adsorbed gas from the surface. An adsorption-desorption-isotherm enables the calculation of the surface area. The applied adsorptions isotherm by Brunauer, Emmett and Teller is a further development of the Langmuir isotherm (Brunauer et al., 1938) and commonly applied.

The so-called ice nucleation active surface site density n_s (see Chapter 1.3.2) is repeatedly used in this work to describe heterogenous ice nucleation. For this, the surface values of INPs were determined using a nitrogen adsorption technique.

The surface areas of the samples were measured using a commercial liquid nitrogen adsorption system (ASAP2020, Micromeritics). About 1.2 g of a sample was heated under vacuum (<13 µbar) at 150 °C for 2 hours before the nitrogen adsorption at -196 °C.

3.5 X-Ray Photoelectron Spectroscopy (XPS)

When a X-ray photon collides and transfer its energy to a core-level electron, the electron is emitted from its initial state (Watts and Wolstenholme, 2003). The kinetic energy of the electron depends on the incident X-Ray light and binding state of the originating atom. The determined energy and intensity of the photoelectron are evaluated to identify the elemental composition qualitatively and quantitively. This method is surface sensitive, since the penetration depths (depending on the elemental composition) lies below 10 nm.

The chemical composition and functionality of INPs are suggested to have a major impact on the INA (see Chapter 1.4). Hence, XPS spectroscopy was used to determine the chemical composition of INPs.

X-ray photoelectron spectroscopy (XPS) was carried out using facilities of the Analytical Instrumentation Center AIC at the TU Wien.

Measurements were performed with a SPECS XPS spectrometer equipped with an Al Kα- X-Ray source (µFocus 350) and a hemispherical WAL-150 analyzer (acceptance angle 60°). The samples were fixed with molybdenum clamps on the sample carrier. To reduce loading effects, the samples were occasionally transferred on a copper carrier. The excitation energy was set to 1486.6 eV, the Pass energy to 30 eV and the resolution to 50 meV. The lower detection limit of quantification is 0.1 at% with an accuracy of 10- 20% depending on the

element. For preparation the samples were drop coated on a silicon single crystal. For the evaluation the software package CASA XPS with transmission correction, Shirley-background (Shirley, 1972) and sensitivity parameter according to Scofield (1976) were used. Charging corrections were done to keep the C-C signal in the C 1s signal steady at 284.8 eV bond energy. All resulting elemental composition are presented in atom percent (at%). The limit for quantification lies at about 0.1 at%. The accuracy of the quantification lies depending on the element at about 10% of the given value. The classification of each component is done according to *NIST Standard Reference Database 20* (Wagner et al., 2003) and *The Scienta ESCA300 Database* (Beamson and Briggs, 1992). The C 1s signal was fitted using a combination of Gaussian/Lorentzian- signals and Shirly-background with the software UNIFIT.

3.6 Transmission Electron Microscopy (TEM)

The transmission electron microscope uses electrons emitted from an emission source connected to a high voltage (Williams and Carter, 1996). These electrons are focused by electromagnetic lenses into a thin beam. The electron beam travels through vacuum until it reaches the sample and depending on the characteristics of the sample, penetrates the sample or is scattered. The remaining electrons hit a fluorescence screen at the bottom of the microscope, resulting to an image displayed in varied darkness's, according to the amount of scattered/unscattered electrons. In general, the TEM operated on the same principle as the light microscope but is capable to reach higher resolutions due to the decreased wavelength of accelerated electrons.

The microstructure of INPs is thought to have an impact on the INA (see Chapter 1.4). The microstructure of soot can include graphene nanoribbons, whose curvature has been identified as a crucial parameter defining the reactivity of soot (Müller et al., 2007). Therefore, TEM analysis has been applied to identify the morphology and microstructure of INPs.

TEM images were obtained on a FEI Tecnai F20 with an acceleration voltage of 200 kV. Samples were prepared by first dispersing them ultrasonically in ethanol and, subsequently, dropping the ethanolic solution on Lacey(R)-coated copper grids. For each sample, overview images to investigate particle size and distribution as well as close-up images to investigate morphology and structure were recorded. Particles sizes were estimated as there was no clear distinction between different particles. Several samples showed some charging effect, which made it difficult to obtain highly resolved images in some cases.

4. Freezing on a Chip- a New Approach to Determine Heterogeneous Ice Nucleation of Micrometer-Sized Water Droplets

Portions of this chapter have been published as *Freezing on a Chip–A New Approach to Determine Heterogeneous Ice Nucleation of Micrometer-Sized Water Droplets* by the Journal *Atmosphere* and partially reproduced (Häusler et al., 2018b).

As described above (see Chapter 1.5.1), the commonly vial-shaking lab bench technique reveals several obstacles. Further developments are needed to improve the investigation of droplets with diameters down to 20 µm in a wide temperature window down to -37 °C. A new approach to analyze the freezing behavior of aqueous droplets containing ice nucleating particles (INPs), with droplet diameters in micrometer range is presented here. Disadvantages of conventional oil-emulsion droplet-freezing experiments like varying droplet sizes or interactions between the water-oil mixture and the INP, were overcome. The freezing-chip consists of an etched and sputtered 15x15x1 mm gold- plated silicon or pure gold chip.

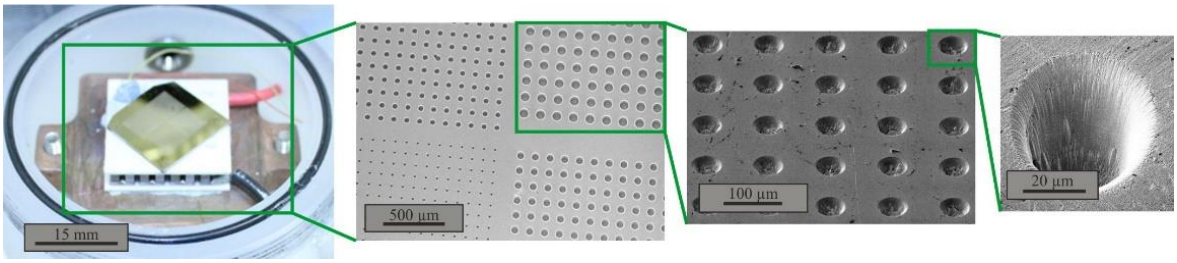

Figure 4-1 Freezing on a Chip- graphical abstract.

Several applications like an automated process control and an automated image evaluation were implemented to improve the quality of heterogeneous freezing experiments. To show the functionality of the setup, a comparison of freezing temperatures of ultrapure water and different INPs (microcline, birch pollen washing water, juniper pollen, Snomax® solution) measured with our setup, with literature data is shown. Minor deviations of the ice nucleation active surface/mass site density $n_{s/m}$ of microcline, birch pollen washing water and juniper pollen compared to literature data are shown and can be explained by slight differences in composition and droplet generation technique. n_m differences close to one order of magnitude at warmer temperatures of Snomax® are suggested to originate from advanced decomposition.

4.1 Description of the New Setup

The experimental setup consists of four main parts: (i) the light microscope including a HD camera to observe the freezing experiment, (ii) the freezing-cell to cool down the sample, (iii) the freezing-chip carrying an ensemble of droplets, and (iv) a computer to control the cell temperature and cooling rate, as well as to record and evaluate pictures of the freezing droplets.

The novel freezing-chip was designed from a (15 × 15 × 1) mm silicon plate by etching a pattern of cavities which allows for the creation of isolated droplets with diameters between 20–80 µm. Reactive ion etching (RIE) was carried out with an OXFORD Plasmalab 80 with 10 cm^3/min argon and 20 cm^3/min SF_6 used as etching gas. The pattern consists of cavities with defined diameters at defined distances from each other, shown in Figure 4-2.

Experiments with ultrapure water revealed a shift of the freezing temperature from −37.5 °C to approximately −20 °C, once the cavity pattern was etched onto the silicon chip. Neither silicon itself nor the roughness of the silicon surface are expected to show INA. Peckhaus et al. (2016) found no effect of a smooth silicon substrate on the freezing temperature between −36 °C and −3 °C of spherical droplets with diameters of 107 ± 14 µm. Campbell et al. (2015) showed that neither form of surface roughening of silicon has any effect on the freezing temperature of ultrapure water. Silicon, as well as glass and mica substrates roughened with diamond powders, resulted in freezing temperatures close to the expected homogeneous freezing temperature. Therefore, the observed shift to −20 °C after the etching process seems to be caused by the reaction of the etching agents with the silicon surface, leading to an ice nucleation active compound. For this reason, a gold layer (with a thickness of 500 nm) was sputtered on top of the pattern after the etching process, creating an ice nucleation neutral surface. As an alternative to a gold sputtered silicon plate, a pure gold chip of similar dimensions was ion-milled with a focused ion beam (FIB) to introduce the same kind of pattern. Due to the thermodynamic stability of pure gold, no ice nucleation active compounds were formed on the surface during the introduction of the cavity pattern, and no further treatments of the surface were necessary. If the surface of the gold sputtered silicon plate is damaged and the silicon is exposed, the chip becomes ice nucleation active again. Small scratches on the surface, as well as slight surface irregularities in the cavities, were not found to have any influences on the INA, which is in agreement with Campbell et al. (2015). Nevertheless, scratches must be avoided to not damage the cavity pattern.

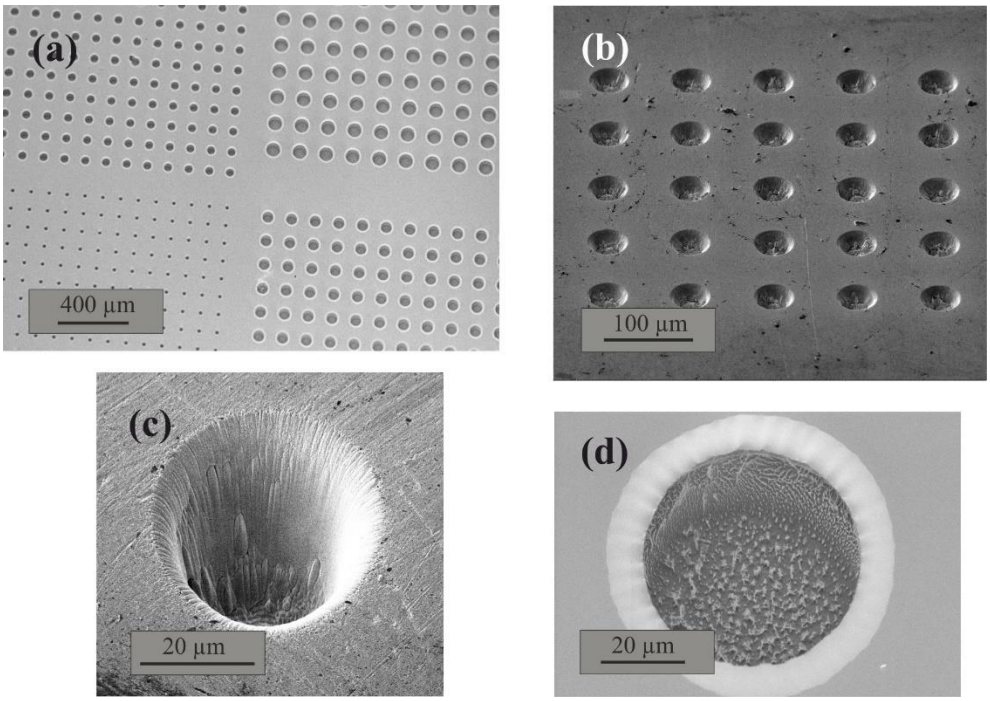

Figure 4-2. Different electron micrographs of the freezing-chip. (a) Cavities of different size (ca. 20 µm to 80 µm) arranged on the freezing-chip. (b) A more detailed picture of the arrangement of the ca. 40 µm cavities. (c) A 40 µm cavity sputtered in gold by ion milling and (d) a 40 µm cavity etched in the gold plate via Ar-SF_6 plasma.

The light microscope is equipped with a 20-fold LWD (long working distance) objective and a 5.0-megapixel USB 3.0 camera (microQ L3CMOS) which is connected to the computer. The custom-built freezing cell is embedded in a hollow polytetrafluorethylene (PTFE, Teflon®) cylinder with a diameter of 68 mm and a height of 25 mm, which can be sealed hermetically (Figure 4-3).

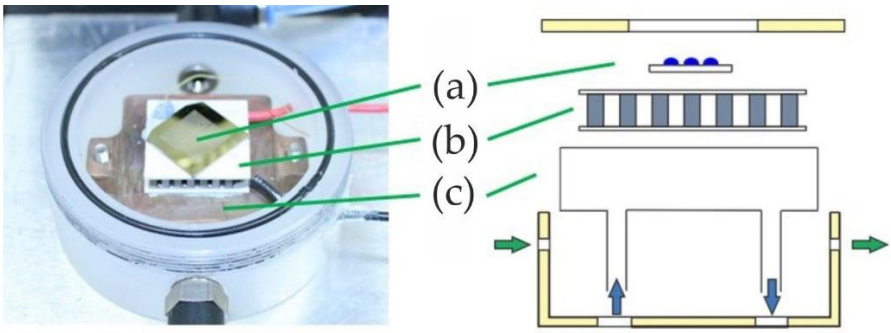

*Figure 4-3. Photograph (left) and vertical section scheme (right) of the freezing cell. The freezing chip (a) lies directly on the thermoelectric cooler (TEC) (b), which is fixed to the heat exchange device (**c**) via a conductive adhesive. The cell can be flushed with dry nitrogen (symbolized by the green arrows) to remove humidity, which could interfere with the measurements. The blue arrows trace the flow of cooling water, taken from a water-ice mixture to cool the warm side of the TEC. The electronic connections (black and red wire) of the TEC are visible in the picture on the left.*

Controlled cooling is performed by a thermoelectric cooler (TEC; i.e., a Peltier element Quick-cool QC-31-1.4-3.7M), connected to a computer-controlled power supply. A water-ice mixture (of approximately 5 °C) is pumped out of a storage tank into a heat exchanger attached to the warm side of the Peltier element with a water pump (EHEIM universal pump). With this set-up, we are able to cool our samples down to −40 °C and below by regulating the electrical current through the TEC. A K-type thermocouple with an associated uncertainty of ±0.4 °C is attached directly on the cold side of the TEC with a thermally conductive adhesive to monitor the temperature. The thermocouple is connected to the computer via a thermocouple measurement device (NI USB- TC01). Two gas connectors on the shell of the freezing cell allow flushing with dry nitrogen. This is done before every experiment to remove humidity and establish a moisture-free atmosphere. Additional slots are available in the shell to insert the thermocouple and the electric connectors for the TEC. The top cover of the cell is removable to introduce the sample and includes a glass window which enables observation of the sample via light microscopy. The cell is placed on a stage directly underneath the objective of the light microscope.

Once the chip is loaded with droplets, it is directly placed on the TEC inside the freezing cell. The field of view, specified by the parameters of the light microscope, enables the observation of about 25 droplets with a center-to-center distance of 100 µm for each experiment. The freezing process can be monitored on the computer screen and is automatically recorded and saved as a video file. Videos are evaluated automatically by a LabVIEW VI (virtual instrument). During the freezing process the droplets turn dark because ice shows a different light scattering behavior than liquid water (see Figure 4-4). The first step for evaluating the videos is to manually mark each droplet (see Figure 4-5). Afterwards, the software analyzes the video and determines the time when the droplet turns dark (i.e., freezes). A contrast graph is generated for each droplet, linking the brightness of the droplet to the time, with respect to temperature. This enables the freezing process to be followed.

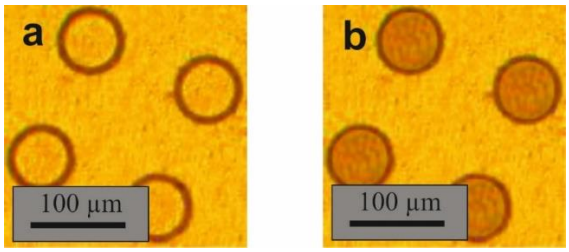

Figure 4-4 Digitally reworked illustration of the differences in light scattering behavior of (a) water and (b) ice as observed via light microscope, leading to a contrast increase during the freezing process which is used to determine the freezing temperature.

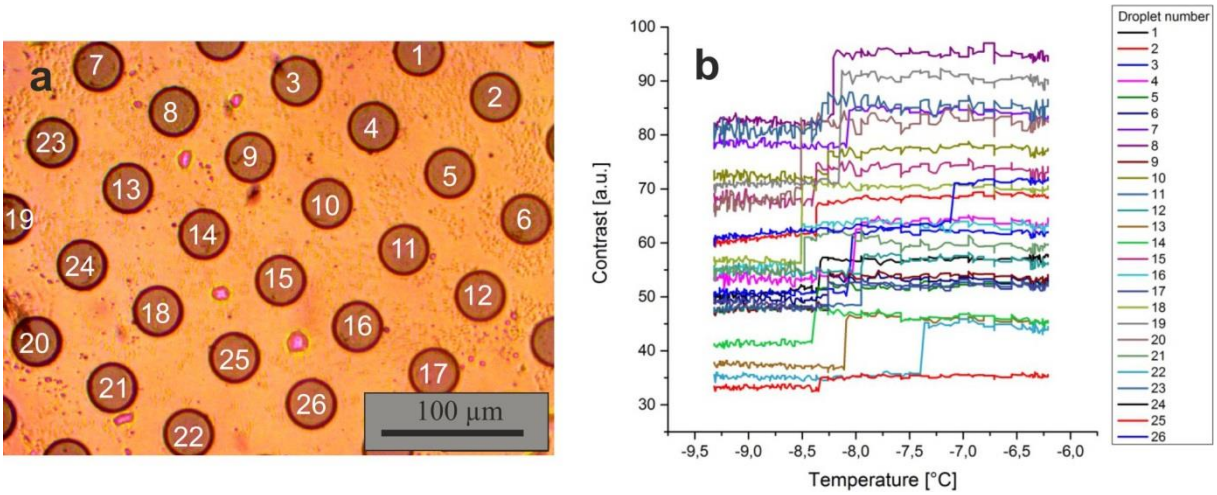

Figure 4-5 Screenshot of the freezing chip (a) as observed during a freezing experiment and the corresponding contrast trend (b) evaluated automatically using LabVIEW, of each frozen droplet.

The accuracy of the temperature measurements was determined by measuring the melting points of five different solvents with well-known melting points. The calibration using melting points (under thermodynamic control) rather than freezing points (under kinetic control) is essential due to the underlying nucleation of crystallization (Riechers et al., 2013). The melting temperature range was determined visually. A maximum temperature error of ±0.4 °C was found. The results of the measurements are presented in Table 4-1. No temperature gradients within the cold stage were observed when using multiple temperature measuring points simultaneously.

Table 4-1 Melting temperature (T_{mp}) of solvents used for temperature calibration. Seven measurements were performed for each solvent.

Chemical	Literature T_{mp}* [°C]	Recorded T_{mp} and standard deviation [°C]	Start [°C]	Finish [°C]	Range [°C]
Ultrapure water	0.0	−0.2 ± 0.1	-0.1	-0.3	0.2
n-Dodecane	−9.6	−10.0 ± 0.1	−10.3	−9.7	0.6
1-Octanol	−14.8	−14.6 ± 0.2	−15.0	−14.2	0.8
Undecane	−25.5	−25.2 ± 0.1	−25.6	−24.8	0.8
Nitromethane	−29.0	−28.9 ± 0.3	−29.3	−28.5	0.8

* Literature melting temperatures taken from *CRC Handbook of Chemistry and Physics* (Haynes, 2004).

4.2 Materials and Preparation

Four different aerosol types were used to investigate the efficiency of the setup: microcline, birch pollen washing water, juniper pollen, and a Snomax solution. The freezing experiments were carried out in ultrapure water type 1 generated by the MilliQ water purification system, Merck Simplicity® 2012. For each set of experiments, the water was directly taken from the generator and stored in a laboratory glass bottle for a maximum time of about 6 hours. The temperature control was set to a cooling rate of 2 K/min for all measurements.

- Microcline is a naturally occurring mineral and was supplied by Alfa Aesar GmbH & Co KG. The composition was determined via X-ray diffraction phase analysis (77% K-feldspar (microcline), 23% Na/Ca-feldspar (albite)). The mineral was freshly milled with a swing mill (Retsch MM400) for 4 minutes and at 30 swings per second immediately before the experiments. A mean surface area of 6.6 m^2/g was determined using the physical adsorption of gas molecules on solid particles (BET Brunauer-Emmett-Teller technique). Microcline was suspended in ultrapure water (in a concentration of 20 g/L).
- The birch pollen sample originated from the Czech Republic and was obtained from Pharmallerga®. The preparation was carried out as described by Augustin et al. (2013). One gram of birch pollen was suspended in 20 mL ultrapure water and placed for 12 hours in a refrigerator. Afterwards, the suspension was filtered (Macherey-Nagel 640m), and the pollen washing water was diluted 1:2 with ultrapure water.
- Juniper pollen was obtained from Pharmallerga® (Juniperus communis JUNU.0111). Sixty-four milligrams of juniper pollen were suspended in ultrapure water at a concentration of 50 mg/mL. After 20 hours at room temperature, the suspension was directly used for the freezing experiment.
- Snomax was obtained from SMI Snow Makers AG. It consists of shredded *Pseudomonas syringae*, an ice nucleation active bacterium. It was stored at −20 °C for 3 years before the measurements were performed. About 1 mg of Snomax was suspended in ultrapure water to a concentration of 0.5 mg/mL.

The freezing behavior of all these INPs is well described in literature, rendering those substances of suitable standard to test the new setup. Their freezing temperatures cover a broad range between −7 °C (Snomax, stored for ≥14 months in a freezer (Polen et al., 2016)) and the predicted homogeneous freezing temperature of water at −37 °C (Pruppacher and Klett, 1997).

Preparation of the Freezing-Chip

For the sample preparation, we applied a thin film of the suspension on the freezing-chip. By placing 2 µL of the sample (i.e., the INPs suspended in ultrapure water) with a pipette on the chip and reabsorbing the suspension into the pipette, a thin film of suspension is applied on the freezing-chip. By precooling the chip to approximately 5 °C right before applying the suspension, the liquid between the cavities evaporates while the cavities stay filled. This leads to droplets in the size of the etched cavities, with defined radii and defined distances between the droplets given by the etched pattern. Different droplet sizes can be achieved with different cavity sizes.

Once the cavities are filled, the surface is coated with paraffin oil to prevent the Wegener–Bergeron–Findeisen effect, which occurs when water is present in both liquid and solid phases. This effect would lead to continuous condensation of water vapor on ice while, at the same time, liquid water evaporates until the liquid phase is entirely consumed (Wegener, 1911; Korolev, 2007). A small droplet of paraffin oil is placed at the center of the plate and spread by putting a microscope plate on top. Using this method, a thin and evenly distributed oil film on top of our chip is obtained. Leading to evenly separated and isolated droplets (Figure 4-6).

The chip was cleaned after each measurement by being immersed in acetone/isopropanol (50/50), toluene, and ultrapure water for 20 minutes each. In certain cases (e.g. Snomax), preheating treatment (150 °C for 1 hour) is required to obtain a complete removal of INPs.

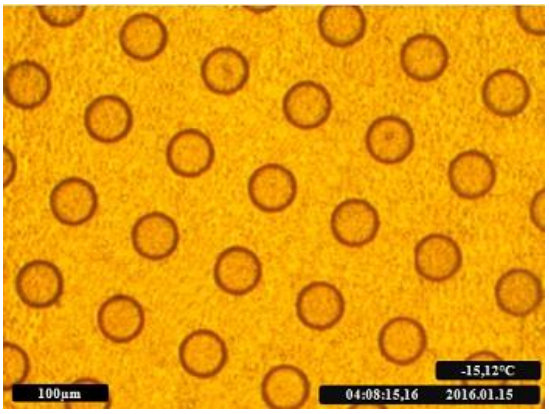

Figure 4-6 Screenshot of the freezing-chip from a recorded freezing video. Cavities (d = 40 µm) are filled with liquid ultrapure water and covered with oil. Temperature, date, and time is automatically inserted.

4.3 Results and Discussion

Homogeneous ice nucleation depends on the droplet volume (Vali, 1971). By increasing the volume, the chance of forming a critical ice cluster via fluctuation of intermolecular hydrogen bonds is higher. Heterogeneous ice nucleation is dependent on the amount of active surface area at the interface between the INP and water (Murray et al., 2011) and has no volume dependence (Hartmann et al., 2016). The characteristic parameter to describe the ice nucleation activity of INPs is the so-called ice nucleation active surface site density n_s (see Equation (9)). The ice nucleating activity can be also expressed by referring to the number of active sites per mass of ice nucleating material (n_m) instead of the surface area per droplet. This is often used when the surface of the investigated INP cannot be accurately quantified.

By increasing the size of droplets from cloud droplet size (diameters of about 10 µm) to about 40 µm, the surface area per droplet for a constant mass fraction of INP in water is increased. Accordingly to Equation (9), this allows the quantification of n_s to smaller values and determination of nucleation efficiencies over a wider range of temperatures than is possible using cloud-sized droplets.(Whale et al., 2015a)

To investigate the comparability of ice nucleation results obtained with the new setup using other experimental techniques, the freezing behavior of the different kinds of INPs was analyzed and compared with the existing literature. For each experiment, 10 measurements were performed. Values of T_{50}, $n_{s,}$ and n_m were used to describe the freezing behavior. T_{50} values describe the temperature at which f_{ice} reaches a value of 50, i.e., 50% of the observed droplets are frozen (see Equation (9)).

4.3.1 Freezing Spectra and T_{50} Values

The chosen aerosol types and ultrapure water were selected to cover a broad freezing temperature range between −7 °C (Snomax, stored for ≥14 months in a freezer (Polen et al., 2016)) and the predicted homogeneous freezing temperature of water at −37 °C (Pruppacher and Klett, 1997). Figure 4-7 shows the freezing spectra of each investigated INP and ultrapure water. They reveal a T_{50} value for microcline of –16.4 °C, birch pollen washing water of −18 °C, juniper pollen of −22.7 °C, Snomax of −8.9 °C, and ultrapure water at −37.5 °C. Ultrapure water, birch pollen washing water, and Snomax freeze within a narrow temperature range of 1 to 2 °C between the first and the last freezing event, while juniper pollen and microcline show a wider freezing range of 8–11 °C.

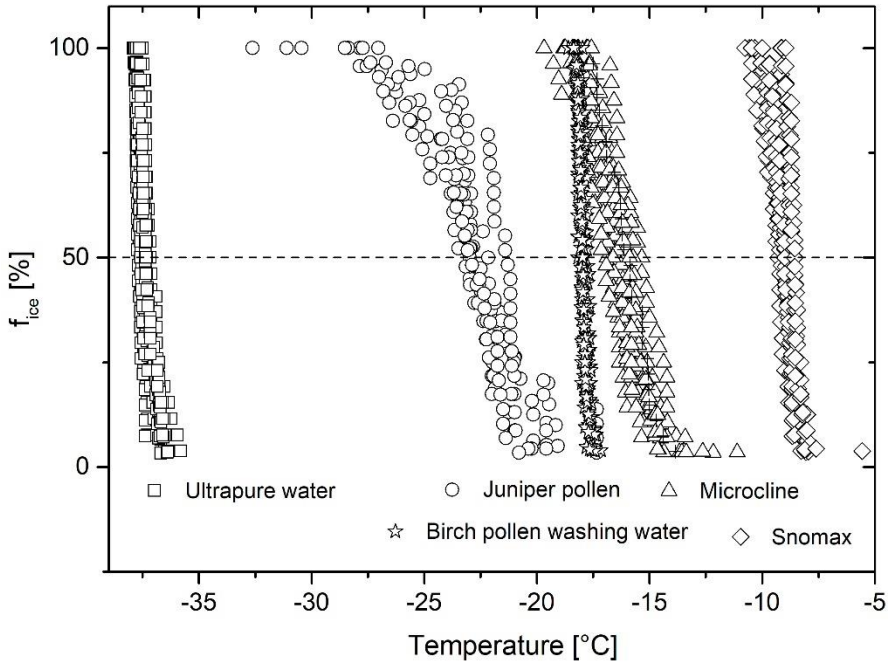

Figure 4-7 Ice nucleation spectra obtained in freezing experiments using freezing-chips with different INPs: microcline, birch pollen washing water, juniper pollen, Snomax, and ultrapure water. The dashed line marks the T_{50} values.

The homogeneous freezing temperature of water is given by Pruppacher and Klett (1997) for droplets with a diameter of 40 µm as −37 °C. Measurements performed with the freezing-chip resulted in an average T_{50} value of –37.5 °C. Considering a temperature error of ±0.4 °C, the determined homogeneous freezing temperature is in good agreement.

The reproducibility of freezing experiments indicates that the INPs are evenly distributed in the droplets and no concentration varieties take place.

4.3.2 Ice Nucleation Active Surface/Mass Site Densities

a. Microcline

The n_s trend of microcline shown in Figure 4-8 is in good agreement with data obtained by Peckhaus et al. (2016). Partial shifts to higher n_s values between −14 °C and −15.5 °C can be seen for freezing-chip-obtained values. Freezing events at temperatures below −12 °C do not agree with Peckhaus et al. (2016). The deviations are considered to be within an acceptable error range based on the different measurement techniques used by Peckhaus et al. (2016) (Piezo-driven droplet-on-demand generator) and slight differences in the microcline composition. Furthermore, measurements using the vial-shaking technique were performed with the same batch of microcline as for the freezing chip measurements. Deviations at temperatures below −19 °C may occur due to the shaking process reducing the concentration of INP and INA. The data obtained via vial-shaking technique is considered to lie within an acceptable range and demonstrates the reproducibility of data using the freezing chip.

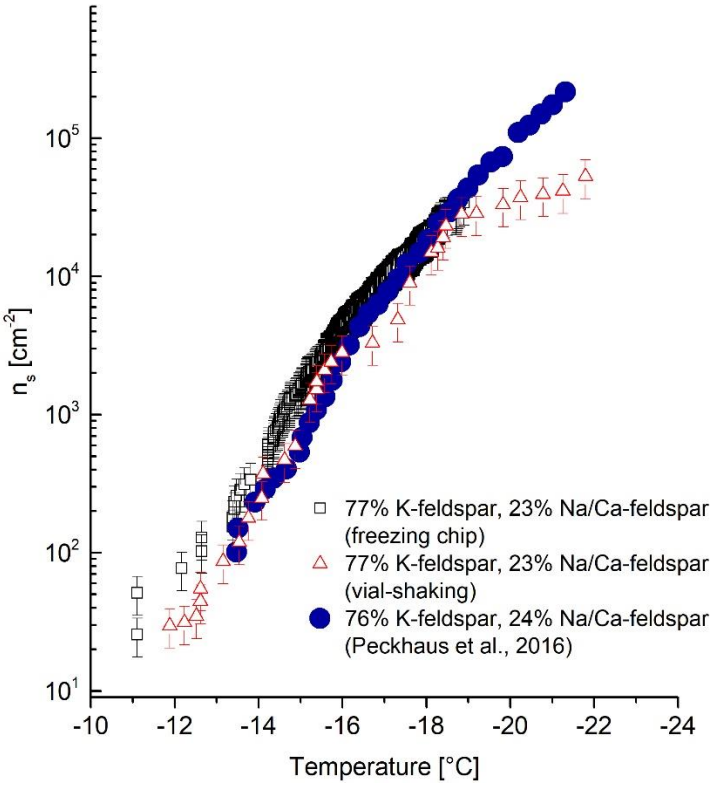

Figure 4-8 The ice nucleation active surface site densities (n_s) of microcline determined with the freezing chip compared to measurements performed with the vial-shaking technique and already published data (Peckhaus et al., 2016). The error bars of the n_s values originate from the estimation of the corresponding droplet diameter of 40 µm ± 10% and weighing uncertainties.

b. Birch Pollen Washing Water

The n_s trend of birch pollen washing water obtained with the freezing chip compared to data by Pummer et al. (2015) is shown in Figure 4-9. While the n_s trend found by Pummer et al. (2015) has a step between −17 and −18 °C and the gradient then decreases, a steeper trend has been found in the values obtained with the new method. Pummer et al. (2015) explained the characteristic decrease of the gradient between −17.5 and −18.5 °C by the fact that the INP is scarce or inefficient. Nevertheless, the differences in n_s trends might be accounted by the presence of two types of INPs present in birch pollen washing water. The more efficient one is concentration-dependent since it is reported to be an agglomeration product of smaller polysaccharides (Dreischmeier et al., 2017). The vial-shaking process to generate droplets in an oil matrix might reduce the concentration of INPs in the water slightly, leading to less agglomeration. This leads to a decrease of INA and decreased n_s values above −18 °C. Using the freezing chip, no INPs are expected to migrate into the oil cover, keeping the concentration and the INA unchanged. It appears that the n_s values from Pummer et al. (2015) are higher than those from the freezing chip at temperatures above −17.5 °C. This contradicts the assumption of decreased n_s values using a vial-shaking technique but might originate from the temperature error of ±0.4 °C. Minor deviations below −18 °C might originate from differences in measurement technique and/or the composition of the pollen batch.

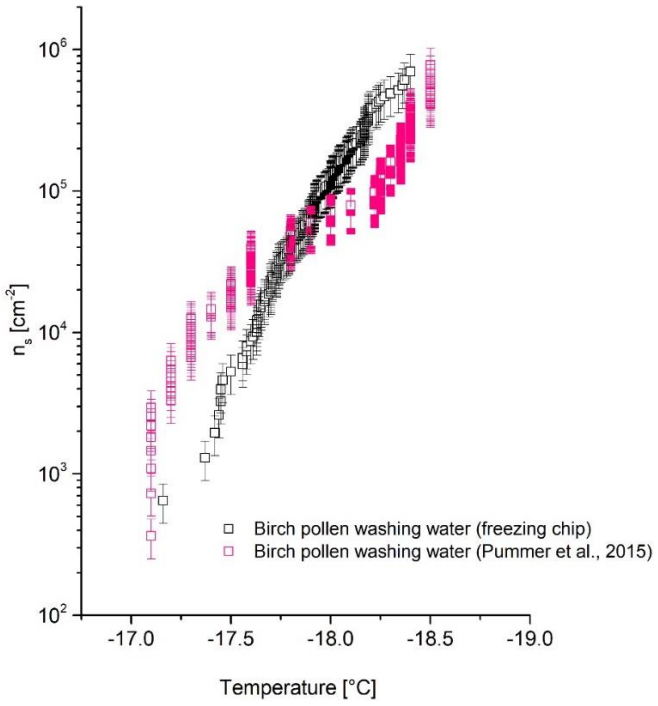

Figure 4-9 The n_s values of birch pollen washing water determined with the freezing chip method compared with already published data (Pummer et al., 2015). The error bars of the n_s values originate from the estimation of the corresponding droplet diameter of 40 µm ± 10% and weighing uncertainties.

c. Juniper Pollen

The n_s trend of juniper pollen shown in Figure 4-10 is in good agreement with Pummer et al. (2012). Partial shifts of freezing-chip-obtained n_s values are shown between −19 °C and −22 °C. The decreased values might be induced due to a different experimental set-up of Pummer et al. (2012) (vial-shaking technique) but are considered to lie within an acceptable range.

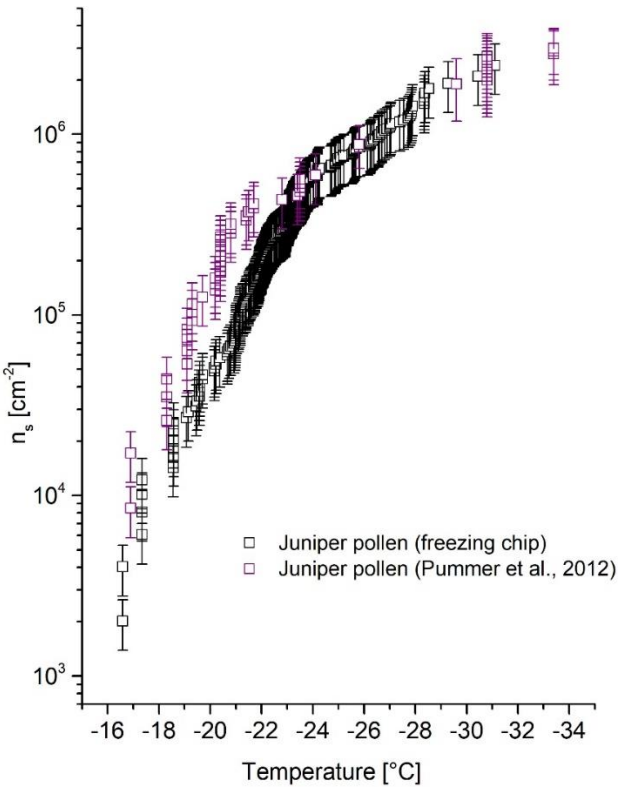

Figure 4-10 The n_s values of juniper pollen determined with the freezing chip and compared to already published data (Pummer et al., 2012). The error bars of the n_s values originate from the estimation of the corresponding droplet diameter of 40 µm ± 10% and weighing uncertainties.

d. Snomax

Figure 4-11 shows the obtained n_m values for Snomax using the freezing chip method, exhibiting a shift to decreased n_m values at temperatures above −8.5 °C compared to data published by Wex et al. (2015) and Polen et al. (2016). The shift to lower n_m values can be explained by the decomposition of Snomax with a prolonged period of storage (Polen et al., 2016). The more efficient ice nucleating protein of Snomax decomposes even when stored at temperatures below 0 °C, which results in a decrease of INA and decreased freezing temperatures of about −7 °C. At this temperature, a less active but more stable ice nucleus triggers ice formation. Ongoing storage duration and thus decomposition leads to a further decrease of n_m values at higher temperatures. Therefore, the decreased n_m values above −8.5 °C of Snomax which has been stored for three years are considered to be in agreement with published work of Polen et al. (2016) and Wex et al. (2015) who investigated Snomax samples stored up to 14 months. The usage of old Snomax samples as an evaluation standard appears more convenient than fresh samples, since it shows stable n_m values, especially at higher temperatures after a certain degree of decomposition (Polen et al., 2016). Furthermore, measurements using the vial-shaking technique were performed with the equally aged Snomax batch as for the freezing chip measurements. The data obtained via vial-shaking technique is in good agreement with the freezing chip. This agreement demonstrates the reproducibility of data using the freezing chip.

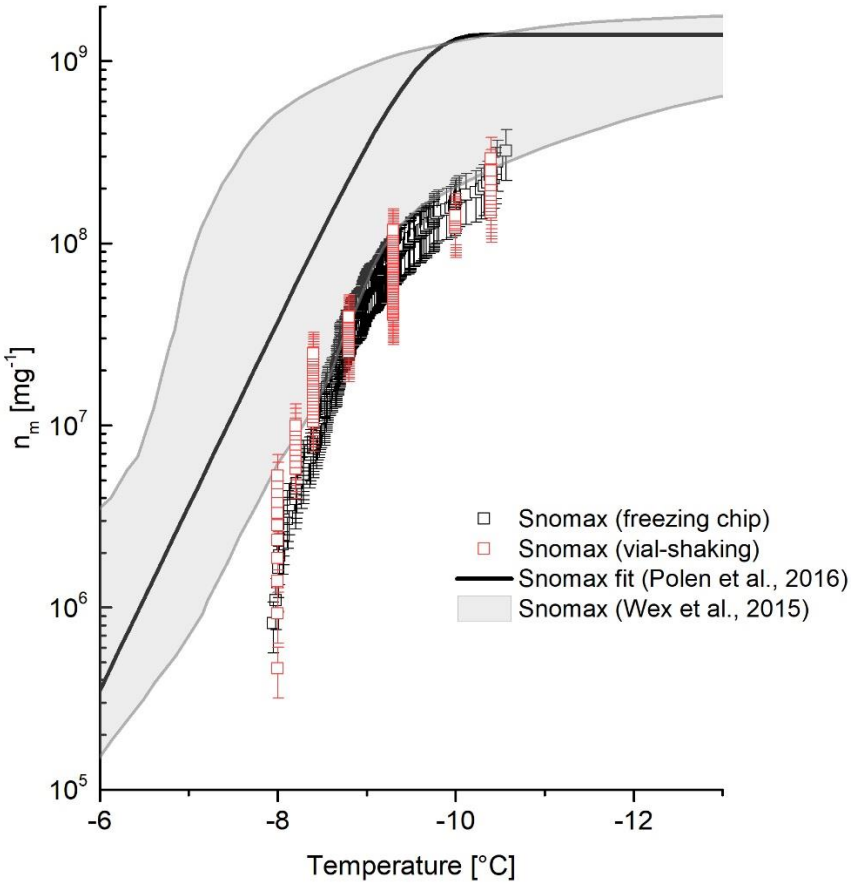

Figure 4-11 The n_m values of Snomax determined with the freezing chip compared to measurements performed with the vial-shaking technique and already published data (Wex et al., 2015; Polen et al., 2016). The error bars of the n_m values originate from the estimation of the corresponding droplet diameter of 40 µm ± 10% and weighing uncertainties.

4.4 Summary

A new technique to generate droplets with diameters in micrometer range was developed to investigate the INA of aerosol particles down to a temperature of −38 °C. By introducing a pattern of cavities on a gold or silicon chip by reactive ion etching and ion milling, the generation of up to 25 droplets with the same well-defined diameters was accomplished. Depending on the size of the cavities, droplets with diameters between 20 and 80 µm can be generated. Due to defined distances between the cavities, generated droplets do not come into direct contact with each other. Since no vial-shaking of an oil-water emulsion is necessary, the risk of migration of aerosol particles into the oil phase is reduced. Oil is only used as a cover to seal the cavities. Therefore, visual disturbances are decreased and the visual evaluation via light microscope is facilitated.

The recording of the freezing process on video files enables reruns and repeatable evaluations. The automatic evaluation via LabVIEW saves time and eliminates the problem of different results arising from varying personal interpretations of manually evaluated microscope pictures. The accuracy of the temperature measurements was determined by measuring the melting points of five different solvents with well-known melting points. A maximum temperature error of ±0.4 °C was determined.

To investigate the comparability of the new setup, the freezing behavior of four different aerosol types (microcline, birch pollen washing water, juniper pollen, and Snomax) and ultrapure water was analyzed and compared with the existing literature. The T_{50} value of ultrapure water droplets with 40 µm diameter of −37.5 °C matches the values published by Pruppacher and Klett (1997). The n_s values of microcline and juniper pollen are consistent with data published by Peckhaus et al. (2016) and Pummer et al. (2015). Minor deviations are suggested to originate from differences in measurement technique and/or composition of the microcline.

The n_s trend of birch pollen washing water revealed a steeper trend of values between −17 °C and −18 °C compared with Pummer et al. (2015). There are two nucleation sites present in birch pollen washing water and the more efficient one is concentration dependent since it is an agglomeration product (Dreischmeier et al., 2017). The vial-shaking process to generate droplets in an oil matrix reduces the concentration of INPs in the water slightly, leading to less agglomeration and to a resulting decrease of INA and n_s values above −18 °C. Using the freezing-chip, no INPs are expected to migrate into the oil cover. This keeps the concentration and, thus, the INA unchanged. However, minor deviations below −18 °C are suggested to originate from differences in measurement technique and/or composition of the pollen batch.

The n_m trend of Snomax shows a shift to lower values at temperatures below −8.5 °C compared to data published by Wex et al. (2015) and Polen et al. (2016). Previously studies showed the decomposition of the ice nucleating proteins of Snomax, leading to a decrease of n_m values at higher temperatures (Polen et al., 2016). Thus, it can explain the shift observed in our study. Therefore, the obtained n_m trend of Snomax is considered to be in agreement with published work of Polen et al. (2016) and Wex et al. (2015).

It can be summed up that the new technique reduces occurring issues in the vial-shaking droplet-freezing technique and is capable in reproducing published results. The freezing-chip retains the unique advantages of vial-shaking techniques but is additionally capable of eliminating and reducing certain disadvantages related to concentration and droplet size distribution.

5. The Ice Nucleation Activity of Graphene and Graphene Oxides

Portions of this chapter were previously published as *The Ice Nucleation Activity of Graphene and Graphene Oxides* in *The Journal of Physical Chemistry C* and have been partially reproduced (Häusler et al., 2018a).

Ice nucleating particles show a variety of different and complex mechanisms when interacting with water during the freezing process. To gain a fundamental understanding of the heterogeneous freezing mechanisms, studies with proxies for atmospheric ice nucleating particles must be performed. Graphene and its derivatives offer suitable model systems for soot particles, which are ubiquitous aerosols in the atmosphere. Here, the investigation of the ice nucleation activity of different types of graphene and graphene oxides is presented. Immersion droplet freezing experiments as well as additional analytical analyses, such as X-ray photoelectron spectroscopy, Raman spectroscopy and transmission electron microscopy, were performed. It is shown within a group of samples that a highly ordered graphene lattice (Raman G band intensity >50%) can support ice nucleation more effectively than a lowly ordered graphene lattice (Raman G band intensity <20%). Ammonia-functionalized graphene revealed the highest ice nucleation activity of all samples. Atmospheric ammonia is known to play a primary role in the formation of secondary particulate matter, forming ammonium-containing aerosols. The influence of functionalization on interactions between the particle interface and water molecules, as well as on hydrophobicity and agglomeration processes, is discussed.

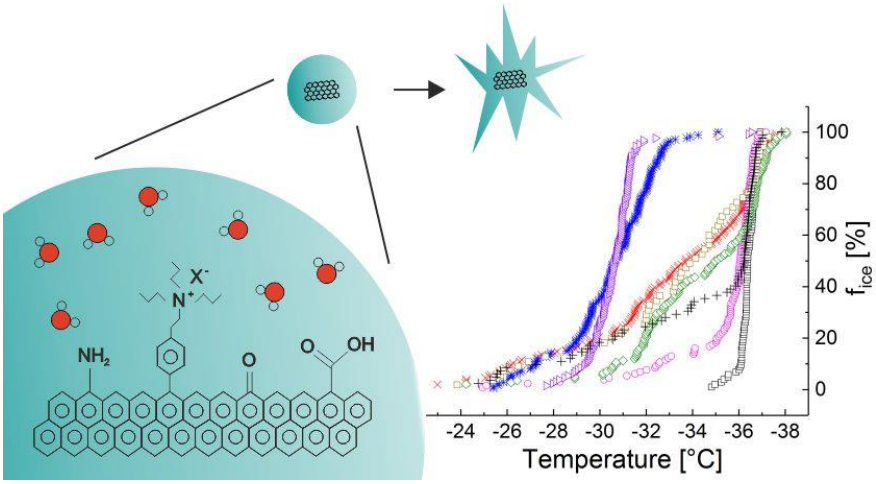

Figure 5-1 The Ice Nucleation Activity of Graphene and Graphene Oxides- graphical abstract.

5.1 Preparation of Suspension

A stable suspension of graphene and graphene oxides in ultrapure water was achieved by sonication for 5 minutes with an operating frequency of 40 kHz. Graphene is considered to disperse poorly in water (Konios et al., 2014; Johnson et al., 2015). Nevertheless, the oxidation of graphene together with the use of sonication allows graphene and graphene oxides to be dispersed in a larger number of solvents, including water (Konios et al., 2014; Johnson et al., 2015). The samples used in this work revealed a sufficient degree of oxidation to achieve stable suspensions. Images of the selected aqueous graphene and graphene oxide suspensions immediately after sonication and after settling for 30 minutes are shown in Figure 5-2.

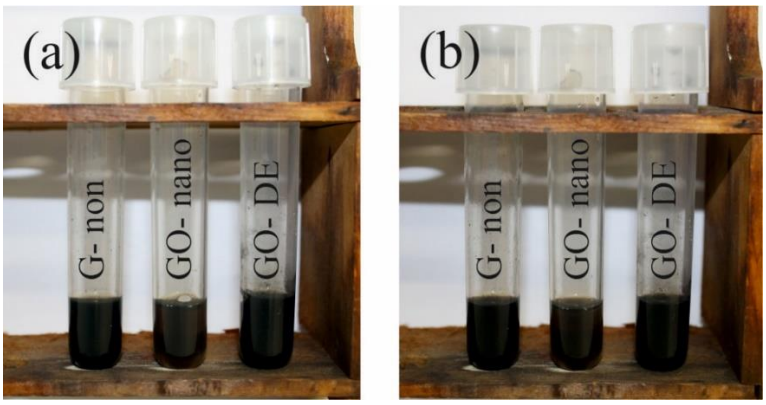

Figure 5-2 Graphene and graphene oxide suspensions with concentrations of 0.8% for G-non and GO-DE, 0.2% for GO-nano (a) immediately after sonication for 5 minutes and (b) after settling for 30 minutes.

To avoid any subsequent phase separation, further preparation steps were carried out immediately after sonication. Graphene samples from Sigma Aldrich were purchased directly as an aqueous suspension. The suspensions were emulsified into an oil matrix (80 wt% paraffin, 20 wt% lanolin), producing droplets in the micrometer range with a diameter of 20-80 µm. Only droplets with diameters between 35 µm and 45 µm were used for evaluation. The water-oil emulsion was put on a glass slide and placed on the TEC. The migration of individual particles into the oil phase cannot be excluded. To minimize migration, the time between emulsification and the start of the cooling process was intentionally kept short. A refreezing experiment was performed to demonstrate that no migration into the oil phase occurs during the freezing experiment (see Figure 5-3). Any migration of INP into the oil phase during the freezing process would lead to a decrease of surface area and hence INA. As demonstrated in Figure 5-3, no decrease of INA can be observed. We assume that due to the

high viscosity of supercooled water at operating temperatures below 0 °C no migration into the oil phase takes place.

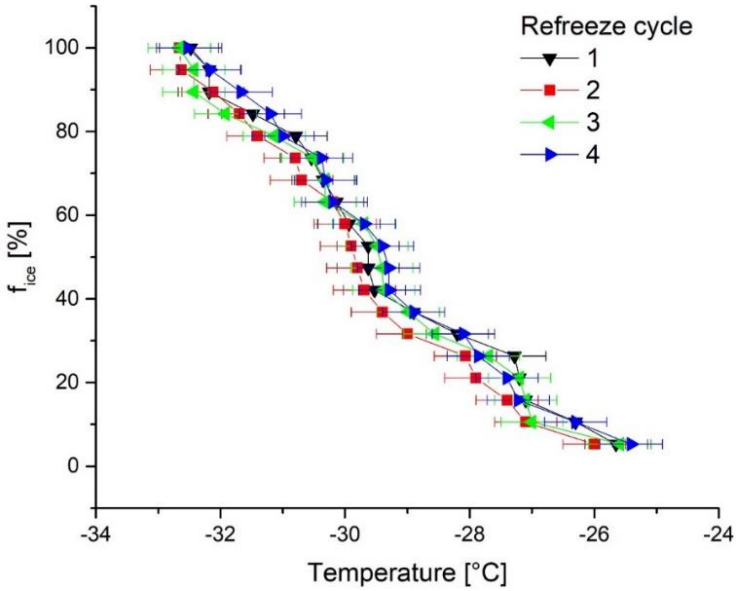

Figure 5-3 Freezing spectra of refreezing experiment with G-non. Error bars are accordingly to a temperature uncertainty of ±0.4 °C.

5.2 Description of Materials

We investigated a variety of functionalized and non-functionalized graphene and graphene oxide materials with different chemical and structural characteristics to evaluate the dependence of the INA on the surface chemistry, microstructure and lattice structure. Four graphene oxides (GO) were chosen for investigation: (i) GO synthesized by our group (GO-DE), (ii) GO purchased from Sigma-Aldrich (GO-SA), (iii) ammonia-functionalized GO (GO-NH_2) and (iv) nanosized colloidal GO (GO-nano). Moreover, three graphene samples were analyzed: (i) non-functionalized graphene (G-non) and (ii) and (iii) covalently functionalized graphene G-$NPr_3^+X^-$ (X=I and OH). Table 5-1 summarizes the material characteristics, including the source of synthesis and the specific surface area according to BET. The representative chemical structures are given in Figure 5-4.

Table 5-1 List of samples investigated, including the sources of each sample, BET-determined surface areas and a short description of the samples, including TEM-determined particle thickness and shape.

Material	Surface areas [m^2/g]	Description
Graphene oxides		
GO-DE[a]	112	Large single-layer graphene oxide sheets (>1 µm)
GO-SA[b]	<10	Large 2-7 multi-layer graphene oxide sheets (>1 µm)
GO-NH_2[b]	<10	Large 2-7 multi-layer graphene oxide sheets (> 1 µm), ammonia functionalized
GO-nano[b]	176	Graphene oxide nano-colloids with varying particle size/shape up to 200 nm and thickness of >3 nm.
Graphene		
G-non[c]	<10	Non-functionalized graphene flakes with a diameter of 400 nm and up to 7 layers; precursor for G-NPr_3^+I/OH^-
G-$NPr_3^+I^-$ [c]	<10	Covalently functionalized graphene with I^- as the counter ion; same form and shape as G-non
G-$NPr_3^+OH^-$ [c]	<10	Covalently functionalized graphene with OH^- as the counter ion; same form and shape as G-non

[a] *Synthesized by our workgroup*

[b] *Acquired from Sigma-Aldrich Chemistry*

[c] *Synthesized by the workgroup of Silvia Marchesan, Department of Chemical and Pharmaceutical Sciences, Università degli studi di Trieste*

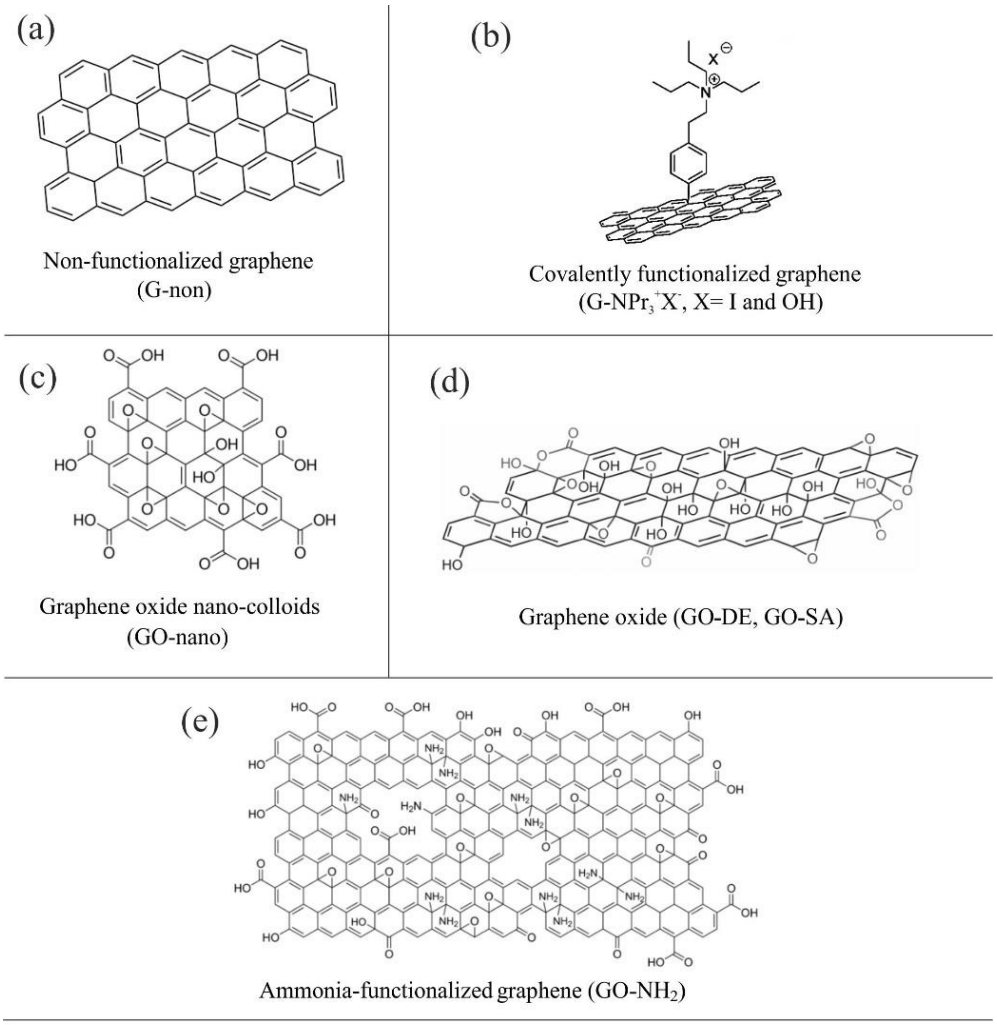

Figure 5-4 Representative chemical structures of the samples investigated: (a) non-functionalized graphene G-non (Chakrabarti et al., 2013), (b) covalently functionalized graphene G-$NPr_3^+X^-$ (X=I and OH), (c) graphene oxide nano-colloids GO-nano, (d) graphene oxide GO-DE and GO-SA (Gao et al., 2009) and (e) ammonia-functionalized graphene oxide GO-ammo*.*

** According to the provided datasheet of the purchased material from Sigma-Aldrich Chemistry.*

5.3 Results

The INA of the entire set of samples is shown in Figure 5-5. For clarity, the samples were divided into two groups according to their chemical characteristics: (i) graphene, including G-non, G-$NPr_3^+I^-$ and G-$NPr_3^+OH^-$, and (ii) graphene oxides, including GO-DE, GO-SA, GO-nano and GO-NH_2 (see Table 5-1).

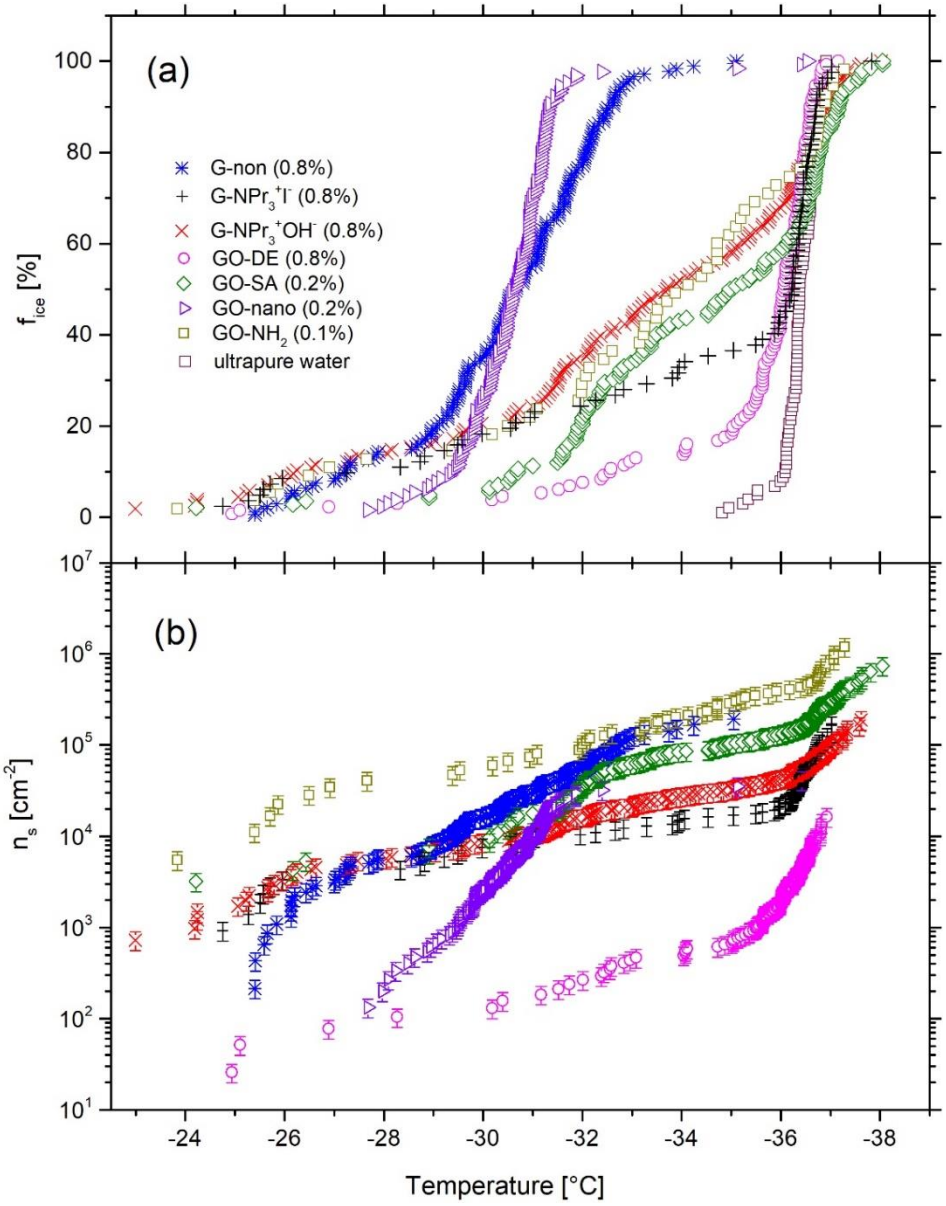

Figure 5-5 (a) Ratio of frozen droplets f_{ice} and (b) the ice nucleation active surface site density n_s at a given temperature for all investigated samples. The n_s value, the freezing temperature range, and the n_s trend provide key information on the characteristics of the ice-nucleation-active samples of graphene or graphene oxides. Some droplets nucleate at about -36 °C, meaning that they do not contain INPs. Experimental uncertainty in the n_s value was calculated by changes in the weight and droplet size.

5.3.1 Graphene

Covalently functionalized graphene (G-$NPr_3^+I^-$ and G-$NPr_3^+OH^-$) show a similar INA with slightly increased n_s values of G-$NPr_3^+OH^-$ between -30 °C and -36.5 °C compared to G-$NPr_3^+I^-$. In contrast, non-functionalized graphene (G-non) shows an increased ice nucleation activity once the temperature is below -28 °C compared to the functionalized samples. XPS measurements were performed to determine the elemental composition and the sp^2-hybridized carbon (C-sp^2) proportion (see Table 5-2 and Figure 5-6). The C-sp^2 proportions are representative for the graphitic carbon ratio. The detailed list of XPS-determined carbon components is given in Table 5-3. The composition of the three samples is similar and consists of approximately 91-92 at% carbon and 4-9 at% oxygen. G-$NPr_3^+I^-$ and G-$NPr_3^+OH^-$ show a nitrogen proportion of 3-4 at% as well as 1 at% iodine for G-$NPr_3^+I^-$ originating from the functionalization. The C-sp^2 proportions are between 72 at% for G-$NPr_3^+OH^-$ and 91 at% for G-$NPr_3^+I^-$.

Table 5-2 Elemental composition and sp^2-hybridized carbon proportion of all investigated graphene samples determined via XPS.

Sample	Element [at%]				C-sp^2
	C	O	N	I	[at%]
G-non	91	9			86
G-$NPr_3^+I^-$	92	4	3	1	91
G-$NPr_3^+OH^-$	92	4	4		72

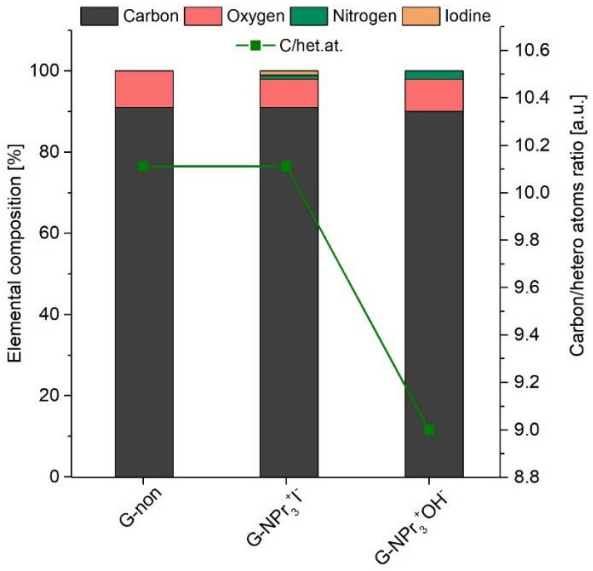

Figure 5-6 Elemental composition and carbon/hetero atoms ratio of all investigated graphene samples, determined via XPS.

Table 5-3 XPS-determined carbon components of all investigated graphene and graphene oxide samples.

	Component at% of C1s signal						
	Csp2	C-C/C-H	C-O	C=O	O-C=O	C shake up	C shake up2
Graphene							
G-non	85.5	7.5	3.1	0.5		2.8	0.5
G-$NPr_3^+I^-$	90.7	1.9	3.1		0.7	3.3	0.3
G-$NPr_3^+OH^-$	72.2	19.1	5.3	3.4			
Graphene oxides							
GO-DE	45.1	18.4	25.0	1.8	2.9	3.3	3.6
GO-SA	29.2	21.2	33.3	2.7	2.8	7.2	3.5
GO-NH_2	42.0	22.5	20.9	3.1	2.5	6.1	3.0
GO-nano	18.5	12.5	37.5	13.7	11.6	6.3	

Raman spectroscopy was performed and analyzed according to Sadezky et al. (2005) to distinguish differences in the microstructure, lattice disorder and short-range order. The Raman spectra (see Table 5-4, Figures 5-7 and 5-8) reveal that non-functionalized graphene (G-non) has fewer structural defects, shown by the lower intensity of the disordered band D1 (layer edge disorder) of 27% and the higher intensity of the ideal graphite band G of 69% compared to those of covalently functionalized graphene. Covalently functionalized graphene exhibits an integrated intensity of D1 of up to 40% for G-$NPr_3^+OH^-$ and 44% for G-$NPr_3^+I^-$. The intensity of D2 is shown to be similar, within a ±1% range for all three samples. The D/G ratio is a suitable indicator of the degree of disorder. The D/G ratio increases from G-non (0.45) to G-$NPr_3^+I^-$ (0.94), until it decreases and G-$NPr_3^+OH^-$ (0.75).

Table 5-4 Proportional intensities of fitted first-order Raman impulses (G, D1 and D2) according to Sadezky et al. (2005) and ratios of the Raman band intensity of the disordered to the ideal graphitic lattice (D/G) of all investigated graphene samples.

Sample	Proportional intensity of fitted bands [%]			
	G	D1	D2	D/G
G-non	69	27	4	0.45
G-$NPr_3^+I^-$	51	44	4	0.94
G-$NPr_3^+OH^-$	57	40	3	0.75

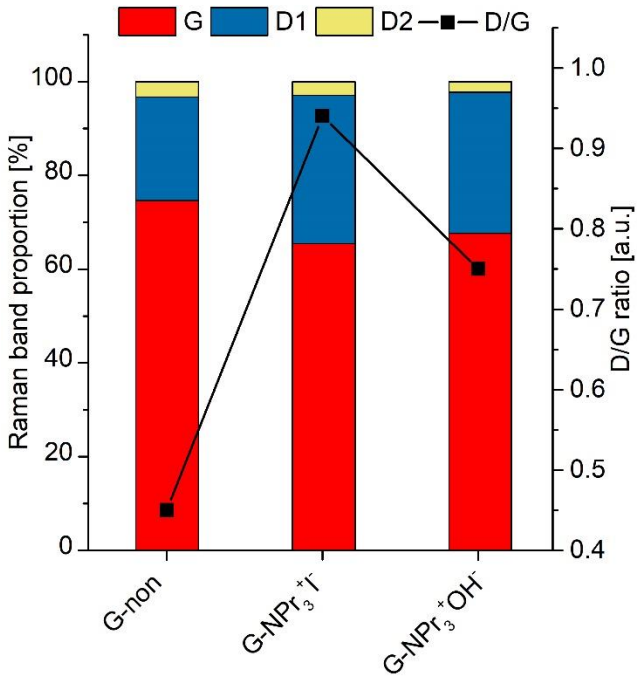

Figure 5-7 Proportions of each fitted first-order Raman impulse and the resulting D/G ratio of all graphene samples.

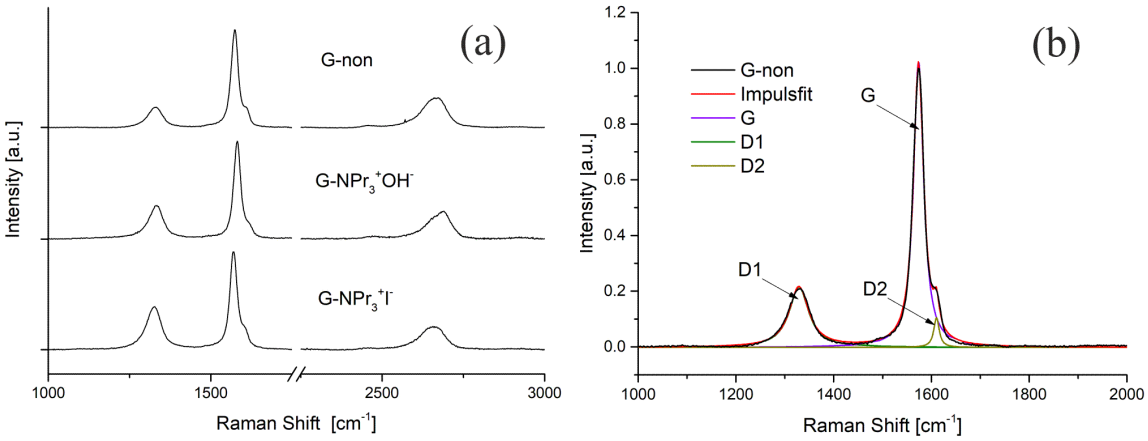

Figure 5-8 Raman spectra of (a) all investigated graphene samples and (b) non-functionalized graphene (G-non); first-order curve fitted with band combination according to Sadezky et al. (2005) (λ_0=633 nm).

Additionally, TEM measurements were performed to determine the morphology of the particles. The images reveal flakes with diameters of up to 400 nm and with up to 7 layers (see Figure 5-9) for all three graphene samples. Individual sheets of G-non, however, show additional accumulation, forming larger "fluffy" aggregates.

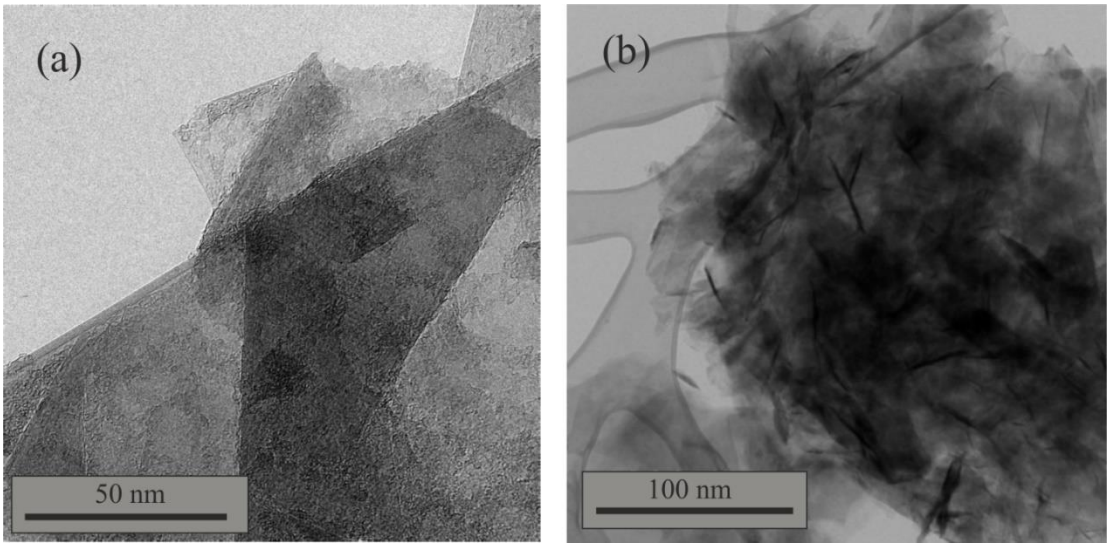

Figure 5-9 TEM images of graphene samples investigated: (a) non-functionalized graphene (G-non) indicates flakes with diameters of up to 400 nm and with up to 7 layers (Shearer et al., 2016) and (b) covalently functionalized graphene (G-NPr3+I- and G-NPr3+OH-) shows the same layer size and thickness as its non-functionalized precursor G-non but also shows individual sheets accumulating into larger "fluffy" aggregates.

5.3.2 Graphene Oxide

Graphene oxides show a broader variety of INA than graphene (see Figure 5-5). The n_s values of the chemically most similar graphene oxide samples GO-DE and GO-SA show a deviation of two orders of magnitude but increase at a similar rate over the entire temperature window. The n_s value of GO-SA increases from $3 \cdot 10^3$ cm^{-2} at -25 °C to 10^5 cm^{-2} at -35 °C, and that of GO-DE increases from 20 cm^{-2} at -25 °C to $7 \cdot 10^2$ cm^{-2} at -35 °C. GO-nano, on the other hand, initiates the ice nucleation process at a similar range as GO-DE at -27.5 °C, with a n_s value of 130 cm^{-2}. The n_s value, however, rises more steeply until it reaches the same value as GO-SA of $3 \cdot 10^4$ cm^{-2} at -32.5 °C. The functionalized graphene oxide sample (GO-NH_2) shows the highest INA of all samples investigated over the entire freezing process, revealing n_s values between 10^4 cm^{-2} at -25 °C and $3 \cdot 10^5$ cm^{-2} at -35 °C.

XPS measurements show a similar composition among all graphene oxide samples, that is, of approximately 67-73 at% carbon and 23-33 at% oxygen (see Table 5-5 and Figure 5-10). GO-nano is composed of an increased amount of oxygen (33 at%) and a consequently decreased proportion of carbon (67%). GO-NH_2 additionally consists of approximately 3 at% nitrogen due to the ammonia functionalization. The proportion of sp^2-hybridzed carbon lies between 19 at% for GO-nano and 45 at% for GO-DE.

Table 5-5 Elemental composition and proportion of sp^2-hybridized carbon (C-sp^2) of all investigated graphene oxide samples determined via XPS.

Sample	Element [at%]			C-sp^2 [at%]
	C	O	N	
GO-SA	71	28	<1	29
GO-DE	72	27	<1	45
GO-nano	67	33	<1	19
GO-NH_2	73	23	3	42

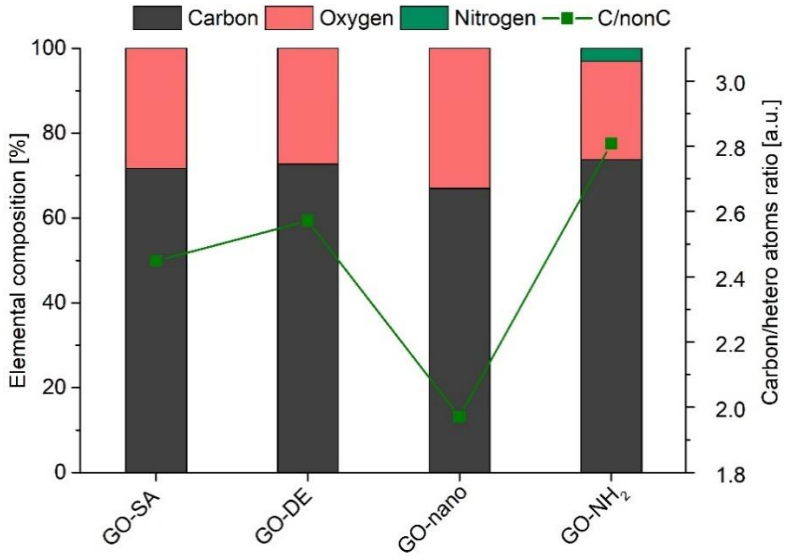

Figure 5-10 Elemental composition and carbon/hetero atoms ratio of all investigated graphene oxide samples, determined via XPS.

Furthermore, Raman spectroscopy reveals distinctions in lattice orders (see Table 5-6, Figures 5-11 and 5-12). In contrast to graphene, the graphene oxide samples show a more complex composition of lattice disorders. The D/G ratio increases from GO-SA (4.82) to GO-NH_2 (9.0). The D value summarizes the integral intensities of all D-bands (D1-D4): edge (D1) and surface (D2) disorders, amorphous graphene oxide features (D3) and ionic impurities/polyene disorders (D4). GO-DE exhibits an increased ratio of integrated intensities of D3 (7%) and D4 (4%) compared to the chemically most similar sample, GO-SA. The Raman spectrum of GO-nano reveals a disordered lattice with an integrated intensity of amorphous disorder of 11%, making this sample the most amorphous of all samples. Nevertheless, GO-NH_2 exhibits the more intense disorder, which is evident in the lowest integrated intensity of the ideal lattice of 10%.

Table 5-6 Proportional intensities of fitted first-order Raman impulses (G, D1 and D2) according to Sadezky et al. (2005) and ratios of the Raman band intensity of the disordered to the ideal graphitic lattice (D/G) of all investigated graphene oxide samples.

	Proportional intensity of fitted bands [%]					
	G	D1	D2	D3	D4	D/G
GO-SA	17	68	7	5	2	4.82
GO-DE	14	69	7	7	4	6.21
GO-nano	14	64	6	11	5	6.14
GO-NH2	10	70	8	8	4	9.0

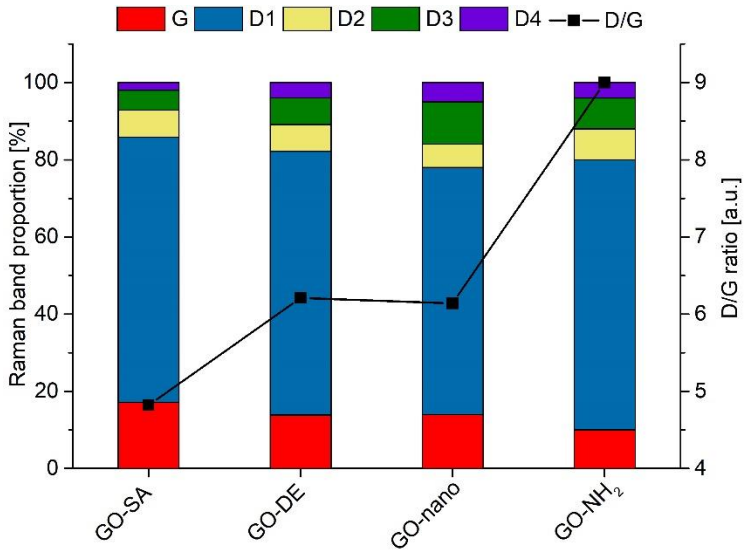

Figure 5-11 Proportions of each fitted first-order Raman impulse and the resulting D/G ratio of all graphene oxide samples.

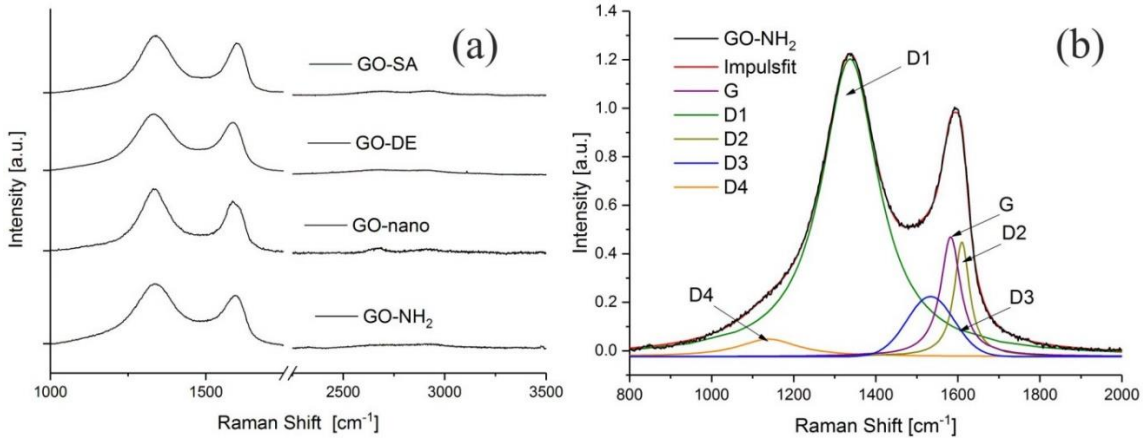

Figure 5-12 Raman spectra of (a) all investigated graphene oxide samples and (b) GO-NH_2; first-order curve fitted with band combination according to Sadezky et al. (2005) (λ_0=633 nm).

TEM analysis of GO-SA, GO-DE and GO-NH_2 reveal similar large flakes of several µm in diameter and a thickness of 2-7 layers. GO-nano, on the other hand, consists of particles of varying shapes and sizes of up to 200 nm and thicknesses of at least 3 nm (see Figure 5-13).

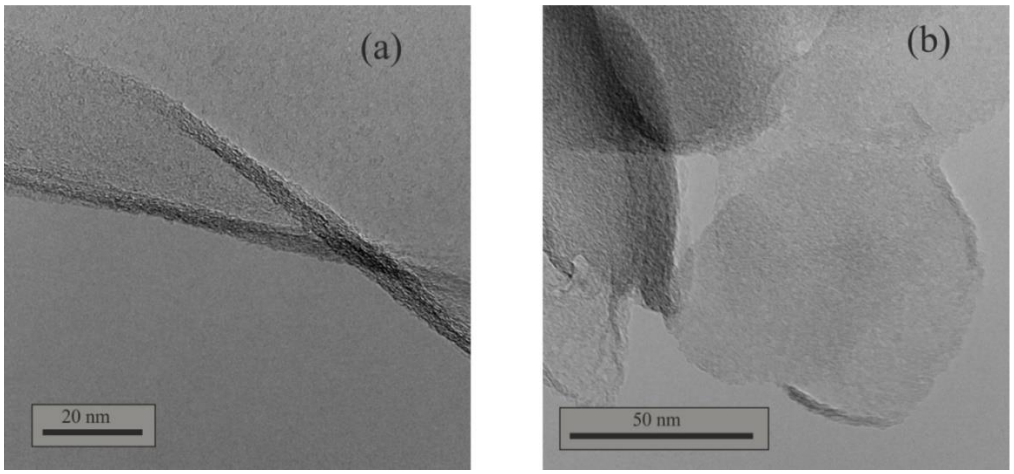

Figure 5-13 TEM images of the samples investigated: (a) non-functionalized (GO-SA and GO-DE) and ammonia-functionalized graphene oxides (GO-NH_2) reveal large flakes of approximately 5 nm thickness and several µm in diameter, and the thickness of the sheets and number of signals in the corresponding electron diffraction pattern (EDP) indicate multi-layer graphene composed of 2-7 layers, while (b) GO-nano consists of particles of varying shapes with sizes of up to 200 nm and thickness of at least 3 nm.

5.4 Discussion

5.4.1 Graphene

In Figure 5-5, the functionalized graphene samples show a similar INA, with slightly increased n_s values for G-$NPr_3^+OH^-$ between -30 °C and -36.5 °C. In contrast, non-functionalized graphene (G-non) shows an increased INA above -28 °C compared to the functionalized samples. TEM analyses indicate that the flake and layer size of functionalized graphene stay nearly the same as that of non-functionalized graphene. Differences in composition revealed by XPS might influence the INA due to the introduction of additional functional sites able to interact with water molecules and trigger ice formation. This would be consistent with the classical *chemical-bonding* requirement stated by Pruppacher and Klett (1997). The Raman data revealed that covalently functionalized graphene (G-$NPr_3^+I^-$ and G-$NPr_3^+OH^-$) exhibits an increased integrated intensity of lattice disorders. With a decrease in the D/G ratio of functionalized graphene, the INA decreases at a similar rate (see Table 5-4). The functionalization process seems to have a major influence on the INA. The ordering process of water molecules at the water-graphene interface supports heterogeneous ice nucleation and depends on the lattice features. Disorientations of the lattice disturb the interaction with liquid water and therefore lower the INA of graphene. Thus, the graphene lattice is a significant parameter influencing the INA of graphene and is also responsible for the INA of soot particles. This is consistent with calculations of Lupi et al. (2014), Lupi and Molinero (2014), and Bi et al. (2016) and the laboratory work of Whale et al. (2015b), which revealed that the ordering of liquid water on an ideal graphitic lattice plays an important role in the heterogeneous ice nucleation mechanism and any oxidation, roughness or curvature was found to decrease the observed nucleation temperature. Nevertheless, accumulations of G-$NPr_3^+I^-$ and G-$NPr_3^+OH^-$ flakes into larger aggregates, as demonstrated in Figure 5-9, may reduce the INA by reducing the available active surface area, which needs to be considered. According to the data obtained in this study, it can be stated that the lattice conditions have an impact on the INA of graphene, yet the influence of agglomeration and functionalization cannot be excluded. However, more graphene species need to be investigated to state a significant trend and distinguish the relevance of each influence.

5.4.2 Graphene Oxides

The INA of graphene oxide appears to be more complex. In contrast to graphene, the graphene oxide samples not only show significant differences in composition but also experience additional lattice disorder. Due to oxidation, the C-sp^2 proportions of the graphene oxides were cut by one half compared to the graphene samples due to an increased amount of carbon-containing contaminants (see Tables 5-2 and 5-5). The n_s values of the chemically most similar graphene oxide samples, GO-DE and GO-SA, show a deviation of two orders of magnitude but increase at a similar rate over the entire temperature window. Furthermore, a consistent chemical composition and particle form was shown for both samples. In contrast, the lattice of GO-DE features an increased portion of structural disorder (D/G of 6.21) compared to GO-SA (D/G of 4.82). Due to the similarity in composition and particle shape, the significant differences in lattice order of GO-DE and GO-SA may account for the activity difference observed for the graphene samples. However, the observed dependence of INA on the lattice order cannot be applied to all graphene oxide samples investigated. In particular, GO-nano initiates ice nucleation in the same range as GO-DE, but nucleation increases substantially more steeply until it reaches the same value as GO-SA at -32.5 °C (see Figure 5-5). The degree of graphitization, however, is in the same range as that of GO-DE and GO-SA, with an amorphous proportion of 11% being the highest of all samples (see Table 5-6). GO-nano shows an increased amount of oxygen (33 at%) and a corresponding decreased proportion of carbon (see Table 5-5). Nevertheless, GO-nano consists of significantly smaller particles of varying shapes and sizes of up to 200 nm and thicknesses of at least 3 nm (see Figure 5-13). Based on the data, three features may account for the increased INA of GO-nano: (i) the particle shape of GO-nano may cause an increase in the INA due to the beneficial arrangement of functional sites on the surface, (ii) additional oxygen groups act as functional sites and improve the interaction of the graphene oxide interface with water molecules due to a possible increase in hydrogen bonds, and (iii) the increased proportion of oxygen increases the hydrophilicity of graphene, reduces agglomeration and hence increases the surface area. However, the influence of hydrophilicity and the resulting agglomeration is not clear. Biggs et al. (2017) reported an increase in the INA due to a decreased in hydrophilicity. The resulting agglomeration may have led to a favorable positioning of the functional site and therefore to an increase in the INA, even though a decrease in the surface area occurs.

XPS measurements of GO-NH_2 revealed a composition of 73 at% carbon, 23 at% oxygen and 3 at% nitrogen due to functionalization. GO-NH_2 exhibits the highest integrated intensity of disorder (G<10%) and the highest INA of all samples investigated. Amines are known to be

more hydrophilic than comparable organic hydrocarbons due to their polarity and basicity (Schirmeister et al., 2016). They therefore interact more easily with other polar groups, such as water molecules, via hydrogen bonds and may act as functional sites, increasing the INA. However, very few proteins show INA, despite containing lysine, an amino-group-containing amino acid, and instead are known to act as anti-freezer.(Watanabe et al., 1988; Zachariassen and Kristiansen, 2000) The influence of increased hydrophilicity and therefore reduced agglomeration of G-NH_2 flakes in aqueous suspension may lead to an increased INA and cannot be excluded. Exfoliation can lead to an increase in the surface area and hence may increase the INA.

5.5 Summary

The INA of different types of graphene and graphene oxides has been investigated. Immersion drop freezing experiments as well as additional analytical analyses such as X-ray photoelectron spectroscopy, Raman spectroscopy and transmission electron microscopy have been performed to gain insight into the surface chemistry, microstructure and lattice structure of the INPs.

The investigation of graphene and graphene oxides show that the lattice order can have a major impact on the INA. The introduction of different kinds of disorders (layer edges, amorphousness, impurities, etc.) can influence the ability to perform heterogeneous ice nucleation. The ordering of water molecules at the interface to perform heterogeneous ice nucleation seems to depend on the graphitic lattice. Disorders in the lattice disturb the interactions with liquid water and therefore lower the INA of graphene. However, the observed dependence of the INA on the lattice order cannot be applied to all investigated graphene oxide samples. In particular, GO-NH_2 exhibits the highest proportion of disorder ($G<10\%$) and revealed the highest INA of all samples investigated. Functionalization with amines influences the INA by increasing the number of functional sites and/or by increasing the hydrophilicity.

In general, two other INP characteristics in addition to the lattice order were shown to influence the INA of graphene and graphene oxides: (i) the particle size, in particular that within the nanometer range, may cause an increase in the INA due to the beneficial arrangement of functional sites on the surface and (ii) the degree of oxidation, which influences the hydrophilicity, reduces agglomeration and hence increases the surface area, as well as generates functional sites.

The impact of the lattice order was demonstrated. Additionally, differences in structure, size and functionalization between the investigated samples were shown. More species with closely controlled differences need to be investigated to state a firm experimental conclusion about the effect of each feature on the INA. Therefore, declarations of the most decisive ice nucleation feature cannot be made. A variety of features relevant to ice nucleation were shown to be essential when describing the ice nucleating behavior of graphene and graphene oxides.

6. The Ice Nucleation Activity of Black and Brown Soot Aged by Exposure to NO_2 and SO_2

Portions of this chapter were previously submitted as *The Ice Nucleation Activity of Black and Brown Soot Aged by Exposure to NO_2 and SO_2* to the *Journal of Geophysical Research-Atmospheres* and have been partially reproduced (Häusler et al., submitted 2018).

The ice nucleation activity of soot was studied experimentally. Two different types of soot were produced by burning a propane-air mixture under controlled conditions with a miniCAST (Combustion Aerosol Standard) burner. Depending on the mixture proportions of the burner, soot with high (brown carbon) and low organic content (black carbon) was obtained. Subsequent reactions of the soot with NO_2 and SO_2 were carried out in a reaction chamber with exposure times between 30 and 360 minutes. Untreated and treated soot samples were analyzed for their INA in immersion freezing experiments. Their composition was analyzed via X-ray photoelectron spectroscopy, their microstructure via Raman spectroscopy and their morphology via transmission electron microscopy. We show that the INA of soot with a high composition of organic material was increased significantly after the reaction with NO_2 and SO_2. The heterogeneous mean freezing temperature was increased by 10-12 °C to about -25 °C. Untreated and NO_2 treated black carbon showed no INA but after 30 minutes of SO_2 exposure the heterogeneous mean freezing temperature shifted by 15 °C to -22 °C. Analytical methods revealed that the surface composition as well as the degree of graphitization have an impact on the INA. The interplay between properties relevant for ice nucleation, such as the chemical composition and the microstructure of the soot's surface, which is closely related to each other, is important and needs to be considered when predicting the ice nucleating ability of soot.

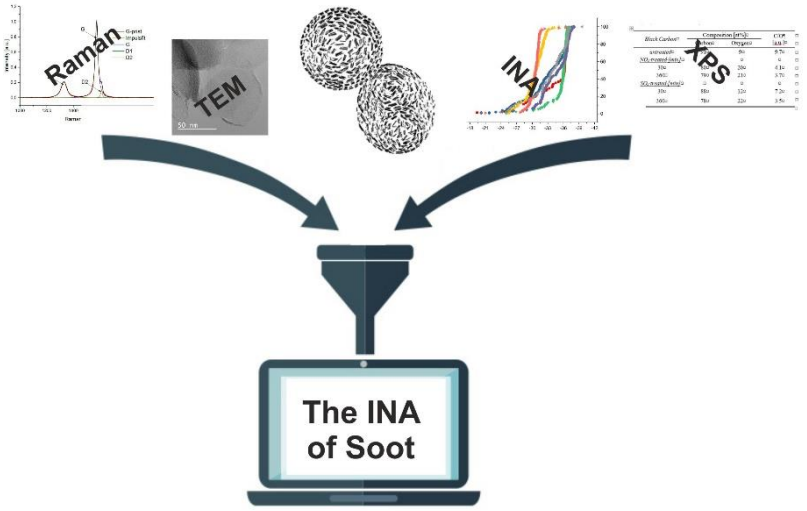

Figure 6-1 The Ice Nucleation Activity of Black and Brown Soot Aged by Exposure to NO_2 and SO_2- graphical abstract.

6.1 Soot Preparation and Gaseous Treatment

Soot particles were produced with a miniCAST (Combustion Aerosol Standard) soot generator type 5201C (Jing-CAST Technologies). In the CAST burner, propane is combusted with air in a co-flow diffusion flame (80-110 °C Jing, personal communication). The ratio of air to fuel can be adjusted to modify the composition and structure of the particles. Operating conditions are described in terms of the carbon-to-oxygen ratio. The flame is quenched with N_2 directly after combustion in order to prevent further combustion processes. Subsequently, the particle stream is diluted with compressed air.

According to the manufacturer and several studies, e.g. by Kim et al. (2015) or Mamakos et al. (2013), the structure of the particles generated by the miniCAST burner is similar to that of diesel soot (see Chapter 1.5.2). An oxygen rich flame results in agglomerates of small spherical primary soot particles, which are typical structures for diesel exhaust particles (Kim et al., 2015). Oxygen poor burning conditions, on the other hand, form less structured particles with a high amount of organic carbon. The burning conditions are chosen according to the carbon to oxygen ratio of the burning gas mixture (C/O_{BGM}). In earlier studies, the optical and thermal properties of CAST soot produced under different C/O_{BGM} ratios were investigated (Kim et al., 2015). Soot generated under oxygen rich conditions (low C/O_{BGM} ratio) was found to consist mainly of thermally highly refractory carbon (i.e. elemental carbon (EC) in thermal carbon analyzers) with optical characteristics corresponding to black carbon obtained from optical analyses. On the other hand, soot generated under oxygen poor conditions (high C/O_{BGM} ratio) was found to have a high content of brown carbon. The burning conditions for the two types of soot analyzed here are listed in Table 6-1.

Table 6-1 MiniCAST flow rates and burning gas mixture ratios (C/O_{BGM}) used for soot production. Elemental carbon (EC) and organic carbon (OC) proportion of each sample. EC and OC were determined using a thermo-optical OC/EC analyzer (Dual-Optical Lab Instrument, Sunset Laboratory Inc.).

Soot sample	Propane [ml/min]	Air [l/min]	Dilution air [l/min]	C/O_{BGM} [a.u.]	EC [%]	OC [%]
Brown carbon (BrC)	80	0.95	10	0.60	1.87	87.13
Black Carbon (BC)	50	1.49	10	0.24	49.58	50.42

The collection of the soot particles was performed with a modified six stage Berner low pressure cascade impactor (Berner, 1976) on polyvinyl fluoride (PVF) Tedlar® foils. Only the pre-precipitator stage and the first stage of the impactor (lower cut sizes 10 µm and 0.1 µm, respectively) were used to sample roughly the whole size range on a single foil.

The samples were treated with NO_2 and SO_2 in a reaction chamber consisting of a glass flask of 300 ml volume equipped with several connectors to flush the chamber. The PVF foils with the soot samples were placed in the flask, which was subsequently flushed with SO_2 and NO_2 respectively. After 30, 120, 180 and 360 minutes, the reaction chamber was flushed with argon and one particular sample was removed from the chamber and stored in a desiccator under vacuum to prevent further reactions with atmospheric gases. The chamber was afterwards flushed again with NO_2 and SO_2 to continue the aging process of the remaining samples. Exposure of the soot samples to ambient air during subsequent analyzation was kept intentionally short to ensure that no further aging processes takes place.

6.2 Results

For clarity the samples were divided into two groups according to their chemical characteristics: (i) black carbon (BC) and (ii) brown carbon (BrC). Both defined as a particulate primary, carbonaceous product from an incomplete combustion process of natural or anthropogenic origin (Gorbunov et al., 2001). However, the BC is primarily released by high-temperature combustion under oxygen rich burning conditions, while BrC is emitted by oxygen poor burning conditions. These two are the two most important light absorbing substances in the atmosphere (Andreae and Gelencser, 2006). Figure 6-2 displays that BrC appears brown or yellow, as BC appears to be black.

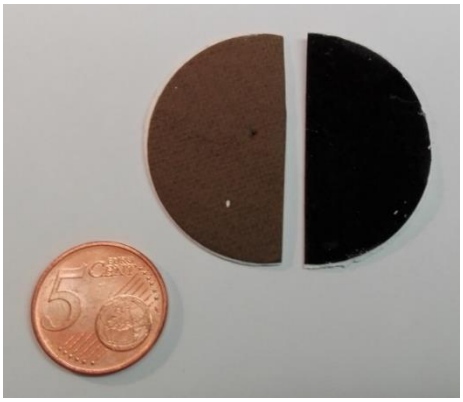

Figure 6-2 Brown and black carbon collected on a quartz filter.

6.2.1 Black Carbon

XPS measurements revealed a decrease in the C/O ratios (see Table 6-2 and Figure 6-3) and confirmed a change in the surface composition of BC via NO_2 or SO_2 vapor-phase treatment. Untreated BC showed a chemical composition of 91% carbon and 9% oxygen with a C/O ratio of 9.7. The oxygen uptake by NO_2 occurred primarily within the first 30 minutes of exposure, resulting in a chemical composition of 80% carbon and 20% oxygen (C/O of 4.1) after 30 minutes and 79% carbon and 21% oxygen (C/O of 3.7) after 360 minutes. SO_2-treated BC reached the same level of oxygen content after 360 minutes of treatment. However, the change was more gradual with the oxygen content increasing to 12% (C/O of 7.2) after 30 minutes and to 22% (C/O of 3.5) after 360 minutes.

Table 6-2 Elemental composition of untreated and vapor-phase-treated brown carbon, including the carbon/oxygen ratio (C/O), determined via XPS.

Black Carbon	Composition [at%]		C/O [a.u.]
	Carbon	Oxygen	
untreated	91	9	9.7
NO_2 treated [min]			
30	80	20	4.1
360	79	21	3.7
SO_2 treated [min]			
30	88	12	7.2
360	78	22	3.5

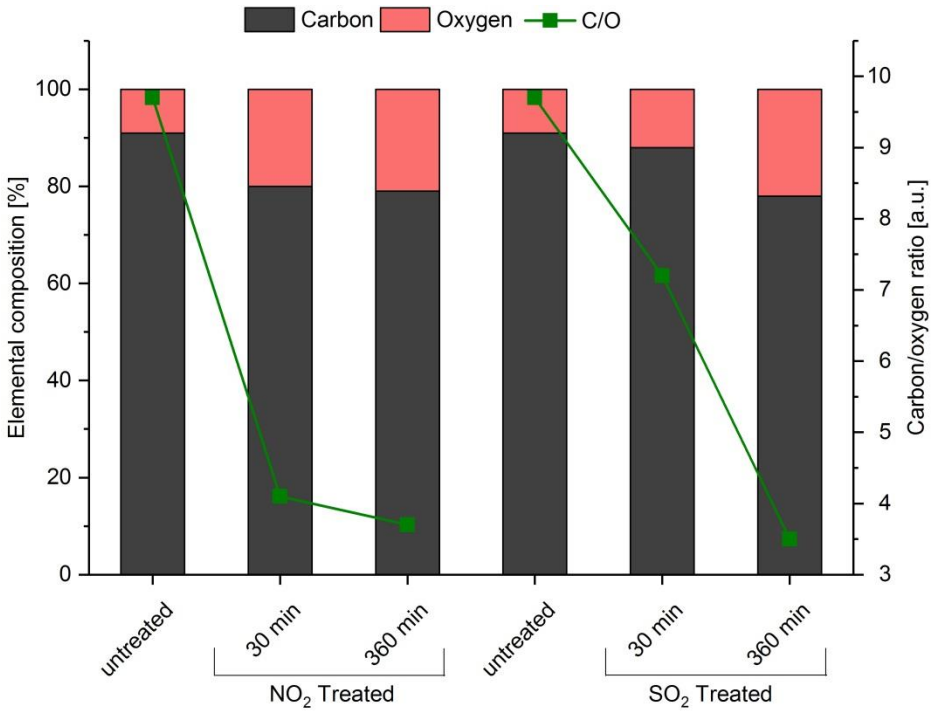

Figure 6-3 Elemental composition and carbon/oxygen ratios of untreated and vapor-phase-treated black carbon.

To determine the influence of the chemical composition changes of the surface on the morphology, microstructure and lattice disorder on soot, TEM analysis and Raman spectroscopy were performed. The Raman spectra of the treated and untreated samples were analyzed according to Sadezky et al. (2005) to distinguish differences in the lattice structure (see Table 6-3 and Figure 6-4). The integrated intensity ratio of the ideal graphitic band to all disordered graphitic lattice bands (G/D) was used to describe the lattice condition (degree of graphitization). The G/D ratio of BC decreased by half after 30 minutes of NO_2 treatment from 0.21 to 0.10 and remained constant afterwards. The degree of graphitization increased within the first 30 minutes of SO_2 exposure, resulting in a G/D ratio of 0.35 until it diminished with further exposure to 0.10. The first 30 minutes of SO_2 treatment left the

graphitic nature of soot more intact in comparison to the NO_2 treatment, which is in line with the observed level of oxygen content from XPS. The decrease in G/D ratios during the treatment indicated a loss of graphitic structure due to chemical reactions on the surface. Chemical reactions damaged the graphitic structure by generating disorders in the graphitic lattice of the soot.

Table 6-3 Proportion of fitted first-order Raman impulses according to Sadezky et al. (2005) and the integrated intensity ratio of ideal graphitic band G and sum of disordered bands D of black carbon.

Proportion of	Duration of treatment [min]			
fitted bands [%]	untreated	30	120	360
NO_2 treated				
G	17	9	9	8
D	83	91	91	92
G/D	0.21	0.10	0.10	0.10
SO_2 treated				
G	17	26	10	9
D	83	74	90	91
G/D	0.21	0.35	0.11	0.10

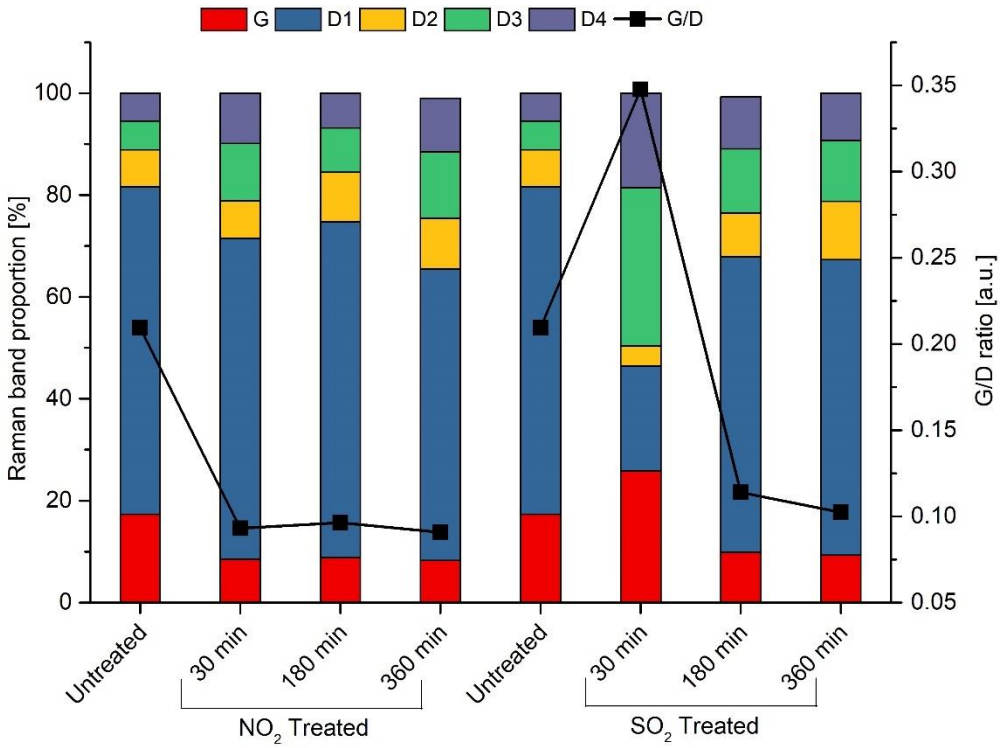

Figure 6-4 Proportions of each fitted first-order Raman impulse and the resulting G/D ratio of untreated, NO_2 and SO_2 treated black barbon.

TEM measurements showed that the particles of untreated black carbon had sizes between 10 nm and 20 nm. After NO_2 exposure, particle sizes varied from 10 nm to 50 nm. After the SO_2 treatment, most particles had sizes of about 50 nm (see Figure 6-5). Generally, boundaries between the smaller particles seemed to become less distinct after both treatments, where this effect seemed to be more pronounced for the SO_2 treated sample. Small particles of untreated BC showed the typical onion like soot structure (e.g. Knauer et al. (2009) while larger-sized particles do not show the graphitic layering and are often embedded in clusters (see Figure 6-6).

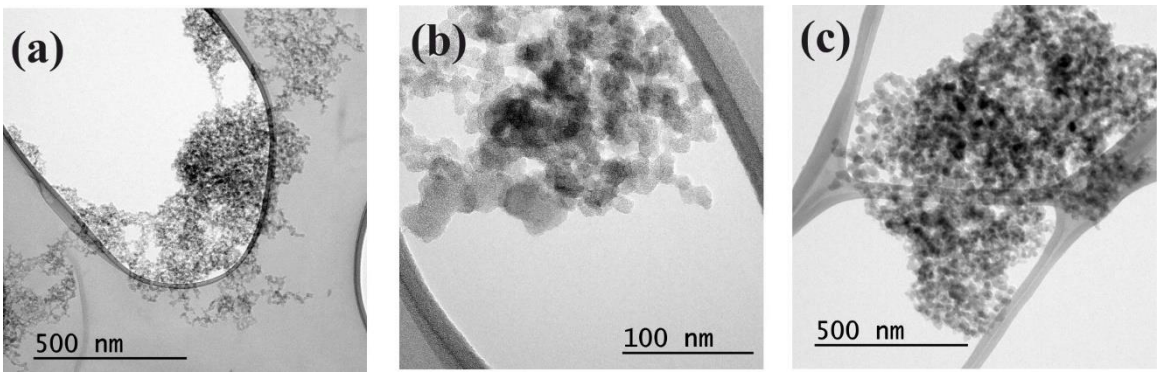

Figure 6-5 TEM images of (a) untreated, (b) 360 minutes NO_2 and (c) 360 minutes SO_2 vapor-phase-treated black carbon. Initial particle sizes of untreated black carbon are approximately 10- 20 nm. After (a) NO_2 exposure there is a mix of small and larger particles varying from 10 to 50 nm and after (b) SO_2 treatment the majority of particles have sizes of around 50 nm (c). Agglomerations to clusters can be seen in all three images.

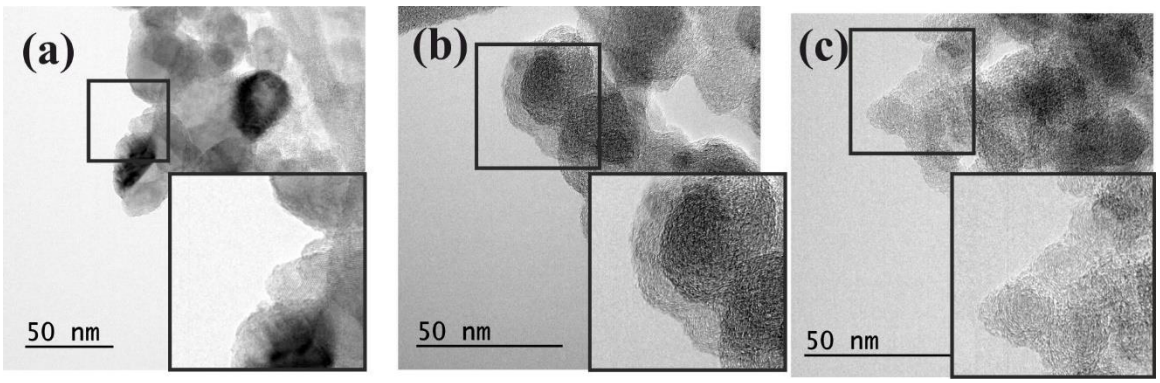

Figure 6-6 TEM images of (a) untreated, (b) 360 minutes NO_2 and (c) 360 minutes SO_2 vapor-phase-treated black carbon. After the treatment the boundaries between the particles become less distinct and diminish.

The INA, including how it is influenced by the gaseous treatments, was determined by means of immersion freezing experiments. The freezing spectra revealed that untreated and NO_2-treated BC did not show any INA (freezing temperatures below -35 °C). In contrast, BC showed INA after 30 minutes of SO_2 treatment ($T_{50,hetero}$ of -22 °C) but no INA after further exposure (freezing temperatures below -35 °C). Approximately 65% of all observed droplets containing BC treated for 30 minutes with SO_2 froze heterogeneously ($f_{ice,hetero}$). However, BC treated for 180 minutes with SO_2 showed a reduced $f_{ice,hetero}$ value of 15%. The freezing spectra of BC and its modifications are shown in Figure 6-7.

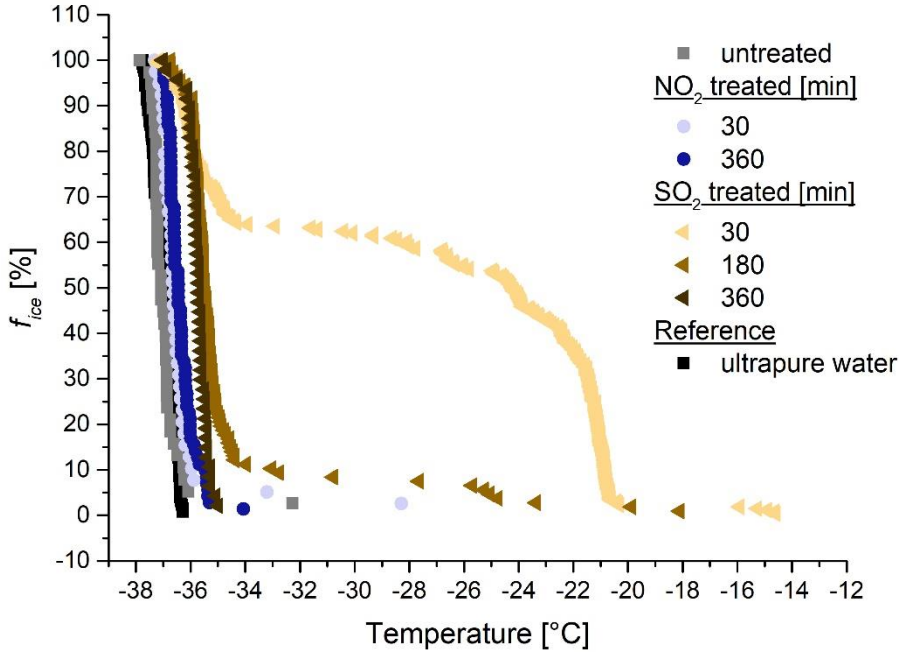

Figure 6-7 Freezing spectra of untreated and vapor-phase-treated black carbon.

6.2.2 Brown Carbon

XPS measurements revealed a decrease of C/O ratios (see Table 6-4 and Figure 6-8) and confirmed a successful reaction of BrC via NO_2 and SO_2 vapor phase treatment. Untreated BrC featured a chemical composition of 89% carbon and 11% oxygen, with a C/O ratio of 7.7. The majority of oxygen uptake (> 50%) takes place within the first 30 minutes for both gaseous treatments. Within the first 30 minutes of reaction, C/O ratios of 5.9 for NO_2 treated and 7.1 for SO_2 treated BrC were achieved. After 360 minutes of exposure, a C/O ratio of 5.4 and 6.7 was reached with NO_2 and SO_2, respectively.

Table 6-4 Elemental composition of untreated and vapor-phase-treated brown carbon, including the carbon/oxygen ratio (C/O), determined via XPS.

Brown Carbon	Composition [at%]		C/O [a.u.]
	Carbon	Oxygen	
Untreated	89	11	7.7
NO_2 treated [min]			
30	86	14	5.9
360	84	16	5.4
SO_2 treated [min]			
30	88	12	7.1
360	87	13	6.7

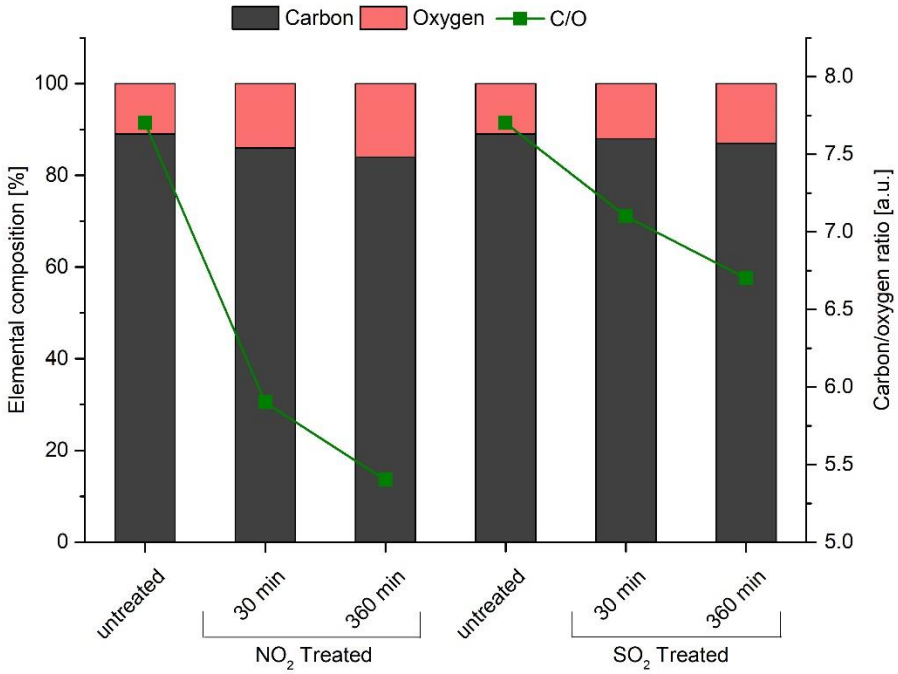

Figure 6-8 Elemental composition and carbon/oxygen ratios of untreated and vapor-phase-treated brown carbon.

Raman spectroscopy revealed the influence of chemical treatment on the lattice structure. The integrated intensity of the G band proportion decreased after NO_2 treatment from 12% to 9%, while the SO_2 treatment caused a decrease to 6% (see Table 6-5 and Figure 6-9). A steady drop in the G/D ratio within continuing NO_2 treatment until a value of 0.10 was reached. The G/D ratio of SO_2 treated BrC fell rapidly within the first 30 minutes to 0.09 and slowed down afterwards until a ratio of 0.07 was reached after 360 minutes. The loss of graphitic structure due to the treatment is indicated by the decrease in the G/D ratios.

Table 6-5 Proportion of fitted first-order Raman impulses according to Sadezky et al. (2005) and the integrated intensity ratio of ideal graphitic band G and sum of disordered bands D of brown carbon.

Proportion of fitted bands [%]	Duration of treatment [min]				
	Untreated	30	120	180	360
NO_2 treated					
G	12	11	11	10	9
D	88	89	90	90	91
G/D	0.14	0.13	0.12	0.10	0.10
SO_2 treated					
G	12	8	8	7	6
D	88	92	92	93	94
G/D	0.14	0.09	0.08	0.08	0.07

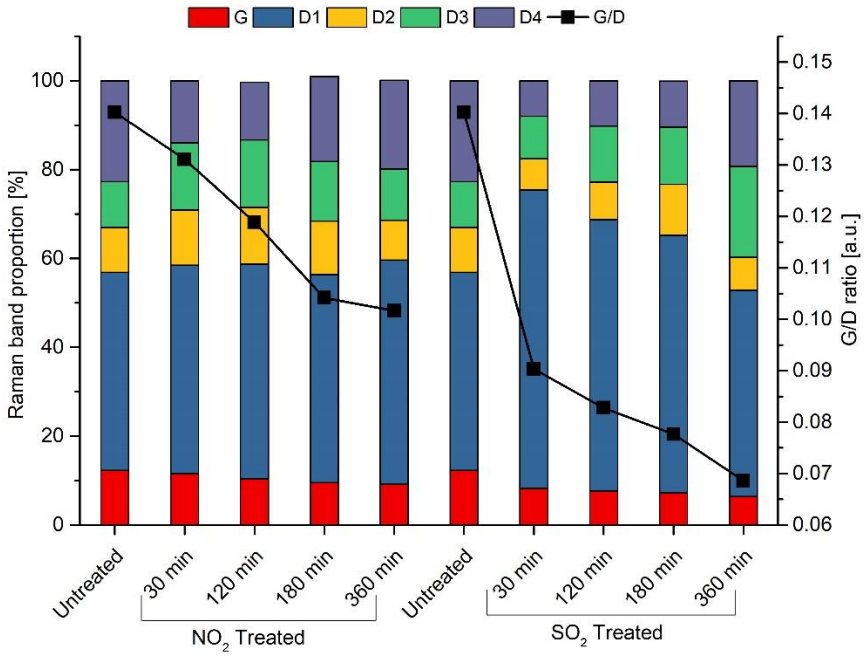

Figure 6-9 Proportions of each fitted first-order Raman impulse and the resulting G/D ratio of untreated, NO_2 and SO_2 treated brown carbon.

TEM measurements revealed that untreated BrC showed less graphitic structure than BC. The vapor treatments smoothed the particle boundaries and reduced the graphitic structure (see Figure 6-10). The loss of structure seemed to be even more pronounced during the SO_2 treatment. Vapor treated samples looked more like an interconnected carbon structure than single particles.

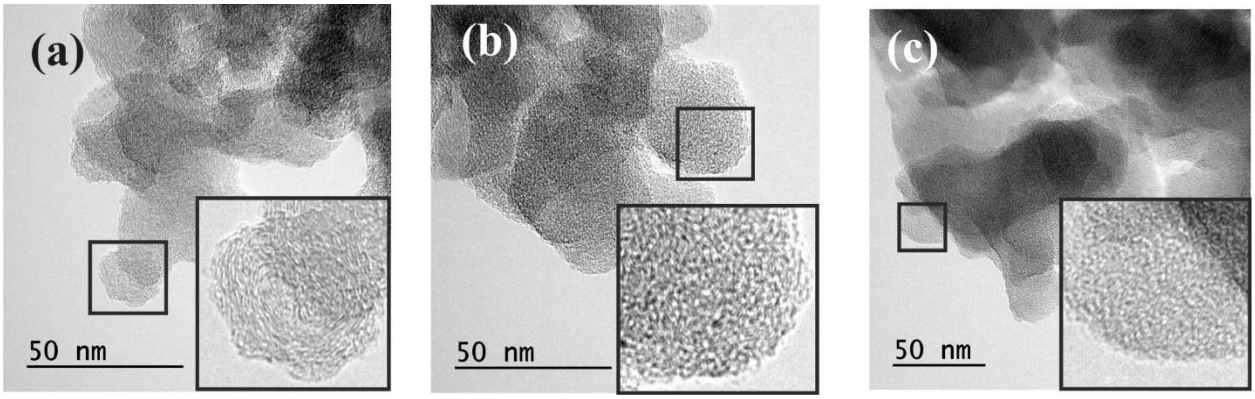

Figure 6-10 TEM pictures of (a) untreated, (b) 360 min NO_2 and (c) 360 min SO_2 vapor-phase-treated brown carbon. (a) Untreated brown carbon has little graphitic structure. (b) NO_2 and (c) SO_2 vapor treatments cause further decrease of structure, whereby the particles appear to be one porous piece of carbon.

The INA of the brown carbon samples before and after vapor treatment is shown in Table 6-6 and Figure 6-11. The freezing spectra showed that untreated BrC had an $f_{ice,hetero}$ value of about 10% and $T_{50,hetero}$ of -32 °C. The SO_2 and the NO_2 vapor phase treatments increased the INA stepwise with continued exposure. Both treatments increased the $T_{50,hetero}$ value after 360 minutes of treatment from -32 °C to -26.5 °C by NO_2 and -24.1 °C by SO_2 exposure (see Table 6-6). Furthermore, the proportion of heterogeneously frozen droplets $f_{ice,hetero}$ rose stepwise with ongoing treatment. After 360 minutes of NO_2 and SO_2 exposure, BrC has an $f_{ice,hetero}$ value of 100% and 40%, respectively.

Table 6-6 Proportion of heterogeneously frozen droplets ($f_{ice,hetero}$) and the mean freezing temperature at which 50% of heterogeneously frozen droplets are frozen ($T_{50,hetero}$) in immersion freezing experiments with NO_2 and SO_2 exposed brown carbon as INP.

Brown Carbon	$T_{50,hetero}$ [°C]	$f_{ice,hetero}$ [%]
Untreated	-32.0	10
NO_2 treated [min]		
30	-29.3	45
120	-27.8	85
180	-27.0	90
360	-26.5	100
SO_2 treated [min]		
30	-34.0	20
120	-32.8	25
180	-25.6	25
360	-24.1	40

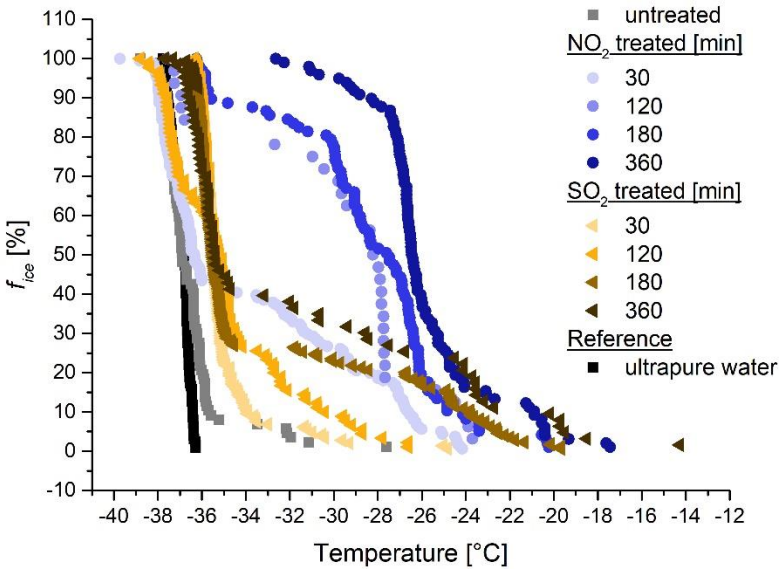

Figure 6-11 Freezing spectra of untreated and vapor-phase-treated brown carbon.

6.3 Discussion

6.3.1 Black Carbon

The expected reduction in the organic residuals due to the high oxygen content in the CAST flame (Mamakos et al., 2013; Kim et al., 2015) was confirmed by the low C/O ratio of untreated BC measured by means of XPS (see Figure 6-12). Furthermore, the successful surface reaction via gaseous treatments was confirmed by the decreasing C/O ratios with ongoing exposure. Untreated BC exhibited a C/O ratio of 9.7 and an increase of oxygen content by both treatments to a similar C/O ratio of approximately 3.6 after 360 minutes. However, the reaction kinetics of the samples differ significantly. While SO_2 reacts with BC more regularly during the whole exposure period, the reaction with NO_2 occurs mostly (> 90%) within the first 30 minutes of treatment. The reaction power of NO_2 is particularly high but weakens after a certain degree a specific oxygen composition is reached. The concentrations of nitrogen and sulfur on the soot's surface were too low to be detected via XPS.

The decrease in the G/D ratios during the NO_2 and SO_2 treatment is consistent with studies by others, e.g., Sadezky et al. (2005) or Song et al. (2006). Because of the surface reactions, the idealized graphene lattice incorporates more heteroatoms and becomes fractured. Therefore, the degree of graphitization decreases.

The INA of NO_2-treated BC does not increase with ongoing treatment. The freezing temperatures of untreated and NO_2-treated BC remain below the homogeneous freezing temperature of -35 °C. Therefore, untreated and NO_2-treated BC are not considered to be ice nucleation active. The initial and constantly increasing proportion of the lattice disorders in BC might account for the inactivity. Recent studies showed that the ordering of liquid water on an ideal graphitic lattice plays an important role in the heterogeneous ice nucleation mechanism. Disorientations of the graphitic lattice disturb the interactions with liquid water and lower the INA until no INA is evident (Lupi et al., 2014; Lupi and Molinero, 2014; Bi et al., 2016).

In contrast to NO_2-treated BC, SO_2-treated BC exhibits a significant decrease in disorders after 30 minutes of treatment (G/D of 0.35). Concurrently, the INA of BC peaks to a maximum after 30 minutes of SO_2 treatment, as shown by a $T_{50,hetero}$ value of approximately -22 °C. However, continuing exposure decreases the G/D ratios in the same way as the INA. The following two mechanisms are thought to account for the sharp increase in INA and G/D ratio: (i) The uptake of oxygen with ongoing treatment indicates the adsorption of SO_2

molecules. SO_2 molecules are known to react with soot surfaces rich in aromatic C-H but poor in oxygen compounds (Zhao et al., 2017). Adsorbed SO_2 forms organo-sulfates, which can influence the particle morphology. TEM images of vapor-treated BC revealed morphology changes and agglomeration processes (see Figures 6-5 and 6-6), which are consistent with Zhao et al. (2017). These processes may increase the G/D ratio since boundaries become smoother, and therefore, surface and edge disorders are reduced. Due to the increased degree of graphitization, the INA rises, which is in agreement with Lupi et al. (2014), Lupi and Molinero (2014) and Bi et al. (2016). (ii) Organo-sulfates are also known to change the water uptake capacity of organic aerosol particles depending on the degree of sulfatization. The increase in the water uptake may increase the water-particle interface and therefore raise the INA (Schill and Tolbert, 2013; Estillore et al., 2016).

The loss of the graphitic structure with the ongoing reaction and a drop in G/D might account for the subsequent decrease in INA (back to the value of the untreated BC). The degree of graphitization seems to have a major impact on the INA and might be responsible for the stepwise rise and fall in the INA of BC. The introduction of disorders influences the ability to perform heterogeneous ice nucleation. The ordering of water molecules at the interface to perform heterogeneous ice nucleation seems to depend on the morphology and the graphitic lattice. Disorders in the lattice disturb the interactions with liquid water and therefore lower the INA of soot.

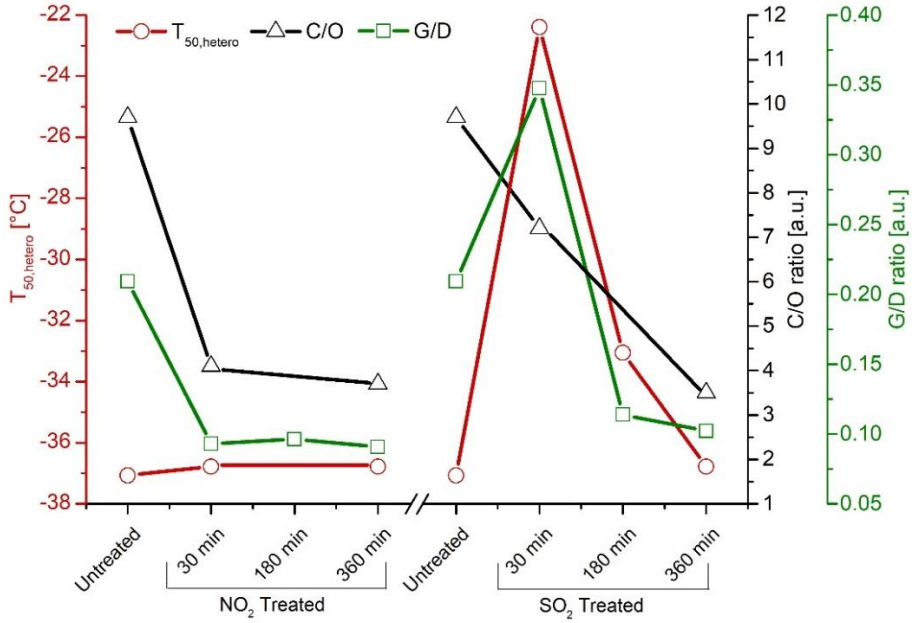

Figure 6-12 Untreated, and NO_2 and SO_2 vapor-phase-treated black carbon: Comparison of the Raman-fitted G/D band ratios (green line with square symbols) indicating the degree of graphitization. The $T_{50,hetero}$ values (red line with circular symbols) indicate the INA, and the C/O ratios (black line with triangular symbols) indicate the surface oxygen content. Freezing temperatures below -35 °C are considered as homogeneous nucleation but remain in the diagram as references.

6.3.2 Brown Carbon

The expected increase in the organic residuals in brown carbon was confirmed by the low C/O ratio of untreated BrC (7.7), which is approximately 20% less than the organic content of black carbon (9.7) (see Figure 6-13). Furthermore, successful surface reactions via gaseous treatments were confirmed by the decreasing C/O ratios with ongoing exposure.

The reaction of BrC with NO_2 and SO_2 proceeds differently. Specifically, the reaction with NO_2 occurs rapidly with 80% of the oxygen uptake occurring within the first 30 minutes resulting in a C/O ratio of 5.4, while the reaction with SO_2 occurs much slower, resulting in a higher C/O ratio of 6.7. In comparison with BC, a significantly reduced oxygen uptake of BrC during both treatments is shown. The C/O ratio of BC decreases by 6 during both treatments, while the ratio of BrC decreases by approximately 1.7. This result can be explained by the fact that BrC surfaces are rich in oxygen-containing functional groups and poor in aromatic C-H groups. These chemical surface compositions are known to reduce the kinetics of NO_2 and SO_2 adsorption (Zhang et al., 2008; Han et al., 2017). However, XPS measurements did not reveal sulfur or nitrogen, which is accounted for by the high detection limits.

Due to gaseous treatments, a loss of graphitic structure is demonstrated by two indicators. First, Raman spectroscopy revealed a drop in the G/D ratios. Second, TEM images of treated and hence oxidized BrC showed a loss of the typical onion-like soot structure, which untreated BrC images exhibited. Nevertheless, the oxidation by SO_2 generates more disorders in the lattice, resulting in a minimum G/D ratio of 0.07, even though more oxygen uptake occurs using NO_2. Within the first 30 minutes of SO_2 exposure, more disorders are generated in the lattice than after 360 minutes of NO_2 treatment.

Immersion freezing experiments showed that the INA of BrC increases stepwise with a continuation of NO_2 and SO_2 treatments. While the $T_{50,hetero}$ value of SO_2-treated BrC (-24.1 °C) reached a higher temperature than NO_2-treated BrC (-26.5 °C), just 40% of the observed droplets froze heterogeneously in the case of SO_2 exposed BrC. However, 100% of the observed droplets froze heterogeneously for NO_2-treated BrC.

Since the INA increased with exposure time and ongoing oxygen uptake, the adsorption and incorporation of oxygen-containing compounds seem to account for the substantial rise in INA, even though the degree of graphitization was lowered. The rise in polar compounds on the BrC surfaces are thought to increase the INA in two ways: (i) a rise in hydrophilicity reduces the agglomeration in an aqueous suspension and hence increases the available surface area and INA; and (ii) oxides or other polar groups on the surface of INPs are thought to offer so-called functional sites, which interact with water molecules and nucleate ice (Garten and

Head, 1964; Gorbunov and Safatov, 1994). These sites are suggested to be able to form hydrogen bonds with water molecules, leading to higher levels of INA. Both mechanisms are thought to influence the INA and must be considered to explain the INA of BrC.

The impact of the lattice order seems to be secondary since the INA goes up even though additional disorder is introduced. Nevertheless, the formation of additional polar groups also increases the hydrophilicity of soot particles and might lead to reduced agglomeration and hence increased surface area and INA, which needs to be considered. In general, longer durations of treatment lead to extended oxygen uptake and thus to more polar groups within the soot. Consequently, a further increase in the INA might be expected with ongoing exposure of over 360 minutes.

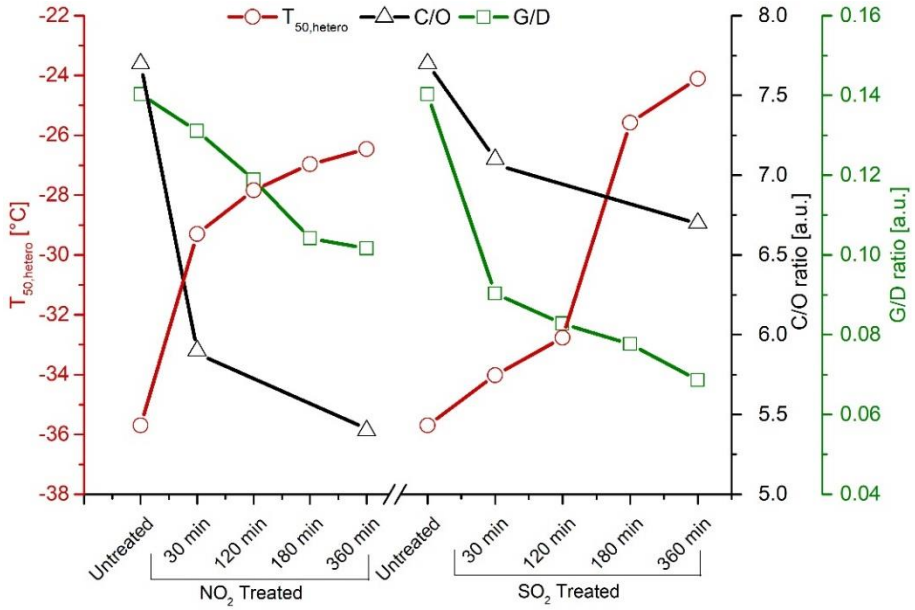

Figure 6-13 Untreated, and NO_2 and SO_2 vapor-phase-treated brown carbon: Comparison of fitted Raman G/D band ratios (green line with square symbols) indicating the degree of graphitization. The $T_{50,hetero}$ values (red line with circular symbols) indicate the INA, and the C/O ratios (black line with triangular symbols) indicate the surface oxygen content. Freezing temperature of untreated BrC (below -35 °C) is considered as homogeneous nucleation but remain in the diagram as a reference.

6.4 Summary

Two different types of soot were produced by burning a propane-air mixture using a miniCAST burner. Depending on the proportions in the mixture, soot with high (brown carbon) or low (black carbon) organic content was obtained. Soot particles in the size range of 0.1–10 µm were collected on a single stage of a modified six-stage cascade impactor on polyvinyl fluoride foils. These samples were treated with NO_2 and SO_2 in a reaction chamber. The exposure times were between 30 and 360 minutes. The untreated and treated soot samples were analyzed with respect to their ice nucleation activity via immersion freezing experiments, their composition via XPS, their microstructure via Raman spectroscopy and their particle morphology via TEM.

Expected differences in the organic residues in black and brown carbon were confirmed by elemental analysis via XPS, which showed an increased proportion of oxygen for BrC (C/O of 7.7) compared to that of BC (C/O of 9.7). Differences in the reactivity of NO_2 and SO_2 with BrC and BC, respectively, were shown by means of different gradients of C/O ratios over the duration of the gas phase reactions. While SO_2 reacts with BC evenly during the whole exposure period, NO_2 reacts almost completely (> 90%) within the first 30 minutes of treatment. However, after 360 minutes of exposure, BC reaches the same degree of surface oxygen content for both gases (C/O of approximately 3.6). In contrast, BrC showed a higher reactivity with NO_2 (C/O of 5.4) than with SO_2 (C/O of 6.7) since a higher degree of oxygen uptake was reached. The reaction of BrC with NO_2 and SO_2 showed a higher reaction rate within the first 30 minutes of exposure. Nearly 80% and 60% of the oxygen uptake were completed within the first 30 minutes of the NO_2 and SO_2 treatments, respectively.

As a consequence of the chemical treatment, additional disorders were generated in the graphitic-like lattice of BC and BrC, as shown by the link of the C/O ratios and degree of graphitization. The graphitization of BC (G/D of 0.21) decreased during the reaction with NO_2 and SO_2 to approximately 0.1, while the values of BrC (G/D of 0.14) decreased to 0.07 during SO_2 and 0.1 during NO_2 treatment.

After 30 minutes of the treatment of BC with SO_2, a considerable increase in INA was shown by a shift of freezing temperatures from below -35 °C to a $T_{ice,hetero}$ value of -22 °C. Concurrently, a significant rise in lattice order, as shown by a shift of the G/D ratio from 0.21 to 0.35, was determined. Further SO_2 treatment of BC reduced the degree of graphitization and INA.

TEM analysis revealed that agglomeration processes occurred during the reaction of BC with SO_2. The formation of organic sulfates on the surface and agglomeration processes are

suggested to lead to a reduction in the boundary and edge disorders, increasing the degree of graphitization and INA after 30 minutes of treatment. A loss of the graphitic structure with ongoing treatment led to a subsequent decrease in INA. The degree of graphitization was shown to influence the INA and accounted for the stepwise upward and downward movements of the INA of BC, which is in agreement with the calculations of Lupi et al. (2014), Lupi and Molinero (2014), Bi et al. (2016) and the laboratory work of Whale et al. (2015b). The introduction of different kinds of disorders influence the ability to perform heterogeneous ice nucleation. The ordering of water molecules at the interface to obtain heterogeneous ice nucleation depends on the graphitic lattice. Disorders in the lattice disturb the interactions with liquid water and therefore lower the INA of soot.

Both gaseous treatments of BrC steadily lowered the degree of graphitization with ongoing reaction. Simultaneously, the INA rose with increasing oxygen uptake into the surface causing higher polarity, which is in agreement with Gorbunov et al. (2001) and Brooks et al. (2014). The increase in polar compounds on BrC surfaces increase the INA in two ways: (i) a rise in hydrophilicity reduces the agglomeration in an aqueous suspension and hence increases the available surface area; and (ii) polar surface functional groups and nucleation sites attract water molecules and allow the formation of critical water clusters (Garten and Head, 1964; Gorbunov and Safatov, 1994). Both can influence the INA and must be considered to explain the INA of BrC.

In conclusion, the surface composition, degree of graphitization and agglomeration are shown to have a major impact on the INA. To determine the ice nucleating relevant feature of soot, the interplay among all factors must be taken into consideration.

7. The Ice Nucleation Activity of Cellulose

Carbonaceous aerosol particles with biological origin, such as microcrystalline cellulose particles, are known to be efficient INPs at temperatures below about -21 °C. Yet several questions, such as the nucleating feature of this type of INP, remain unanswered. The INA of four different types of cellulose and the dependence on concentration, surface modification and preparation was investigated and is presented here. Cellulose revealed an INA limited to a certain range of concentration. A lower concentration limit needs to be surpassed to reveal INA. An increase of effective water-particle interface allows INPs to trigger ice formation more effectively. On the contrary, suspensions with increased concentrations above an upper limit showed a lowered INA. An increased concentration can lead to agglomeration processes within the suspension. Particles accumulate to larger agglomerates, reducing the effective surface area and therefore the INA.

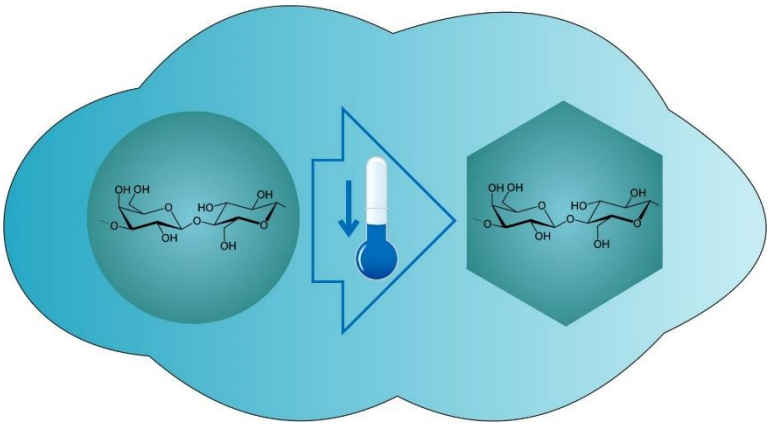

Figure 7-1 The Ice Nucleation Activity of Cellulose- graphical abstract.

To determine the impact of different welling durations, cellulose was kept suspended for an increased duration of 24 hours, before the INA was determined. The increased duration caused a shift of freezing temperatures from -24 °C to -23.2 °C. Even cellulose is hydrophilic due to its polar groups and therefore considered to suspend easily in water. An increased duration of dwelling in the suspension is necessary to fully suspend the particles and develop a maximum water-particle interface. The rise of effective water-particle interface allows INPs to trigger ice formation more effectively and increases the INA.

To determine the impact of chemical composition on the INA, cellulose sample M105 was esterified to reduce the characteristic hydroxy group. A successful esterification was confirmed by IR-spectroscopy, revealing the characteristic ester C=O stretch vibration at 1729 cm^{-1} after the treatment. The freezing spectra of untreated and esterified cellulose show a shift of the T_{50} value to lower temperatures, from -24 °C to -26.9 °C. A reduction of polar groups able to form hydrogen bonds with water molecules led to a lowered INA, which agrees with classical “chemical bonding” requirement of INPs.

7.1 Description of Materials

Natural cellulose [β(1,4)-linked D-glucose polymer] (see Figure 7-2) is a main component of a variety of biological cell walls and contributes about 50% of the dry weight of plants (Nishiyama et al., 2002; Quiroz-Castañeda and Folch-Mallol, 2013). Therefore, cellulose-containing particles are ubiquitous in the Earth's atmosphere. Field observations showed that cellulose can constantly account for more than 5% (up to 22%) by mass of the total airborne organic matter throughout the year, despite seasonal variations (Sanchez-Ochoa et al., 2007). Moreover, a concentration of atmospheric cellulose can be up to 0,4 µg m^{-3} in urban environments and is attributed to the plant debris emitted at or near ground level (Puxbaum and Tenze-Kunit, 2003).

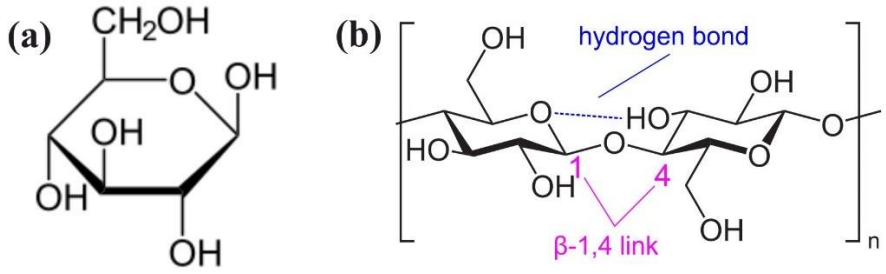

Figure 7-2 Structural formula of (a) D- glucose and (b) β(1,4)-linked D-glucose units forming cellobiose and stabilizing via hydrogen bonds.

Four different microcrystalline cellulose powders, purchased from JRS Pharma GMBH & CO. KG, were investigated. Their description, including commercial name, batch number, specific surface area and other physicochemical properties, is given in Table 7-1.

Table 7-1 List of investigated cellulose samples, including their batch numbers and physicochemical properties.

Characteristics	Sample			
Name	VIVAPURR 105	VIVAPURR 101	VIVAPURR 102	ARBOCEL M80
Batch number	6610540508	6610138133	5610241006	72813130330
Specific surface area [m2/g]	3.1375	1.4697	1.1898	0.9756
Degree of polymerization	224	238	243	1158
Stability of suspension	stabile	stabile	stabile	
Conductivity [µS/cm]	30	19	26	
Solubility in ether [%]	0.0	0.01	0.01	0.02
Solubility in water [%]	0.13	0.10	0.11	0.2
Heavy metals [ppm]	< 10	< 10	< 10	< 10
pH	6	6.3	6.2	5.4
Concentration of aerobic microorganism [cfu/g]	103	102	102	< 103
Concentration of mold and yeast particles	102	20	20	< 102
E. coli, Pseudomonas aeruginosa, Staph aureus	non	non	non	non
Salmonella	non	non	non	non
Density [g/ml]	0,16	0,28	0,29	218
Particle size > 32µm [%]	1	58	78	41

7.2 Results and Discussion

7.2.1 Concentration Dependence

To determine the concentration dependence on the INA of cellulose, suspensions with concentrations between 0.4 and 4.1 g/L were prepared. The freezing spectrum of each suspension is shown in Figures 7-3 to 7-6. A lower limit of concentration needed to be exceeded before cellulose nucleates ice. Furthermore, when surpassing an upper limit of concentration, no heterogeneous ice nucleation took place. The lower concentration limit of cellulose M80, M101 and M105 lied between 0.4 and 0.5 g/L, while M102 revealed a decreased limit of 0.9 g/L. The upper limit of M80 and M102 lied at 4.0 g/L, while M101 and M105 revealed a significantly decreased upper limit of 2.6 and 2.0 g/L.

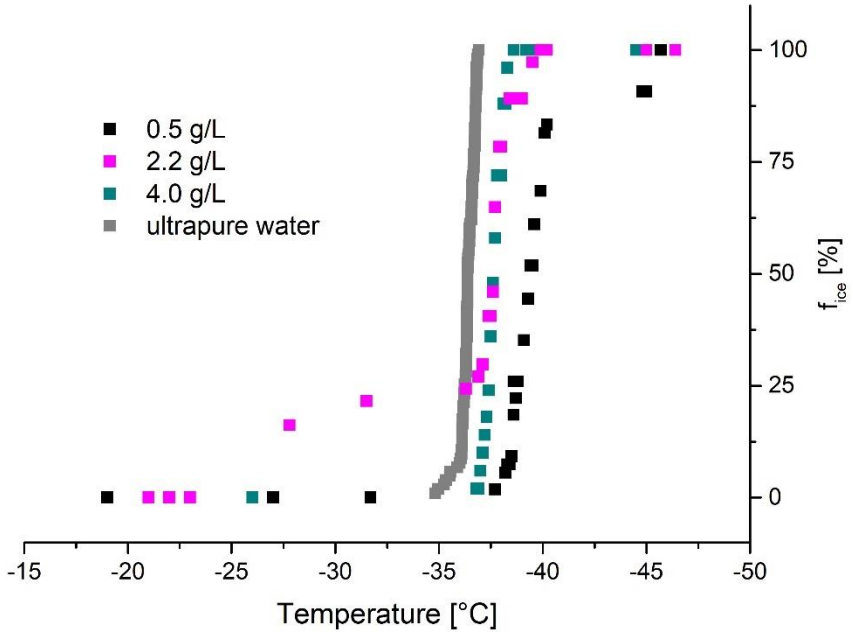

Figure 7-3 Freezing spectra of cellulose sample M80 at different concentrations and ultrapure water. The cellulose suspensions with a concentration of 0.5 g/L (black squares) and 4.0 g/L (green squares) do not show INA. The suspension of 2.2 g/L (pink squares) partially freezes at temperatures higher than -37 °C and is therefore considered to be ice nucleation active.

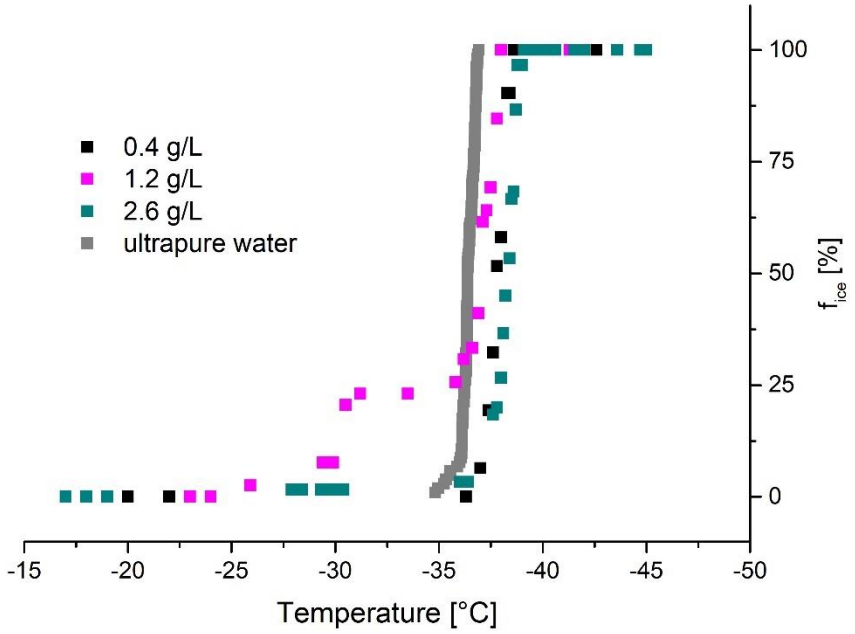

Figure 7-4 Freezing spectra of cellulose sample M101 at different concentrations and ultrapure water. The cellulose suspensions with a concentration of 0.4 g/L (black squares) and 2.6 g/L (green squares) do not show INA. The suspension of 1.2 g/L (pink squares) partially freezes at temperatures higher than -37 °C and is therefore considered to be ice nucleation active.

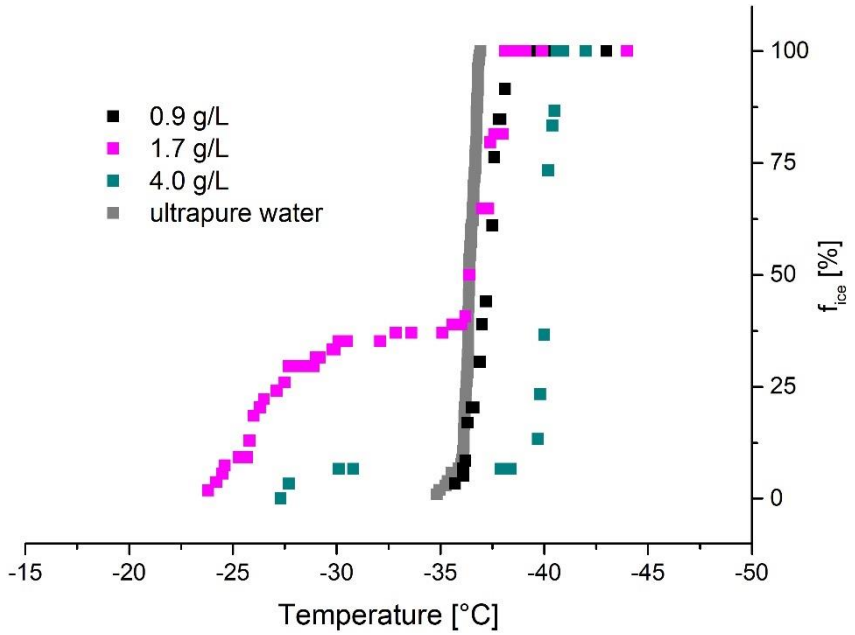

Figure 7-5 Freezing spectra of cellulose sample M102 at different concentrations and ultrapure water. The cellulose suspensions with a concentration of 0.9 g/L (black squares) and 4.0 g/L (green squares) do not show INA. The suspension of 1.7 g/L (pink squares) partially freezes at temperatures higher than -37 °C and is therefore considered to be ice nucleation active.

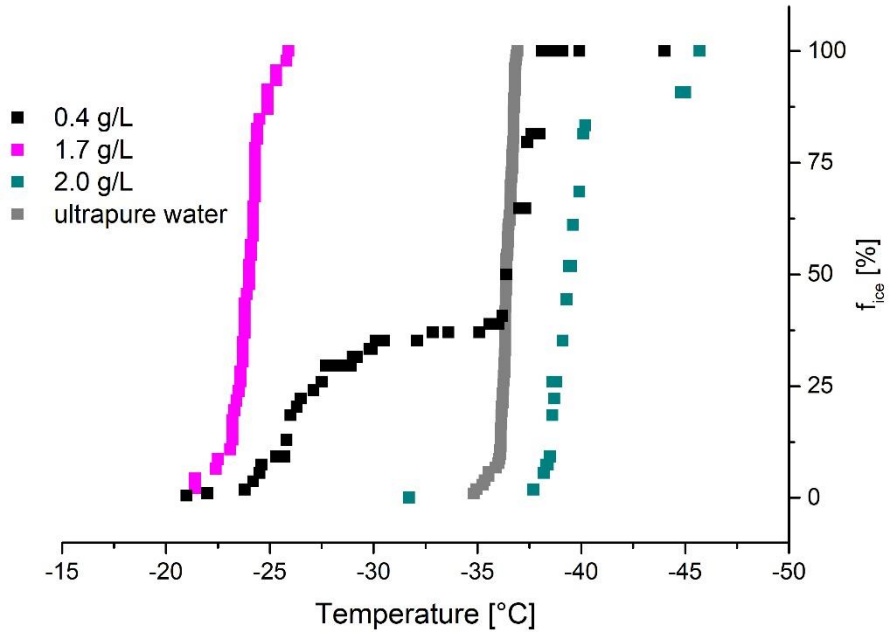

Figure 7-6 Freezing spectra of cellulose sample M105 at different concentrations and ultrapure water. The cellulose suspension with a concentration of 2.0 g/L (green squares) does not show INA. The suspension of 0.4 g/L (black squares) freezes partially and the suspension of 1.7 g/L (pink squares) completely at temperatures higher than -37 °C and are therefore considered to be ice nucleation active.

7.2.2 Preparation Dependence

For freezing experiments, the time delay between the preparation of suspension and the measurement is intentionally kept short to minimize possible altering processes of the INP. To determine the impact of different welling times of suspended INPs in ultrapure water, the cellulose sample M105 was kept suspended for 24 hours before the INA was determined. A comparison of freezing spectra with freshly suspended cellulose and welled cellulose for 24 hours is shown in Figure 7-7. An increased duration of dwelling caused a shift of the T_{50} value to higher temperatures, from -24 °C to -23.2 °C.

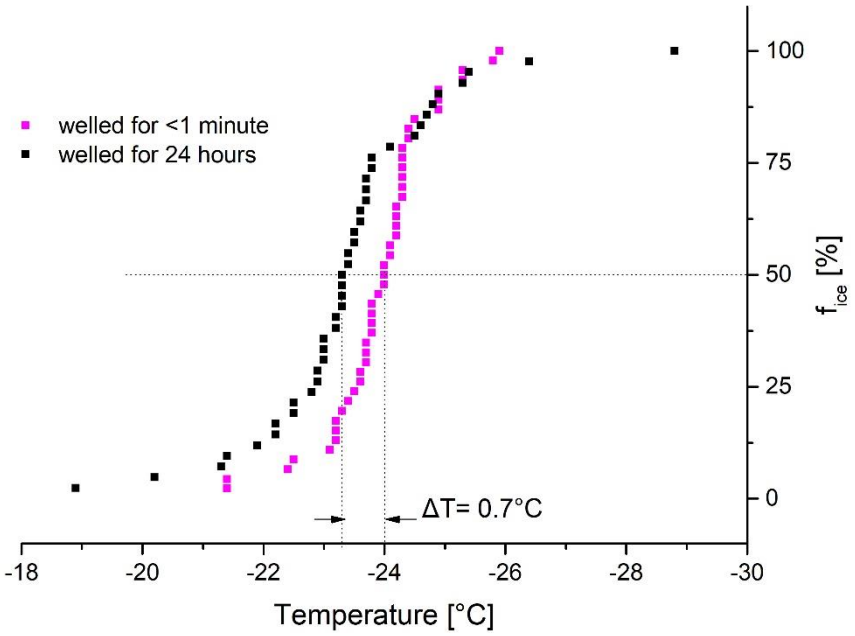

Figure 7-7 Freezing spectra of cellulose M105 (concentration of 1.7 g/L) with welling durations of <1 minute and 24 hours. The T_{50} value of the sample with longer welling duration shifts for 0.7 °C to higher temperatures.

7.2.3 Chemical Composition Dependence

The interplay between chemical groups on the surface of an INP and water molecules can have a major impact on the INA (Pruppacher and Klett, 1997). Polar groups like the hydroxy groups of cellulose are assumed to support ice nucleation by forming hydrogen bonds with water molecules and stabilizing the ice cluster. To determine the impact of chemical composition on the INA of cellulose, cellulose M105 was esterified to reduce the characteristic hydroxy group. For this purpose, 5 g of cellulose M105 was dried for 24 hours under vacuum, diluted with acidic acid until a concentration of 18M was reached and cooked under reflux for 2 hours. Hydrochloric acid was added as a catalyzer. The esterified cellulose was repeatedly washed with deionized water and centrifugated to remove remaining solvents. The final dehydration took place under vacuum at 80 °C (Braun et al., 2012). To confirm the esterification, IR spectroscopy was performed. The evident characteristic ester C=O stretch vibration at 1729 cm^{-1} (see Figure 7-8) confirms a successful esterification (Silverstein et al., 1981). Freezing spectra shown in Figure 7-9 reveal a shift of the T_{50} value to lower temperatures, from -24 °C to -26.9 °C, after the esterification.

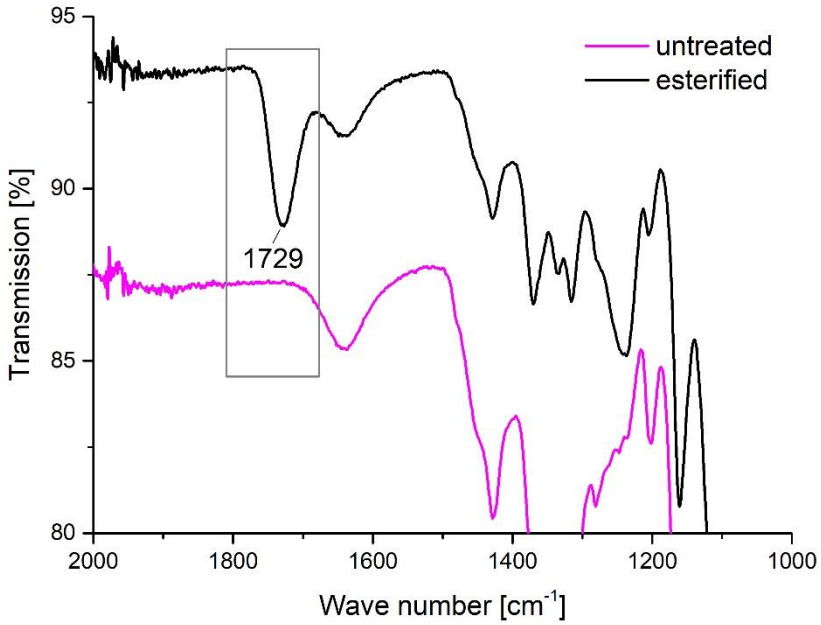

Figure 7-8 IR spectra of untreated and esterified cellulose M105. The characteristic C=O stretch vibration band for ester at 1729 cm^{-1} confirms a successful esterification (Silverstein et al., 1981).

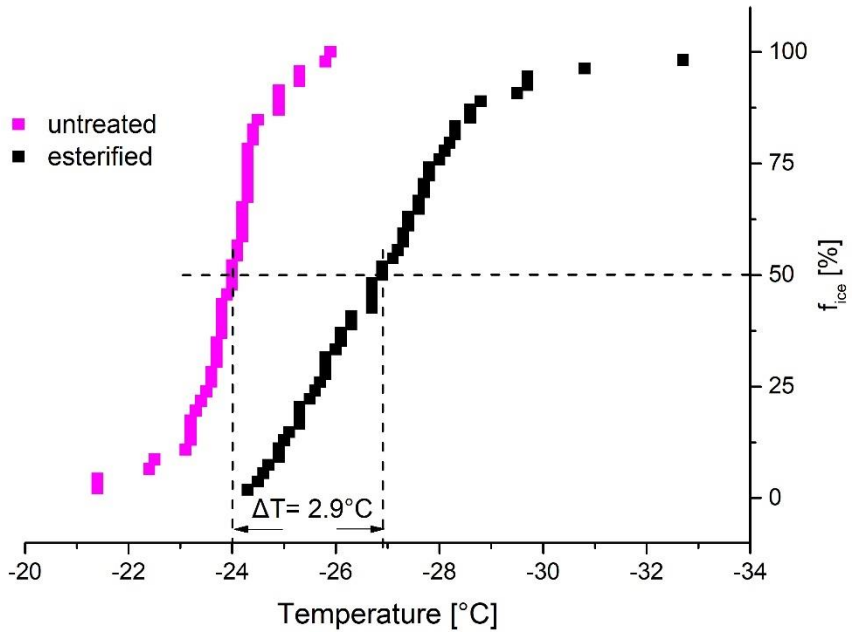

Figure 7-9 Freezing spectra of cellulose M105 (concentration of 1.7 g/L) untreated and esterified. The T_{50} value of esterified cellulose shifts for 2.9 °C to lower temperatures.

7.3 Summary

The impact of suspension preparation, suspension concentration and chemical composition on the INA of microcrystalline cellulose was investigated. Freezing spectra of all cellulose samples revealed an upper and lower concentration limit of INA (see Figure 7-3 to 7-6). A lower concentration limit needs to be surpassed in order that cellulose reveals INA. Suspensions below this concentration revealed freezing temperatures below -37 °C and are therefore considered to be inactive. However, the concentration varies within the samples investigated. The lower concentration limit of cellulose M80, M101 and M105 lies between 0.4 and 0.5 g/L, while M102 revealed a decreased limit of 0.9 g/L. The specific surface area is known to have a major impact on the INA (Pruppacher and Klett, 1997). Suspensions of INPs with an increased surface area are known to show an increased INA compared to suspension of INPs with a lower surface area. The rise of effective water-particle interface allows INPs to trigger ice formation more effectively and increases the INA. Furthermore, an upper concentration limit for the INA of cellulose was revealed by the freezing spectra. Suspensions with increased concentrations above this limit showed a lowered INA. An increased concentration can lead to agglomeration processes within the suspension. Particles accumulate to larger agglomerates, reducing the effective surface area and therefore the INA.

To determine the impact of different welling durations on the INA of cellulose, sample M105 was kept suspended for 24 hours before the INA was determined. The increased dwelling duration caused a shift of freezing temperatures. The T_{50} value of cellulose longer in suspension shifted to higher temperatures, from -24 °C to -23.2 °C, suggesting an increased INA. Even though cellulose is hydrophilic due to its polar groups and therefore considered to suspend easily in water, an increased duration of dwelling in the suspension is necessary to fully suspend the particles and develop a maximum water-particle interface.

Polar groups like the hydroxy groups of cellulose are assumed to support ice nucleation by forming hydrogen bonds with water molecules and stabilizing the ice cluster. To determine the impact of chemical composition on the INA of cellulose, cellulose M105 was esterified according to Braun et al. (2012) to reduce the characteristic hydroxy group. A successful esterification was confirmed by IR-spectroscopy, revealing the characteristic ester C=O stretch vibration at 1729 cm^{-1} after the treatment. The freezing spectra of untreated and esterified cellulose M105 show a shift of the T_{50} value to lower temperatures, from -24 °C to -26.9 °C. A reduction of polar groups able to form hydrogen bonds with water molecules led to a lowered INA, which is in agreement with the classical “chemical bonding” requirement of INPs from Pruppacher and Klett (1997).

8. Outlook

The primary role of laboratory experiments should be meant to link theoretical work and real-world measurements. Their results are important for the interpretation of measurement campaigns of freezing events in the atmosphere as well as for the parametrization of theoretical calculations. This work focused on two main objectives: (i) the enhancement of immersion freezing techniques to determine INA and (ii) the investigation of carbonaceous aerosol particles. The new technique to determine the ice nucleation activity of aerosol particles in immersion freezing mode reduces the issues connected with vial-shaking droplet-freezing techniques. Furthermore, it opens the possibility to conduct refreezing experiments and to possibly distinguish between stochastic and singular nucleation in the future. A continuous enhancement and adaptation of the established techniques will improve the quality of results, reduce time necessary to perform and evaluate freezing experiments and ensure their scientific relevance.

Ice nucleating particles exhibit a variety of different and complex mechanisms when interacting with water during the freezing process. Yet knowledge of an ice nucleating feature remains unknown. Therefore, studies of proxy INPs, as shown in this work, are an effective approach to provide an answer to the question - What makes an effective INP? The investigation of similar INPs with differences in one ice nucleation relevant feature should be continued and intensified. More species with closely controlled differences need to be investigated in order to draw a firm experimental conclusion about the effect of each feature on the INA. Developed results gained by experiments of proxy INPs need to be applied to real-world INPs as soot. An ongoing response to the question of whether ice nucleating rules of proxy INPs are consistent with real-world INPs needs to be established.

The combination of different approaches, from theoretical calculations to laboratory experiments to real-world measurement campaigns, needs to be focused on. Only with an all-embracing point of view, the answers to open-ended questions in the field of ice nucleation, can be found.

9. References

Abascal, J. L. F., Sanz, E., Fernandez, R. G., and Vega, C.: A potential model for the study of ices and amorphous water: TIP4P/Ice, *Journal of Chemical Physics*, 122, 2005.

Abascal, J. L. F., and Vega, C.: A general purpose model for the condensed phases of water: TIP4P/2005, *Journal of Chemical Physics*, 123, 2005.

Abbatt, J. P. D.: Interactions of atmospheric trace gases with ice surfaces: Adsorption and reaction, *Chemical Reviews*, 103, 4783-4800, 2003.

Andreae, M. O., and Gelencser, A.: Black carbon or brown carbon? The nature of light-absorbing carbonaceous aerosols, *Atmospheric Chemistry and Physics*, 6, 3131-3148, 2006.

Atkinson, J. D., Murray, B. J., Woodhouse, M. T., Whale, T. F., Baustian, K. J., Carslaw, K. S., Dobbie, S., O'Sullivan, D., and Malkin, T. L.: The importance of feldspar for ice nucleation by mineral dust in mixed-phase clouds, *Nature*, 500, 491-491, 2013.

Augustin, S., Wex, H., Niedermeier, D., Pummer, B., Grothe, H., Hartmann, S., Tomsche, L., Clauss, T., Voigtlander, J., Ignatius, K., and Stratmann, F.: Immersion freezing of birch pollen washing water, *Atmospheric Chemistry and Physics*, 13, 10989-11003, 2013.

Auliciems, A., and Burton, I.: Trends in Smoke Concentrations before and after Clean Air Act of 1956, *Atmospheric Environment*, 7, 1063-1070, 1973.

Beamson, G., and Briggs, D.: High Resolution XPS of Organic Polymers - The Scienta ESCA300 Database, Wiley, Appendices 3.1 and 3.2. pp., 1992.

Behera, S. N., and Sharma, M.: Investigating the potential role of ammonia in ion chemistry of fine particulate matter formation for an urban environment, *Science of the Total Environment*, 408, 3569-3575, 2010.

Berner, A.: About the separation property, of impactor stage with nonstationary flow., 327- 358, 1976.

Bi, Y. F., Cabriolu, R., and Li, T. S.: Heterogeneous Ice Nucleation Controlled by the Coupling of Surface Crystallinity and Surface Hydrophilicity, *Journal of Physical Chemistry C*, 120, 1507-1514, 2016.

Bianco, V., Franzese, G., Dellago, C., and Coluzza, I.: Role of Water in the Selection of Stable Proteins at Ambient and Extreme Thermodynamic Conditions, *Physical Review X*, 7, 2017.

Biggs, C. I., Packer, C., Hindmarsh, S., Walker, M., Wilson, N. R., Rourke, J. P., and Gibson, M. I.: Impact of sequential surface-modification of graphene oxide on ice nucleation, *Physical chemistry chemical physics : PCCP*, 19, 21929-21932, 10.1039/c7cp03219f, 2017.

Bockhorn, H.: Soot formation in combustion: mechanisms and models, Springer, Berlin, 1994.

Bogdan, A.: Thermodynamics of the curvature effect on ice surface tension and nucleation theory, *Journal of Chemical Physics*, 106, 1921-1929, 1997.

Böhm, H. P., Clauss, A., Fischer, G. O., and Hofmann, U.: Das Adsorptionsverhalten sehr dünner Kohlenstoff-Folien, *Zeitschrift für anorganische und allgemeine Chemie*, 316, 119-127, 10.1002/zaac.19623160303, 1962.

Böhm, H. P.: Graphene-How a Laboratory Curiosity Suddenly Became Extremely Interesting, *Angewandte Chemie-International Edition*, 49, 9332-9335, 2010.

Braun, B., Dorgan, J. R., and Hollingsworth, L. O.: Supra-Molecular EcoBioNanocomposites Based on Polylactide and Cellulosic Nanowhiskers: Synthesis and Properties, *Biomacromolecules*, 13, 2013-2019, 2012.

Brimblecombe, P.: Air Composition and Chemistry, Cambridge University Press, Cambridge, UK, 1986.

Broadley, S. L., Murray, B. J., Herbert, R. J., Atkinson, J. D., Dobbie, S., Malkin, T. L., Condliffe, E., and Neve, L.: Immersion mode heterogeneous ice nucleation by an illite rich powder representative of atmospheric mineral dust, *Atmospheric Chemistry and Physics*, 12, 287-307, 2012.

Brooks, S. D., Suter, K., and Olivarez, L.: Effects of Chemical Aging on the Ice Nucleation Activity of Soot and Polycyclic Aromatic Hydrocarbon Aerosols, *Journal of Physical Chemistry A*, 118, 10036-10047, 2014.

Brunauer, S., Emmett, P. H., and Teller, E.: Adsorption of Gases in Multimolecular Layers, *Journal of the American Chemical Society*, 60, 309-319, 10.1021/ja01269a023, 1938.

Budke, C., and Koop, T.: BINARY: an optical freezing array for assessing temperature and time dependence of heterogeneous ice nucleation, *Atmospheric Measurement Techniques*, 8, 689-703, 2015.

Bunbury, H. M.: Die Chemie des Holzes., Springer, Berlin, Heidelberg, 1925.

Butler, G. W., and Bailey, R. W.: Chemistry and Biochemistry of Herbage, 1, Academic Press, New York, 1973.

Campbell, J. M., Meldrum, F. C., and Christenson, H. K.: Is Ice Nucleation from Supercooled Water Insensitive to Surface Roughness?, *Journal of Physical Chemistry C*, 119, 1164-1169, 2015.

Chakrabarti, M. H., Low, C. T. J., Brandon, N. P., Yufit, V., Hashim, M. A., Irfan, M. F., Akhtar, J., Ruiz-Trejo, E., and Hussain, M. A.: Progress in the electrochemical modification of graphene-based materials and their applications, *Electrochimica Acta*, 107, 425-440, 2013.

Chang, S. G., and Novakov, T.: Formation of Pollution Particulate Nitrogen-Compounds by NO-Soot and NH3-Soot Gas-Particle Surface-Reactions, *Atmospheric Environment*, 9, 495-504, 1975.

Chen, J. P., Hazra, A., and Levin, Z.: Atmospheric Chemistry and Physics 8, 2008.

Chou, C., Kanji, Z. A., Stetzer, O., Tritscher, T., Chirico, R., Heringa, M. F., Weingartner, E., Prevot, A. S. H., Baltensperger, U., and Lohmann, U.: Effect of photochemical ageing on the ice nucleation properties of diesel and wood burning particles, *Atmospheric Chemistry and Physics*, 13, 761-772, 2013.

Chughtai, A. R., Brooks, M. E., and Smith, D. M.: Hydration of black carbon, *Journal of Geophysical Research-Atmospheres*, 101, 19505-19514, 1996.

Colthup, N., Daly, L. H., and Wiberley, S. E.: Introduction to Infrared and Raman Spectroscopy, 3 ed., Academic Press, London, 1990.

Coluzza, I., Creamean, J., Rossi, M. J., Wex, H., Alpert, P. A., Bianco, V., Boose, Y., Dellago, C., Felgitsch, L., Frohlich-Nowoisky, J., Herrmann, H., Jungblut, S., Kanji, Z. A., Menzl, G., Moffett, B., Moritz, C., Mutzel, A., Poschl, U., Schauperl, M., Scheel, J., Stopelli, E., Stratmann, F., Grothe, H., and Schmale, D. G.: Perspectives on the Future of Ice Nucleation Research: Research Needs and Unanswered Questions Identified from Two International Workshops, *Atmosphere*, 8, 2017.

Connolly, P. J., Mohler, O., Field, P. R., Saathoff, H., Burgess, R., Choularton, T., and Gallagher, M.: Studies of heterogeneous freezing by three different desert dust samples, *Atmospheric Chemistry and Physics*, 9, 2805-2824, 2009.

Cooper, D. R., D'Anjou, B., Ghattamaneni, N., Harack, B., Hilke, M., Horth, A., Majlis, N., Massicotte, M., Vandsburger, L., Whiteway, E., and Yu, V.: Experimental Review of Graphene, *ISRN Condensed Matter Physics*, 2012, 56, 10.5402/2012/501686, 2012.

Cox, S. J., Kathmann, S. M., Purton, J. A., Gillan, M. J., and Michaelides, A.: Non-hexagonal ice at hexagonal surfaces: the role of lattice mismatch, *Physical Chemistry Chemical Physics*, 14, 7944-7949, 2012.

Crawford, I., Mohler, O., Schnaiter, M., Saathoff, H., Liu, D., McMeeking, G., Linke, C., Flynn, M., Bower, K. N., Connolly, P. J., Gallagher, M. W., and Coe, H.: Studies of propane flame soot acting as heterogeneous ice nuclei in conjunction with single particle soot photometer measurements, *Atmospheric Chemistry and Physics*, 11, 9549-9561, 2011.

Cziczo, D. J., Ladino, L., Boose, Y., Kanji, Z. A., Kupiszewski, P., Lance, S., Mertes, S., and Wex, H.: Measurements of Ice Nucleating Particles and Ice Residuals, *Meteorological Monographs*, 58, 8.1-8.13, 10.1175/amsmonographs-d-16-0008.1, 2017.

Deguillaume, L., Leriche, M., Amato, P., Ariya, P. A., Delort, A. M., Poschl, U., Chaumerliac, N., Bauer, H., Flossmann, A. I., and Morris, C. E.: Microbiology and atmospheric processes: chemical interactions of primary biological aerosols, *Biogeosciences*, 5, 1073-1084, 2008.

DeMott, P. J.: An Exploratory-Study of Ice Nucleation by Soot Aerosols, *Journal of Applied Meteorology*, 29, 1072-1079, 1990.

Demott, P. J.: Quantitative Descriptions of Ice Formation Mechanisms of Silver Iodide-Type Aerosols, *Atmospheric Research*, 38, 63-99, 1995.

DeMott, P. J., Rogers, D. C., and Kreidenweis, S. M.: The susceptibility of ice formation in upper tropospheric clouds to insoluble aerosol components, *Journal of Geophysical Research-Atmospheres*, 102, 19575-19584, 1997.

DeMott, P. J., Chen, Y., Kreidenweis, S. M., Rogers, D. C., and Sherman, D. E.: Ice formation by black carbon particles, *Geophysical Research Letters*, 26, 2429-2432, 1999.

DeMott, P. J.: Laboratory studies of cirrus cloud processes, in Cirrus, Oxford Univ. Press, New York, 102- 136 pp., 2002.

DeMott, P. J., Prenni, A. J., Liu, X., Kreidenweis, S. M., Petters, M. D., Twohy, C. H., Richardson, M. S., Eidhammer, T., and Rogers, D. C.: Predicting global atmospheric ice nuclei distributions and their impacts on climate, *Proc Natl Acad Sci U S A*, 107, 11217-11222, 2010.

Denffer, D.: Lehrbuch der Botanik, Gustav
Fischer Verlag, Frankfurt/Main, 1978.

Diehl, K., and Mitra, S. K.: A laboratory study of the effects of a kerosene-burner exhaust on ice nucleation and the evaporation rate of ice crystals, *Atmospheric Environment*, 32, 3145-3151, 1998.

Dippel, B., and Heintzenberg, J.: Soot characterization in atmospheric particles from different sources by NIR FT Raman spectroscopy, 1999.

Dippel, B., Jander, H., and Heintzenberg, J.: NIR FT Raman spectroscopic study of flame soot, *Physical Chemistry Chemical Physics*, 1, 4707-4712, 1999.

Dreischmeier, K., Budke, C., Wiehemeier, L., Kottke, T., and Koop, T.: Boreal pollen contain ice-nucleating as well as ice-binding 'antifreeze' polysaccharides, *Scientific Reports*, 7, 2017.

Dymarska, M., Murray, B. J., Sun, L. M., Eastwood, M. L., Knopf, D. A., and Bertram, A. K.: Deposition ice nucleation on soot at temperatures relevant for the lower troposphere, *Journal of Geophysical Research-Atmospheres*, 111, 2006.

Edwards, G. R., Evans, L. F., and Lamer, V. K.: Ice Nucleation by Monodisperse Silver Iodide Particles, *Journal of Colloid Science*, 17, 749-758, 1962.

Estillore, A. D., Hettiyadura, A. P. S., Qin, Z., Leckrone, E., Wombacher, B., Humphry, T., Stone, E. A., and Grassian, V. H.: Water Uptake and Hygroscopic Growth of Organosulfate Aerosol, *Environmental Science & Technology*, 50, 4259-4268, 2016.

Ferrari, A. C., and Basko, D. M.: Raman spectroscopy as a versatile tool for studying the properties of graphene, *Nature Nanotechnology*, 8, 235-246, 2013.

Friedman, B., Kulkarni, G., Beranek, J., Zelenyuk, A., Thornton, J. A., and Cziczo, D. J.: Ice nucleation and droplet formation by bare and coated soot particles, *Journal of Geophysical Research-Atmospheres*, 116, 2011.

Gao, W., Alemany, L. B., Ci, L. J., and Ajayan, P. M.: New insights into the structure and reduction of graphite oxide, *Nature Chemistry*, 1, 403-408, 2009.

Garten, V. A., and Head, R. B.: Carbon Particles + Ice Nucleation, *Nature*, 201, 1091, 1964.

Gierens, K.: On the transition between heterogeneous and homogeneous freezing, *Atmospheric Chemistry and Physics*, 3, 437-446, 2003.

Gorbunov, B., and Safatov, A.: In-Situ Measurements of the Ice-Forming Activity of Metal-Oxide Aerosols with Controlled Amounts of Surface-Active Groups, *Journal of Aerosol Science*, 25, 673-682, 1994.

Gorbunov, B., Baklanov, A., Kakutkina, N., Windsor, H. L., and Toumi, R.: Ice nucleation on soot particles, *Journal of Aerosol Science*, 32, 199-215, 2001.

Gray, C. A., and Muranko, H.: Studies of Robustness of Industrial Aciniform Aggregates and Agglomerates—Carbon Black and Amorphous Silicas: A Review Amplified by New Data, *Journal of Occupational and Environmental Medicine*, 48, 1279-1290, 10.1097/01.jom.0000251477.40643.2a, 2006.

Gruber, T., Zerda, T. W., and Gerspacher, M.: Raman Studies of Heat-Treated Carbon-Blacks, *Carbon*, 32, 1377-1382, 1994.

Han, C., Liu, Y. C., and He, H.: Heterogeneous reaction of NO2 with soot at different relative humidity, *Environmental Science and Pollution Research*, 24, 21248-21255, 2017.

Hartmann, S., Wex, H., Clauss, T., Augustin-Bauditz, S., Niedermeier, D., Rosch, M., and Stratmann, F.: Immersion Freezing of Kaolinite: Scaling with Particle Surface Area, *Journal of the Atmospheric Sciences*, 73, 263-278, 2016.

Hauptmann, A., Handle, K. F., Baloh, P., Grothe, H., and Loerting, T.: Does the emulsification procedure influence freezing and thawing of aqueous droplets?, *The Journal of Chemical Physics*, 145, 211923, 10.1063/1.4965434, 2016.

Häusler, T., Gebhardt, P., Iglesias, D., Rameshan, C., Marchesan, S., Eder , D., and Grothe, H.: The Ice Nucleation Activity of Graphene and Graphene Oxides, *The Journal of Physical Chemistry C*, 122, 8182-8190, 10.1021/acs.jpcc.7b10675, 2018a.

Häusler, T., Witek, L., Felgitsch, L., Hitzenberger, R., and Grothe, H.: Freezing on a Chip–A New Approach to Determine Heterogeneous Ice Nucleation of Micrometer-Sized Water Droplets, *Atmosphere*, 9, 140, 10.3390/atmos9040140, 2018b.

Häusler, T., Haselmann, G., Haller, T., Eder, D., Hitzenberger, R., and Grothe, H.: The Ice Nucleation Activity of Black and Brown Soot Aged by Exposure to NO_2 and SO_2, *Journal of Geophysical Research-Atmospheres*, submitted 2018.

Haynes, W. M.: CRC Handbook of Chemistry and Physics, 84th Edition ed., CRC Press, 2004.

Heidenreich, R. D., Hess, W. M., and Ban, L. L.: A test object and criteria for high resolution electron microscopy, *Journal of Applied Crystallography*, 1, 1-19, doi:10.1107/S0021889868004930, 1968.

Heintzenberg, J.: Fine particles in the global troposphere A review, *Tellus Series B-Chemical and Physical Meteorology*, 41, 149-160, 1989.

Hiranuma, N., Mohler, O., Yamashita, K., Tajiri, T., Saito, A., Kiselev, A., Hoffmann, N., Hoose, C., Jantsch, E., Koop, T., and Murakami, M.: Ice nucleation by cellulose and its potential contribution to ice formation in clouds, *Nature Geoscience*, 8, 273-277, 2015.

Holton, J. R., and Gettelman, A.: Horizontal transport and the dehydration of the stratosphere, *Geophysical Research Letters*, 28, 2799-2802, 2001.

Hoose, C., and Möhler, O.: Heterogeneous ice nucleation on atmospheric aerosols: a review of results from laboratory experiments, *Atmospheric Chemistry and Physics*, 12, 9817-9854, 2012.

Hu, C., Sedghi, S., Silvestre-Albero, A., Andersson, G. G., Sharma, A., Pendleton, P., Rodriguez-Reinoso, F., Kaneko, K., and Biggs, M. J.: Raman spectroscopy study of the

transformation of the carbonaceous skeleton of a polymer-based nanoporous carbon along the thermal annealing pathway, *Carbon*, 85, 147-158, 2015.

Huang, J. F., and Bartell, L. S.: Kinetics of Homogeneous Nucleation in the Freezing of Large Water Clusters, *Journal of Physical Chemistry*, 99, 3924-3931, 1995.

Iannone, R., Chernoff, D. I., Pringle, A., Martin, S. T., and Bertram, A. K.: The ice nucleation ability of one of the most abundant types of fungal spores found in the atmosphere, *Atmospheric Chemistry and Physics*, 11, 1191-1201, 2011.

Ivleva, N. P., Niessner, R., and Panne, U.: Characterization and discrimination of pollen by Raman microscopy, *Analytical and Bioanalytical Chemistry*, 381, 261-267, 2005.

Ivleva, N. P., Messerer, A., Yang, X., Niessner, R., and Poschl, U.: Raman microspectroscopic analysis of changes in the chemical structure and reactivity of soot in a diesel exhaust aftertreatment model system, *Environmental Science & Technology*, 41, 3702-3707, 2007.

Johnson, D. W., Dobson, B. P., and Coleman, K. S.: A manufacturing perspective on graphene dispersions, *Current Opinion in Colloid & Interface Science*, 20, 367-382, 2015.

Kanji, Z. A., Welti, A., Chou, C., Stetzer, O., and Lohmann, U.: Laboratory studies of immersion and deposition mode ice nucleation of ozone aged mineral dust particles, *Atmospheric Chemistry and Physics*, 13, 9097-9118, 2013.

Kanji, Z. A., Ladino, L. A., Wex, H., Boose, Y., Burkert-Kohn, M., Cziczo, D. J., and Krämer, M.: Overview of Ice Nucleating Particles, *Meteorological Monographs*, 58, 1.1-1.33, 10.1175/amsmonographs-d-16-0006.1, 2017.

Kärcher, B., and Lohmann, U.: A parameterization of cirrus cloud formation: Heterogeneous freezing, *Journal of Geophysical Research-Atmospheres*, 108, 4402, 2003.

Kärcher, B., Mohler, O., DeMott, P. J., Pechtl, S., and Yu, F.: Insights into the role of soot aerosols in cirrus cloud formation, *Atmospheric Chemistry and Physics*, 7, 4203-4227, 2007.

Kiehl, J. T., and Trenberth, K. E.: Earth's annual global mean energy budget, *Bulletin of the American Meteorological Society*, 78, 197-208, 1997.

Kim, J., Bauer, H., Dobovicnik, T., Hitzenberger, R., Lottin, D., Ferry, D., and Petzold, A.: Assessing Optical Properties and Refractive Index of Combustion Aerosol Particles Through Combined Experimental and Modeling Studies, *Aerosol Science and Technology*, 49, 340-350, 2015.

Knauer, M., Schuster, M. E., Su, D. S., Schlogl, R., Niessner, R., and Ivleva, N. P.: Soot Structure and Reactivity Analysis by Raman Microspectroscopy, Temperature-Programmed Oxidation, and High-Resolution Transmission Electron Microscopy, *Journal of Physical Chemistry A*, 113, 13871-13880, 2009.

Knopf, D. A., Wang, B., Laskin, A., Moffet, R. C., and Gilles, M. K.: Heterogeneous nucleation of ice on anthropogenic organic particles collected in Mexico City, *Geophysical Research Letters*, 37, 2010.

Konios, D., Stylianakis, M. M., Stratakis, E., and Kymakis, E.: Dispersion behaviour of graphene oxide and reduced graphene oxide, *Journal of Colloid and Interface Science*, 430, 108-112, 2014.

Korolev, A.: Limitations of the wegener-bergeron-findeisen mechanism in the evolution of mixed-phase clouds, *Journal of the Atmospheric Sciences*, 64, 3372-3375, 2007.

Kunit, M., and Puxbaum, H.: Enzymatic determination of the cellulose content of atmospheric aerosols, *Atmospheric Environment*, 30, 1233-1236, 1996.

Laskin, A., Laskin, J., and Nizkorodov, S. A.: Chemistry of Atmospheric Brown Carbon, *Chemical Reviews*, 115, 4335-4382, 10.1021/cr5006167, 2015.

Levine, J.: Statistical Explanation of Spontaneous Freezing of Water Droplets, *National Advisory Committee for Aeronautics*, 1950.

Levy, L., Chaudhuri, I. S., Krueger, N., and McCunney, R. J.: Does Carbon Black Disaggregate in Lung Fluid? A Critical Assessment, *Chemical Research in Toxicology*, 25, 2001-2006, 10.1021/tx300160z, 2012.

Li, K. Y., Xu, S., Chen, J., Zhang, Q. L., Zhang, Y. F., Cui, D. P., Zhou, X., Wang, J. J., and Song, Y. L.: Viscosity of interfacial water regulates ice nucleation, *Applied Physics Letters*, 104, 2014.

Liou, K. N.: Influence of Cirrus Clouds on Weather and Climate Processes - a Global Perspective, *Monthly Weather Review*, 114, 1167-1199, 1986.

Liu, J. K., Li, Q. Q., Zou, Y., Qian, Q. K., Jin, Y. H., Li, G. H., Jiang, K. L., and Fan, S. S.: The Dependence of Graphene Raman D-band on Carrier Density, *Nano Letters*, 13, 6170-6175, 2013.

Lohmann, U.: A glaciation indirect aerosol effect caused by soot aerosols, *Geophysical Research Letters*, 29, 2002.

Lohmann, U., and Feichter, J.: Global indirect aerosol effects: a review, *Atmospheric Chemistry and Physics*, 5, 715-737, 2005.

Long, C. M., Nascarella, M. A., and Valberg, P. A.: Carbon black vs. black carbon and other airborne materials containing elemental carbon: Physical and chemical distinctions, *Environmental Pollution*, 181, 271-286, https://doi.org/10.1016/j.envpol.2013.06.009, 2013.

Lupi, L., Hudait, A., and Molinero, V.: Heterogeneous Nucleation of Ice on Carbon Surfaces, *Journal of the American Chemical Society*, 136, 3156-3164, 2014.

Lupi, L., and Molinero, V.: Does Hydrophilicity of Carbon Particles Improve Their Ice Nucleation Ability?, *Journal of Physical Chemistry A*, 118, 7330-7337, 2014.

Mamakos, A., Khalek, I., Giannelli, R., and Spears, M.: Characterization of Combustion Aerosol Produced by a Mini-CAST and Treated in a Catalytic Stripper, *Aerosol Science and Technology*, 47, 927-936, 2013.

Matsumoto, M., Saito, S., and Ohmine, I.: Molecular dynamics simulation of the ice nucleation and growth process leading to water freezing, *Nature*, 416, 409-413, 2002.

McCreery, R. L.: Raman Spectroscopy for Chemical Analysis, John Wiley & Sons, New York, 2000.

McCunney, R. J., Muranko, H. J., Long, C. M., Hamade, A. K., Valberg, P. A., and Morfeld, P.: Carbon black, *Patty's Toxicology*, 5, 429-453, 2012.

Mernagh, T. P., Cooney, R. P., and Johnson, R. A.: Raman-Spectra of Graphon Carbon-Black, *Carbon*, 22, 39-42, 1984.

Mie, G.: Articles on the optical characteristics of turbid tubes, especially colloidal metal solutions., *Annalen Der Physik*, 25, 377-445, 1908.

Mishchenko, M. I., Rossow, W. B., Macke, A., and Lacis, A. A.: Sensitivity of cirrus cloud albedo, bidirectional reflectance and optical thickness retrieval accuracy to ice particle shape, *Journal of Geophysical Research-Atmospheres*, 101, 16973-16985, 1996.

Möhler, O., Buttner, S., Linke, C., Schnaiter, M., Saathoff, H., Stetzer, O., Wagner, R., Kramer, M., Mangold, A., Ebert, V., and Schurath, U.: Effect of sulfuric acid coating on heterogeneous ice nucleation by soot aerosol particles, *Journal of Geophysical Research-Atmospheres*, 110, 2005a.

Möhler, O., Linke, C., Saathoff, H., Schnaiter, M., Wagner, R., Mangold, A., Kramer, M., and Schurath, U.: Ice nucleation on flame soot aerosol of different organic carbon content, *Meteorologische Zeitschrift*, 14, 477-484, 2005b.

Molinero, V., and Moore, E. B.: Water Modeled As an Intermediate Element between Carbon and Silicon, *Journal of Physical Chemistry B*, 113, 4008-4016, 2009.

Müller, J. O., Su, D. S., Wild, U., and Schlögl, R.: Bulk and surface structural investigations of diesel engine soot and carbon black, *Physical Chemistry Chemical Physics*, 9, 4018-4025, 2007.

Mullin, J. W.: Crystallization, Fourth Edition ed., Elsevier Ltd., 2001.

Murphy, D. M., and Koop, T.: Review of the vapour pressures of ice and supercooled water for atmospheric applications, *Quarterly Journal of the Royal Meteorological Society*, 131, 1539-1565, 2005.

Murray, B. J., Broadley, S., Wilson, T., and Atkinson, J.: Heterogeneous freezing of water droplets containing kaolinite particles: Time and surface area dependence, *Abstracts of Papers of the American Chemical Society*, 242, 2011.

Murray, B. J., O'Sullivan, D., Atkinson, J. D., and Webb, M. E.: Ice nucleation by particles immersed in supercooled cloud droplets, *Chemical Society Reviews*, 41, 6519-6554, 2012.

Murray, E. J., Murray, B. J., and Sivakumar, V.: Discussion on meta-stable equilibrium in unsaturated soils., *Unsaturated Soils: Advances in Geo-Engineering*, 553-558, 2008.

Niedermeier, D., Hartmann, S., Shaw, R. A., Covert, D., Mentel, T. F., Schneider, J., Poulain, L., Reitz, P., Spindler, C., Clauss, T., Kiselev, A., Hallbauer, E., Wex, H., Mildenberger, K., and Stratmann, F.: Heterogeneous freezing of droplets with immersed mineral dust particles - measurements and parameterization, *Atmospheric Chemistry and Physics*, 10, 3601-3614, 2010.

Niedermeier, D., Shaw, R. A., Hartmann, S., Wex, H., Clauss, T., Voigtlander, J., and Stratmann, F.: Heterogeneous ice nucleation: exploring the transition from stochastic to singular freezing behavior, *Atmospheric Chemistry and Physics*, 11, 8767-8775, 2011.

Nishiyama, Y., Langan, P., and Chanzy, H.: Crystal structure and hydrogen-bonding system in cellulose 1 beta from synchrotron X-ray and neutron fiber diffraction, *Journal of the American Chemical Society*, 124, 9074-9082, 2002.

Novakov, T., Chang, S. G., and Harker, A. B.: Sulfates as Pollution Particulates - Catalytic Formation on Carbon (Oot) Particles, *Science*, 186, 259-261, 1974.

Pandolfi, M., Amato, F., Reche, C., Alastuey, A., Otjes, R. P., Blom, M. J., and Querol, X.: Summer ammonia measurements in a densely populated Mediterranean city, *Atmospheric Chemistry and Physics*, 12, 7557-7575, 2012.

Pawlyta, M., and Hercman, H.: Transmission electron microscopy (TEM) as a tool for identification of combustion products: Application to black layers in speleothems, 2016.

Peckhaus, A., Kiselev, A., Hiron, T., Ebert, M., and Leisner, T.: A comparative study of K-rich and Na/Ca-rich feldspar ice-nucleating particles in a nanoliter droplet freezing assay, *Atmospheric Chemistry and Physics*, 16, 11477-11496, 2016.

Phan, N. T., Kim, K. H., Shon, Z. H., Jeon, E. C., Jung, K., and Kim, N. J.: Analysis of ammonia variation in the urban atmosphere, *Atmospheric Environment*, 65, 177-185, 2013.

Phillips, V. T. J., Donner, L. J., and Garner, S. T.: Nucleation processes in deep convection simulated by a cloud-system-resolving model with double-moment bulk microphysics, *Journal of the Atmospheric Sciences*, 64, 738-761, 2007.

Phillips, V. T. J., DeMott, P. J., and Andronache, C.: An empirical parameterization of heterogeneous ice nucleation for multiple chemical species of aerosol, *Journal of the Atmospheric Sciences*, 65, 2757-2783, 2008.

Polen, M., Lawlis, E., and Sullivan, R. C.: The unstable ice nucleation properties of Snomax (R) bacterial particles, *Journal of Geophysical Research-Atmospheres*, 121, 11666-11678, 2016.

Pope, R. M., and Fry, E. S.: Absorption spectrum (380–700 nm) of pure water. II. Integrating cavity measurements, *Applied Optics*, 36, 8710-8723, 10.1364/AO.36.008710, 1997.

Pratt, K. A., DeMott, P. J., French, J. R., Wang, Z., Westphal, D. L., Heymsfield, A. J., Twohy, C. H., Prenni, A. J., and Prather, K. A.: In situ detection of biological particles in cloud ice-crystals, *Nature Geoscience*, 2, 397-400, 2009.

Pratt, K. A., Heymsfield, A. J., Twohy, C. H., Murphy, S. M., DeMott, P. J., Hudson, J. G., Subramanian, R., Wang, Z. E., Seinfeld, J. H., and Prather, K. A.: In Situ Chemical Characterization of Aged Biomass-Burning Aerosols Impacting Cold Wave Clouds, *Journal of the Atmospheric Sciences*, 67, 2451-2468, 2010.

Prospero, J. M., Ginoux, P., Torres, O., Nicholson, S. E., and Gill, T. E.: Environmental characterization of global sources of atmospheric soil dust identified with the Nimbus 7 Total Ozone Mapping Spectrometer (TOMS) absorbing aerosol product, *Reviews of Geophysics*, 40, 2002.

Pruppacher, H. R., and Klett, J. D.: Microphysics of Clouds and Precipitation, Kluwer Academic Publishers, Dordrecht, 1997.

Pummer, B. G., Bauer, H., Bernardi, J., Bleicher, S., and Grothe, H.: Suspendable macromolecules are responsible for ice nucleation activity of birch and conifer pollen, *Atmospheric Chemistry and Physics*, 12, 2541-2550, 2012.

Pummer, B. G., Budke, C., Augustin-Bauditz, S., Niedermeier, D., Felgitsch, L., Kampf, C. J., Huber, R. G., Liedl, K. R., Loerting, T., Moschen, T., Schauperl, M., Tollinger, M., Morris, C. E., Wex, H., Grothe, H., Poschl, U., Koop, T., and Frohlich-Nowoisky, J.: Ice nucleation by water-soluble macromolecules, *Atmospheric Chemistry and Physics*, 15, 4077-4091, 2015.

Puxbaum, H., and Tenze-Kunit, M.: Size distribution and seasonal variation of atmospheric cellulose, *Atmospheric Environment*, 37, 3693-3699, 2003.

Quiroz-Castañeda, R. E., and Folch-Mallol, J. L.: Sustainable Degradation of Lignocellulosic Biomass—Techniques, Applications and Commercialization, InTech, 2013.

Ramanathan, V., Crutzen, P. J., Kiehl, J. T., and Rosenfeld, D.: Atmosphere - Aerosols, climate, and the hydrological cycle, *Science*, 294, 2119-2124, 2001.

Reicher, N., Segev, L., and Rudich, Y.: The WeIzmann Supercooled Droplets Observation on a Microarray (WISDOM) and application for ambient dust, *Atmos. Meas. Tech.*, 11, 233-248, 2018.

Richter, H., and Howard, J. B.: Formation of polycyclic aromatic hydrocarbons and their growth to soot - a review of chemical reaction pathways, *Progress in Energy and Combustion Science*, 26, 565-608, 2000.

Riechers, B., Wittbracht, F., Hutten, A., and Koop, T.: The homogeneous ice nucleation rate of water droplets produced in a microfluidic device and the role of temperature uncertainty, *Physical Chemistry Chemical Physics*, 15, 5873-5887, 2013.

Rogers, D. C., DeMott, P. J., Kreidenweis, S. M., and Chen, Y. L.: Measurements of ice nucleating aerosols during SUCCESS, *Geophysical Research Letters*, 25, 1383-1386, 1998.

Rosen, H., Hansen, A. D. A., Dod, R. L., and Novakov, T.: Soot in Urban Atmospheres - Determination by an Optical-Absorption Technique, *Science*, 208, 741-744, 1980.

Sadezky, A., Muckenhuber, H., Grothe, H., Niessner, R., and Poschl, U.: Raman micro spectroscopy of soot and related carbonaceous materials: Spectral analysis and structural information, *Carbon*, 43, 1731-1742, 2005.

Sanchez-Ochoa, A., Kasper-Giebl, A., Puxbaum, H., Gelencser, A., Legrand, M., and Pio, C.: Concentration of atmospheric cellulose: A proxy for plant debris across a west-east transect over Europe, *Journal of Geophysical Research-Atmospheres*, 112, 2007.

Sanz, E., Vega, C., Espinosa, J. R., Caballero-Bernal, R., Abascal, J. L. F., and Valeriani, C.: Homogeneous Ice Nucleation at Moderate Supercooling from Molecular Simulation, *Journal of the American Chemical Society*, 135, 15008-15017, 2013.

Schill, G. P., and Tolbert, M. A.: Heterogeneous ice nucleation on phase-separated organic-sulfate particles: effect of liquid vs. glassy coatings, *Atmospheric Chemistry and Physics*, 13, 4681-4695, 2013.

Schirmeister, T., Schmuck, C., Wich, P. R., Beyer, H., Walter, W., and Francke, W.: Organische Chemie, Stuttgart. Hirzel Verlag 2016.

Schumann, U., Ström, J., Busen, R., Baumann, R., Gierens, K., Krautstrunk, M., Schroder, F. P., and Stingl, J.: In situ observations of particles in jet aircraft exhausts and contrails for different sulfur-containing fuels, *Journal of Geophysical Research-Atmospheres*, 101, 6853-6869, 1996.

Scofield, J. H.: Hartree-Slater Subshell Photoionization Cross-Sections at 1254 and 1487ev, *Journal of Electron Spectroscopy and Related Phenomena*, 8, 129-137, 1976.

Seinfeld, J. H., and Pandis, S. N.: Atmospheric Chemistry and Physics: From Air Pollution to Climate Change, Wiley-Interscience, N. J., 1998.

Shearer, C. J., Slattery, A. D., Stapleton, A. J., Shapter, J. G., and Gibson, C. T.: Accurate thickness measurement of graphene, *Nanotechnology*, 27, 125704 (125710pp), 2016.

Shirley, D. A.: High-Resolution X-Ray Photoemission Spectrum of the Valence Bands of Gold, *Physical Review B*, 5, 4709-4714, 1972.

Shupe, M. D., and Intrieri, J. M.: Cloud radiative forcing of the Arctic surface: The influence of cloud properties, surface albedo, and solar zenith angle, *Journal of Climate*, 17, 616-628, 2004.

Silverstein, R., Bassler, G., and Morrill, T.: Spectrometric Identification of Organic Compounds., edited by: ed., t., John Wiley and Sons, New York, 1981.

Smith, M. W., Dallmeyer, I., Johnson, T. J., Brauer, C. S., McEwen, J. S., Espinal, J. F., and Garcia-Perez, M.: Structural analysis of char by Raman spectroscopy: Improving band assignments through computational calculations from first principles, *Carbon*, 100, 678-692, 2016.

Song, J. H., Alam, M., Boehman, A. L., and Kim, U.: Examination of the oxidation behavior of biodiesel soot, *Combustion and Flame*, 146, 589-604, 2006.

Stan, C. A., Schneider, G. F., Shevkoplyas, S. S., Hashimoto, M., Ibanescu, M., Wiley, B. J., and Whitesides, G. M.: A microfluidic apparatus for the study of ice nucleation in supercooled water drops, *Lab on a Chip*, 9, 2293-2305, 2009.

Stanley, R. G., and Linsken, H. F.: Pollen - Biologie, Biochemie, Gewinnung und Verwendung, URS Freund Verlag, Greifenberg-Ammersee, Deutschland, 1985.

Steiner, T.: The hydrogen bond in the solid state, *Angewandte Chemie-International Edition*, 41, 48-76, 2002.

Stopelli, E., Conen, F., Zimmermann, L., Alewell, C., and Morris, C. E.: Freezing nucleation apparatus puts new slant on study of biological ice nucleators in precipitation, *Atmospheric Measurement Techniques*, 7, 129-134, 2014.

Szyrmer, W., and Zawadzki, I.: Biogenic and anthropogenic sources of ice-forming nuclei: A review, *Bulletin of the American Meteorological Society*, 78, 209-228, 1997.

Tobo, Y.: An improved approach for measuring immersion freezing in large droplets over a wide temperature range, *Scientific Reports*, 6, 2016.

Vali, G.: Quantitative Evaluation of Experimental Results on Heterogeneous Freezing Nucleation of Supercooled Liquids, *Journal of the Atmospheric Sciences*, 28, 402-409, 1971.

Vali, G.: Interpretation of freezing nucleation experiments: singular and stochastic; sites and surfaces, *Atmospheric Chemistry and Physics*, 14, 5271-5294, 2014.

NIST Standard Reference Database 20, Version 3.4 (web version): http:/srdata.nist.gov/xps/, 2003.

Wagner, R., Mohler, O., Saathoff, H., Schnaiter, M., and Leisner, T.: New cloud chamber experiments on the heterogeneous ice nucleation ability of oxalic acid in the immersion mode, *Atmospheric Chemistry and Physics*, 11, 2083-2110, 2011.

Wang, B.: Physics and dynamics of clouds and precipitation., Cambridge University Press, Cambridge, 2013.

Wang, B. B., and Knopf, D. A.: Heterogeneous ice nucleation on particles composed of humic-like substances impacted by O-3, *Journal of Geophysical Research-Atmospheres*, 116, 2011.

Watanabe, M., Makino, T., Okada, K., Hara, M., Watabe, S., and Arai, S.: Alkylbenzyldimethylammonium Salts as Inhibitors for the Ice Nucleating Activity of Erwinia-Ananas, *Agricultural and Biological Chemistry*, 52, 201-206, 1988.

Watts, J. F., and Wolstenholme, J.: An Introduction to Surface Analysis by XPS and AES, Wiley, Rexdale, 2003.

Wegener, A.: Thermodynamik der Atmosphäre., J.A. Barth, Leipzig, 1911.

Welti, A., Lueoend, F., Kanji, Z. A., Stetzer, O., and Lohmann, U.: Time dependence of immersion freezing: an experimental study on size selected kaolinite particles, *Atmospheric Chemistry and Physics*, 12, 9893-9907, 2012.

Wex, H., Augustin-Bauditz, S., Boose, Y., Budke, C., Curtius, J., Diehl, K., Dreyer, A., Frank, F., Hartmann, S., Hiranuma, N., Jantsch, E., Kanji, Z. A., Kiselev, A., Koop, T., Mohler, O., Niedermeier, D., Nillius, B., Rosch, M., Rose, D., Schmidt, C., Steinke, I., and Stratmann, F.: Intercomparing different devices for the investigation of ice nucleating particles using Snomax (R) as test substance, *Atmospheric Chemistry and Physics*, 15, 1463-1485, 2015.

Whale, T. F., Murray, B. J., O'Sullivan, D., Wilson, T. W., Umo, N. S., Baustian, K. J., Atkinson, J. D., Workneh, D. A., and Morris, G. J.: A technique for quantifying heterogeneous ice nucleation in microlitre supercooled water droplets, *Atmospheric Measurement Techniques*, 8, 2437-2447, 2015a.

Whale, T. F., Rosillo-Lopez, M., Murray, B. J., and Salzmann, C. G.: Ice Nucleation Properties of Oxidized Carbon Nanomaterials, *Journal of Physical Chemistry Letters*, 6, 3012-3016, 2015b.

Wheeler, M. J., and Bertram, A. K.: Deposition nucleation on mineral dust particles: a case against classical nucleation theory with the assumption of a single contact angle, *Atmospheric Chemistry and Physics*, 12, 1189-1201, 2012.

Williams, D. B., and Carter, C. B.: The Transmission Electron Microscope, Springer, Boston, MA, 1996.

Wright, T. P., and Petters, M. D.: The role of time in heterogeneous freezing nucleation, *Journal of Geophysical Research-Atmospheres*, 118, 3731-3743, 2013.

Wyslouzil, B. E., Carleton, K. L., Sonnenfroh, D. M., Rawlins, W. T., and Arnold, S.: Observation of Hydration of Single, Modified Carbon Aerosols, *Geophysical Research Letters*, 21, 2107-2110, 1994.

Yan, J. Y., and Patey, G. N.: Heterogeneous Ice Nucleation Induced by Electric Fields, *Journal of Physical Chemistry Letters*, 2, 2555-2559, 2011.

Zachariassen, K. E., and Kristiansen, E.: Ice nucleation and antinucleation in nature, *Cryobiology*, 41, 257-279, 2000.

Zaragotas, D., Liolios, N. T., and Anastassopoulos, E.: Supercooling, ice nucleation and crystal growth: a systematic study in plant samples, *Cryobiology*, 72, 239-243, 2016.

Zhang, R., Khalizov, A. F., Pagels, J., Zhang, D., Xue, H., and McMurry, P. H.: Variability in morphology, hygroscopicity, and optical properties of soot aerosols during atmospheric processing, *Proc Natl Acad Sci U S A*, 105, 10291-10296, 10.1073/pnas.0804860105, 2008.

Zhao, Y., Liu, Y. C., Ma, J. Z., Ma, Q. X., and He, H.: Heterogeneous reaction of SO2 with soot: The roles of relative humidity and surface composition of soot in surface sulfate formation, *Atmospheric Environment*, 152, 465-476, 2017.

Zheng, Y., Su, C. L., Lu, J., and Loh, K. P.: Room-Temperature Ice Growth on Graphite Seeded by Nano-Graphene Oxide, *Angewandte Chemie-International Edition*, 52, 8708-8712, 2013.

Zolles, T., Burkart, J., Häusler, T., Pummer, B., Hitzenberger, R., and Grothe, H.: Identification of Ice Nucleation Active Sites on Feldspar Dust Particles, *Journal of Physical Chemistry A*, 119, 2692-2700, 2015.

Zuberi, B., Bertram, A. K., Koop, T., Molina, L. T., and Molina, M. J.: Heterogeneous freezing of aqueous particles induced by crystallized (NH4)(2)SO4, ice, and letovicite, *Journal of Physical Chemistry A*, 105, 6458-6464, 2001.

Zuberi, B., Johnson, K. S., Aleks, G. K., Molina, L. T., and Laskin, A.: Hydrophilic properties of aged soot, *Geophysical Research Letters*, 32, 2005.